Markus Ornik, BSc

Relating spot and flare/superflare occurrence on dwarf stars

MASTER'S THESIS

to achieve the university degree of

Master of Science

Master's degree programme: Physics

submitted to

Graz University of Technology

Supervisor

Assoz. Prof. Mag. Dr.rer.nat. Manuela Stadlober-Temmer
Institute of Physics, University of Graz

Co-Supervisor

Mag. Dr.rer.nat. Martin Leitzinger
Institute of Physics, University of Graz

Graz, June 10, 2025

Markus Ornik, BSc

Relating spot and flare/superflare occurrence on dwarf stars –

Thesis in partial fulfillment of the requirements for the degree of Master of Science – MSc;
Thesis submitted on June 11, 2025, and defended on July 10, 2025.

Institute of Physics, NAWI Graz, University of Graz.

Supervisor: Assoz. Prof. Mag. Dr.rer.nat. Manuela Stadlober-Temmer[1]
Co-Supervisor: Mag. Dr.rer.nat. Martin Leitzinger[1]
[1] Institut für Physik, NAWI Graz, University of Graz, Universitätsplatz 5/II, 8010 Graz, Austria.

Abstract

Context. In recent years detection of flares and superflares on stars gained a lot of attention, but the origin of superflares is still under debate. One possibility is that superflares are scaled up versions of normal flares, for which one would expect to find a correlation with the appearance of spots on the stars surface.

Aims. This study aims to relate flares and superflares on stars to the appearance of spots on the surfaces of stars of various spectral types (M, K, G, and F) using Kepler/K2 and TESS lightcurves.

Methods. Over 300 stars were analysed with a newly developed GUI application and flare detection algorithm, which can detect flares with normalized peaks of as low as 0.3% above their surrounding flux. The lightcurves are then folded by the automatically detected spot modulation period and the dependence of flare counts across the normalized phase are analyzed.

Results. The analysed stars are investigated according to their spectral type. We also present individual results for BD-08 995, TYC 1360-957-1, TYC 4595-107-1, V* V471 Tau, V* HK Aqr, KOI-256 and 2MASS J19230963+3739397. The only cumulative results which shows a significant spot dependence are those for G type stars. The results for K type stars show one significant peak in the 10 bin histogram. There was no significant spot dependence found for M type stars, even though some individual stars show a distinct spot dependence.

Conclusions. Investigations of spot to flare dependence from literature could be partially reproduced. It is furthermore found that the used flare algorithm as well as the sample of stars used for analysis affect the results. The present investigation has revealed that only G-type main-sequence stars show a larger number of flares on a more spotted hemisphere.

Kurzfassung

Kontext. In den letzten Jahren hat die Detektion von Flares und Superflares auf Sternen viel Aufmerksamkeit erhalten, jedoch ist der Ursprung von Superflares immer noch umstritten. Eine Möglichkeit ist, dass Superflares energiereichere normale Flares sind. In diesem Fall wäre eine Korrelation mit dem Auftreten von Flecken auf der Sternoberfläche zu erwarten.

Ziele. Das Ziel dieser Studie ist es Flares und Superflares und das Auftreten von Flecken auf Sternoberflächen verschiedener Spektraltypen (M, K, G, und F) in Relation zu bringen. Dafür wurden Lichtkurven von Kepler/K2 und TESS verwendet.

Methoden. Es wurden über 300 Sterne mit einer neu entwickelten GUI-Anwendung und einem Flareerkennungsalgorithmus analysiert, welcher Flares mit normalisierten Spitzenwerten von 0.3% über dem Umgebungsfluss erkennen kann. Die Lichtkurven werden danach mit einer automatisch erkannten Fleckenmodulationsperiode gefaltet und die Abhängigkeit der Flareanzahl von der normalisierten Phase wurde analysiert.

Ergebnisse. Die analysierten Sterne wurden anhand ihres Spektraltyps untersucht. Wir präsentieren auch einzelne Ergebnisse für die Sterne BD-08 995, TYC 1360-957-1, TYC 4595-107-1, V* V471 Tau, V* HK Aqr, KOI-256 und 2MASS J19230963+3739397. Die einzige signifikante Fleckenabhängigkeit wurde bei den Gesamtergebnissen für G-Sterne gefunden. Die Ergebnisse für K-Sterne zeigen einen signifikanten Spitzenwert im Histogramm mit 10 Bins. Für M-Sterne wurde keine signifikante Abhängigkeit gefunden, obwohl ein paar Einzelsterne eine Abhängigkeit aufweisen.

Fazit. Ähnliche Untersuchungen aus der Literatur konnten teilweise reproduziert werden. Darüber hinaus wurde ermittelt, dass sowohl der Flareerkennungsalgorithmus als auch die Auswahl an analysierten Sternen einen Einfluss auf das Ergebnis haben. Die derzeitige Untersuchung hat gezeigt, dass nur Hauptreihensterne vom Spektraltyp G eine erhöhte Anzahl an Flares auf einer fleckenreicheren Hemisphäre zeigen.

Acknowledgement

I gratefully acknowledge my supervisors Assoz. Prof. Mag. Dr.rer.nat. Manuela Stadlober-Temmer and Mag. Dr.rer.nat. Martin Leitzinger for guiding me through the process.

Additionally I thank Dr. Petra Odert for proof reading the manuscript as well as providing helpful comments.

I thank my family and friends for supporting me.

This thesis made use of the experimental setups, laboratory and technical infrastructure, general resources and observational facilities of the Institute of Physics of the University of Graz. This thesis also made use of infrastructure, which was supported by NAWI Graz.

This research made use of pandas (The pandas development team, 2020; McKinney, 2010). This research made use of Astropy, a community-developed core Python package for Astronomy (Astropy Collaboration et al., 2013; Astropy Collaboration et al., 2018). This research made use of SciPy (Virtanen et al., 2020). This research made use of matplotlib, a Python library for publication quality graphics (Hunter, 2007). This research made use of NumPy (Harris et al., 2020). This research made use of Astroquery (Ginsburg et al., 2019).

This research has made use of the SIMBAD database, operated at CDS, Strasbourg, France.

This paper includes data collected by the Kepler mission and obtained from the MAST data archive at the Space Telescope Science Institute (STScI). Funding for the Kepler mission is provided by the NASA Science Mission Directorate. STScI is operated by the Association of Universities for Research in Astronomy, Inc., under NASA contract NAS 5–26555.

This paper includes data collected with the TESS mission, obtained from the MAST data archive at the Space Telescope Science Institute (STScI). Funding for the

TESS mission is provided by the NASA Explorer Program. STScI is operated by the Association of Universities for Research in Astronomy, Inc., under NASA contract NAS 5–26555.

I gratefully acknowledge the Austrian Science Fund (FWF): I5711-N (PI: Martin Leitzinger) for supporting this project.

Contents

1 Introduction

This chapter gives a brief introduction to the goals of this study, the state of the art, scientific backgrounds such as spectral types, spots and flares, as well as to the space missions from which data has been extensively used for the present study.

The goal of this study is to relate flares/superflares to the appearance of spots on the surfaces of stars of various spectral types. Flares are well studied for the Sun (Aschwanden and Freeland, 2012; Zhang et al., 2012; Shibata and Magara, 2011) with the first recorded event being the Carrington event from September 1859 (Carrington, 1859). The same accounts for the impact of stellar activity on Earths magnetic field (Gopika et al., 2025). A detailed description of spots and flares is given in section 1.3. While the first stellar flares were discovered in middle of the last century (Joy and Humason, 1949; Luyten, 1949), the topic gained a lot of attraction with the launch of the likes of Kepler (Borucki et al., 2010) and the Transiting Exoplanet Survey Satellite (TESS) (Ricker et al., 2014b). They allowed the survey of thousands of stars. With this, studies of flares and superflares on a large number of stars have been conducted (Maehara et al., 2015; Maehara et al., 2018; Roettenbacher and Vida, 2018; Howard and Law, 2021), but the origin of superflares (flares with a bolometric energy above 10^{33} erg) is still not clear. So far no superflare has been observed on our Sun, but there have been studies focusing on the possible origin on superflares and their likelyhood to happen on our Sun (Shibata et al., 2013). They found that superflares on our Sun would be rare events (every $\sim$800 years for superflares with 10^{34} erg). Even more recently Vasilyev et al. (2024) estimated the occurrence rate of superflares with $> 10^{34}$ erg on Sun-like stars to roughly once per century.

A few proposed generation mechanisms for superflares could be star-planet interaction (SPI) (Ilin and Poppenhaeger, 2022; Cuntz et al., 2000; Ip et al., 2004), or just being scaled up version of normal flares which we see from our Sun coming from large spots (Notsu et al., 2013; Maehara, 2017). In the latter case, we would expect to see a correlation between the appearance of superflares and the spot modulation/phase (spots or spot groups rotating in and out of the visible disk of a star, periodically slightly dimming it).

1.1 State of the art - relation between flare occurrence, spots, and rotation

Doyle et al. (2018) studied 34 M dwarfs from the K2 mission, using short cadence observational data. They confirmed that the stars in their dataset with a rotational period of less than 10 days showed more flares than stars with longer rotation periods, which was already shown previously (Mohanty and Basri, 2003; McLean et al., 2012). Furthermore they found no star with a preference for when flares occured during the rotational phase (Doyle et al., 2018). A similar study using TESS 2 minute cadence data has been conducted by Doyle et al. (2019). In this study they used data of 167 M dwarfs and found a total of 1834 flares. Similar to the study on K2 data, they found no preference for rotational phase (Doyle et al., 2019).

Roettenbacher and Vida (2018) investigated a sample of 119 stars from spectral types M to F. They used a subset of the Kepler long-cadence data. They found that flares which increase the stellar flux by 1% to 5% appear more often while larger starspots are visible, while flares which increase the flux by more that 5% do not seem to have this dependency (Roettenbacher and Vida, 2018).

Further analysis on periodic flare occurrence was done by Howard and Law (2021), who studied TESS lightcurves of 284 cool dwarfs. They found three targets (TIC 80427281, TIC 95328477, TIC 220432563) with a confirmed flare periodicity, which correlates to their rotational period or half of it. There have also been studies on individual stars, for example Araújo and Valio (2021) focused on Kepler-411, which is a K2V dwarf, by investigating the relation between superflares and star spots on that star. They found a positive correlation between the energy of flares and the area of star spots (Araújo and Valio, 2021) on Kepler-411. They then compared their results for Kepler-411, which produced multiple superflares, with Kepler-210 (a K dwarf with two planets), which did not produce superflares while having the same number of spots (Araújo and Valio, 2023). They found the spots on Kepler-210 to be larger, warmer and therefore being magnetically weaker/less complex compared to Kepler-411 and concluded that the area of starspots is not the only relevant parameter for superflare occurrence (Araújo and Valio, 2023).

Star-planet interaction was studied by Ilin and Poppenhaeger (2022) for the star AU Mic. While they found a signal in their used TESS lightcurves correlating with the orbital period of AU Mic b, they state that a $> 3\sigma$ detection requires more observations (Ilin and Poppenhaeger, 2022).

In conclusion, many flares and superflares have been found on stars, but the origin of the latter is still not clear. Although it is widely accepted that superflares may be scaled up normal flares, still the issue of star-planet interaction is discussed. Furthermore, the above mentioned studies could not relate flare/superflare occurrence distinctively to the spottedness of stars. With a large data set comprised of Kepler, K2 and TESS data we aim for a more distinct relation of flare/superflare occurrence and spottedness of stars.

1.2 Spectral Types

Spectral classification is a way to classify the vast amount of stars into various types. The original definition of the currently used Harvard System was developed by Cannon and Pickering (1912a). It characterized stars by their most prominent spectral lines. The different spectral types introduced are O, B, A, F, G, K and M. In this system the stars were differentiated by their different prominent spectral lines. For example B type stars were described to have faint hydrogen lines, but numerous helium lines. Another example would be spectral class A, which was described to have the most prominent hydrogen lines (Cannon and Pickering, 1912a). Furthermore the spectral classes were divided into 10 subtypes, with 1 to 9 attached to the letter. In a later revision, the spectral types without a numeral had a 0 attached, for example B to B0 or A to A0 (Cannon and Pickering, 1912b). If the exact spectral type can not be determined, the numeral should be left out (Cannon and Pickering, 1912b). Payne-Gaposchkin (1925) then found that this specification links to the effective temperature of stars, with O being the hottest, and M being the coolest. The same applies to the subtypes, with 0 being the hottest, and 9 the coolest of their respective type (Berlind, 2025). Additionally the terms "early" and "late" are often used and can refer to the spectral type itself, with the hotter O, B, or A stars being "early" type, and cooler F, G, K, M stars being "late" types, or if used in combination with a spectral type, it refers to hotter or colder subtypes like K0 being an early K type or G9 being a late G type (Allen, 2025). Table 1.1 shows the spectral types with their respective approximate temperature range as well as color.

Table 1.1.: Table showing the different spectral types, in relation to their minimum and maximum effective temperature ranges in Kelvin. Based on the tables given in (Allen, 2025; Berlind, 2025).

Spectral type	min. T_{eff} [K]	max. T_{eff} [K]	Color
O	25000	-	Blue
B	10000	25000	Blue
A	7500	10000	Blue
F	6000	7500	Blue to White
G	5000	6000	White to Yellow
K	3500	5000	Orange to Red
M	-	3500	Red

1.3 Spots and Flares

This section gives a short overview of starspots/flares by explaining it based on the best observable example we have: the Sun.

1.3.1 Spots

Sunspots, or genereally speaking spots, are magnetic regions on the surface of a star that are cooler than their surroundings. Spots generally have an umbra, which is the center, and the penumbra, which is surrounding the umbra and separating it from the rest of the surface of the star (Solanki, 2003). If a spot does not have a penumbra, it is called a pore (Solanki, 2003). The size of spots varies greatly, and can be up to a diameter of 60000 km on the Sun and have lifetimes from a few days up to several months (Solanki, 2003). The umbra can be 1000 to 1900K cooler than the solar surface, while the penumbra can be 250 to 400 K cooler, which also causes them to be less bright than the rest of the photosphere (values for the Sun, Solanki (2003)). This is because the strong magnetic fields (1800 to 3700 G in the umbra and 700 to 1000 G in the penumbra, compared to a few gauss in the photosphere (Solanki, 2003)) limit the convection process, effectively reducing the thermal energy in this area (Solanki, 2003; Fox, 2025). An example of a sunspot can be seen in figure 1.1. The image was taken by SOHO (Solar & Heliospheric Observatory)[1,2,3]. It shows a sunspot, with its umbra (black area) being slightly larger than Earth. The penumbra is visible in orange, and the surrounding solar photosphere is colored in yellow. Additionally an image of the full solar disk at the same time the spot image was taken is included in the top right. The sunspot is located slightly left of the center. Figure 1.2 shows a sketch of a sunspot, with its

[1] https://soho.nascom.nasa.gov/
[2] https://www.esa.int/Science_Exploration/Space_Science/SOHO
[3] https://science.nasa.gov/mission/soho/

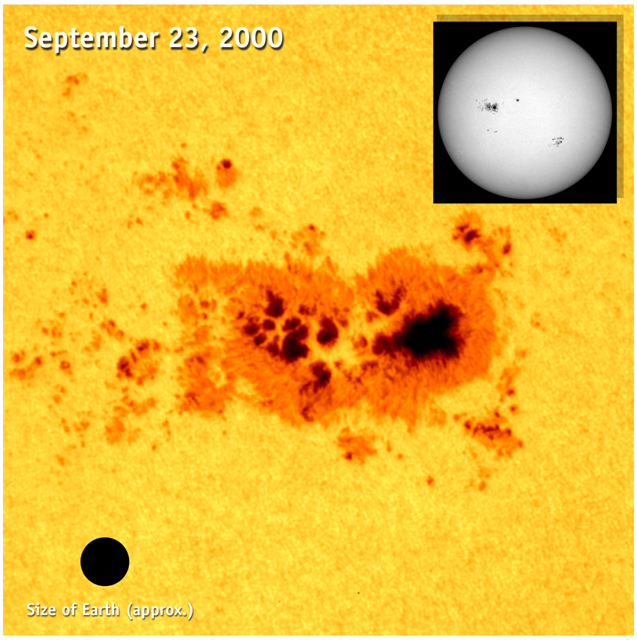

Fig. 1.1.: Image showing a sunspot from 23 September 2000. Comparison of its size to Earth in the bottom left. The whole disk of the Sun is visible in the top right corner. Image taken from the SOHO image gallery (The SOHO Team, 2025).

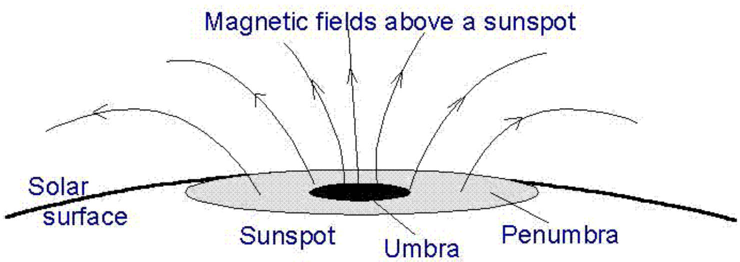

Fig. 1.2.: Image showing magnetic field lines coming out of a sunspot. Field lines are denser in the umbra compared to the penumbra, representing stronger magnetic fields. Image from Australian Space Weather Forecasting Centre (2025).

umbra and penumbra and magnetic field lines, with more field lines at the umbra representing a stronger magnetic field. Each spot is also magnetically linked to one or more spots of the opposite polarity, with the magnetic field varying in complexity. A simple example of this can be seen in figure 1.3.

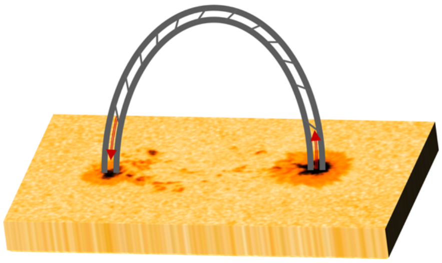

Fig. 1.3.: Image showing two sunspots being connected by magnetic field lines. Image from Norton (2025).

1.3.2 Flares

Flares are a sudden release of a huge amount of magnetic energy, which happens due to magnetic reconnection (Shibata and Magara, 2011) with the first flare observed on 1 September 1859 by Carrington (1859) and Hodgson (1859). Hayakawa et al. (2023) estimated the energy release of the flare to $5.77 \pm 2.89 * 10^{32}$ erg, with an estimated GOES classification of X46 to X126 with a median of X80. The energy which is released, is the so called free magnetic energy (Priest and Forbes, 2000; Priest and Forbes, 2002). This is the excess energy above the ground state of the magnetic field. During a period of days to weeks this free energy is accumulated by braiding, sheering and twisting the frozen-in magnetic fields (Priest and Forbes, 2000; Priest and Forbes, 2002). The more the magnetic field now differs from the unmodified state, the more energy is built up which is then released in a magnetic reconnection (Priest and Forbes, 2000; Priest and Forbes, 2002). For this two magnetic field lines of opposing direction need to come close (Priest and Forbes, 2000; Priest and Forbes, 2002). This causes a current sheet to form due to the strong current flow (Priest and Forbes, 2000; Priest and Forbes, 2002). In this region the frozen-in state is broken (Priest and Forbes, 2000; Priest and Forbes, 2002). The energy that is released during the reconnection process causes a temperature increase of the surrounding plasma (multiple 10 million K) (Priest and Forbes, 2000; Priest and Forbes, 2002). This is then observed in soft X-ray, EUV, FUV, UV as well as some lines in the visible spectrum and in radio (Priest and Forbes, 2000; Priest and Forbes, 2002). Additionally particles are accelerated and when they hit the denser chromosphere, those particles are decelerated quickly, producing hard X-ray (Bremsstrahlung) (Priest and Forbes, 2000; Priest and Forbes, 2002). The energy release can take just a few tens of seconds, but can also last up to a few hours on the Sun (Reep and Barnes, 2021). An illustration of this process can be seen in figure 1.4.

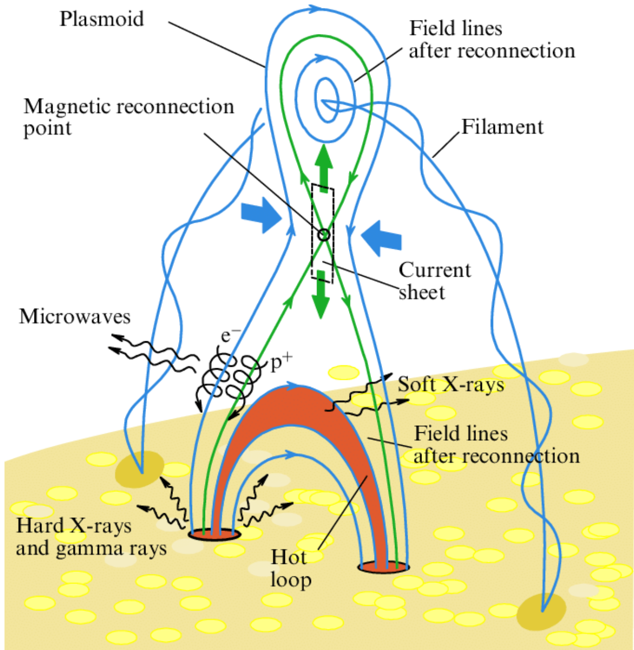

Fig. 1.4.: Illustration showing the standard model for a solar flare. The blue arrows indicate inflow of cool plasma. The green arrows indicate outflow of hot plasma. Image from Lysenko et al. (2019).

1.4 Space missions

This section gives a short overview on the space mission from which the data was used for this study.

1.4.1 Kepler and K2

The Kepler space telesope was named after Johannes Kepler and was launched in 2009[4] and its primary mission lasted till May 2013[5]. Its main scientific goal was the discovery of exoplanets, especially Earth-sized ones, in the habitable zone around their host star using the transit method[6] (Borucki et al., 2010).

It provides two different types of data: short cadence (1 minute exposure) and long cadence (30 minute exposure) data[5] (Borucki et al., 2010). While short cadence data provides a higher temporal resolution, it was used for fewer targets (Borucki et al., 2010). It had a fixed exposure time of 6.02 seconds for its photometer with a field of view of 115 deg^2 near the Cygnus constellation[5] (Borucki et al., 2010) and is most sensitive in the visual to near infrared as seen in figure 1.5. The data was then accumulated for selected targets to either short or long cadence, and then

4 https://science.nasa.gov/mission/kepler/in-depth/
5 https://archive.stsci.edu/missions-and-data/kepler
6 https://exoplanetarchive.ipac.caltech.edu/docs/KeplerMission.html

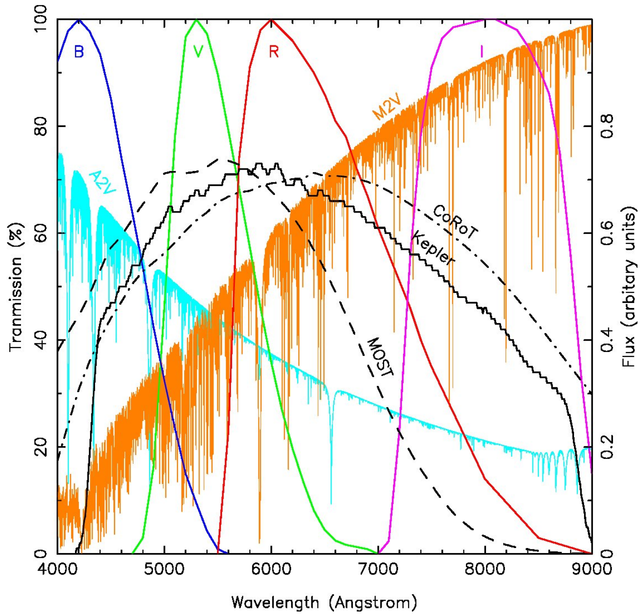

Fig. 1.5.: Johnson B, V, R and I in comparison to the Kepler, MOST and CoRoT missions response curves. Also shown is a A2V and a M2V spectrum. Image from Rowe et al. (2009).

downloaded (Borucki et al., 2010). The space telescope could accomodate data of around 170,000 targets with long cadence and 512 targets with short cadence (Borucki et al., 2010). The spatial resolution of each of the 42 CCDs was 4 arcseconds per pixel (Doyle et al., 2019; Gilliland et al., 2011).

The K2 mission is the continuation mission of Kepler after the second of four of its reaction wheels broke in 2013[4] (Mikulski Archive for Space Telescopes, 2025). Due to this, a follow-up mission was proposed, keeping the now limited capabilities in mind[4]. The mission was active from February 2014 till September 2018 when its fuel ran out[7,8,9]. It discovered a total of over 2600 confirmed planets as of 2018[8,9].

1.4.2 TESS

The Transiting Exoplanet Survey Satellite (TESS) was launched in 2018, with its primary mission lasting two years[10], and was designed to detected exoplanets using the transit method. Since 2020 TESS is in its extended mission, the first being from 2020 to 2022[11], the second from 2022 to 2024[12]. TESS has four identical cameras,

7 https://archive.stsci.edu/missions-and-data/k2
8 https://web.archive.org/web/20181030211627/https://www.nytimes.com/2018/10/30/science/nasa-kepler-exoplanet.html
9 https://www.jpl.nasa.gov/news/nasa-retires-kepler-space-telescope/
10 https://exoplanets.nasa.gov/tess/
11 https://archive.stsci.edu/contents/newsletters/august-2020/tess-extended-mission

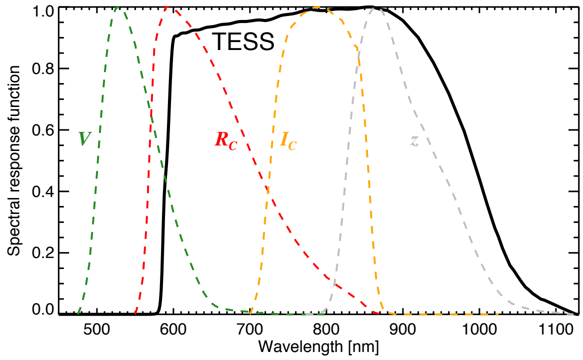

Fig. 1.6.: Johnson V, R_C, I_C and SDSS z (colored dashed lines) response curves and in comparison to TESS (solid black line). Image from Ricker et al. (2014a).

with each providing a 24 times 24 degree field of view[12] (Ricker et al., 2014a). TESS's CCDs have a pixel scale of 21 arcseconds (Ricker et al., 2014a; Doyle et al., 2019) and is most sensitive in the red and near infrared (see figure 1.6). The data is provided in 2 minute cadence for individual stars and 30 minute cadence for full frame images[12]. Since the first extended mission, the cadence for full frame images has been reduced to 200 seconds, and additionally 20 second cadence data is available[12]. TESS observes its targets in so called sectors. Each sector is observed for 27 days[12].

[12]https://tess.mit.edu/science/

GUI application

2

In this chapter the usage of the newly developed GUI application is explained. It was developed to easily download new data, as well as to try various algorithms for flare detection and the usage of various functions of the *lightkurve* python package (Lightkurve Collaboration et al., 2018). The GUI is written in python 3 (Van Rossum and Drake, 2009) and uses the PyQt5 (Riverbank Computing Limited, 2025) framework.

2.1 Data download

During the first startup the GUI window (e.g. in figure 2.2) is nearly completely empty. An empty local database will be created with SQLite3 (SQLite Development Team, 2025). To show lightcurves, data need to be downloaded first. For that, the "Add" button has to be clicked and a new dialog window appears. This can be seen in figure 2.1. This GUI uses the astroquery (Ginsburg et al., 2019) python package to fetch metadata and download flexible image transport system (fits) files from the Mikulski Archive for Space Telescopes (MAST).

The first step is to enter the identifier of the star(s). In case of multiple identifiers, they have to be seperated by a semicolon. Then the missions from which the data should be fetched can be selected. The supported missions are TESS and Kepler/K2. For Kepler and K2 short and/or long cadence can be selected. The differences are described in section 1.4. After the selection has been made, the fetch button needs to be pressed. The program will then request metadata matching the star identifier(s) and selected missions from the MAST archive. The found mission data is then displayed in the preview field. It can then be downloaded by pressing the "Ok" button. The program then proceeds to download the corresponding "fits" files. The filename and TESS sector or Kepler/K2 target table ID is appended to the previously fetched metadata and handed back to the main GUI.

There a request to SIMBAD is made to fetch additional metadata. First the alternative identifiers are fetched from SIMBAD, which also have a MAIN_ID attribute. This is to make sure we only have one entry in the local database per star and no duplicates. Afterwards additional data is fetched from SIMBAD (Wenger et al., 2000) like spectral type, radial velocity and distance. After the data is gathered, the main identifier, the alternative identifiers, spectral type, rotational velocity and distance (and their respective units) as well as the file path, source (TESS, Kepler or K2), and sector/target table ID are saved as an unique identifier into a local database using SQLite3 (SQLite Development Team, 2025). For Kepler/K2 the target table ID was chosen instead of the quarter, as the target table ID is a unique number, whereas there can be multiple "fits" files for the same star and the same quarter.

2.2 Data display and manipulation

Afterwards the list of stars seen in figure 2.2 will be refreshed. It shows the alphabetically sorted main identifier determined from SIMBAD.

When one of the stars in the list is selected, the program will show the additionally saved information. This includes all known identifiers for the star (categorized as alternative identifiers in the Alt. IDs list seen in the "Star infos" section of the GUI), the spectral type, its rotational velocity and its distance (from SIMBAD). Additionally a preferred fitting type for the folded lightcurves (which are described in section 3.2) can be selected. The default value for this is "sine". The list to the right of the information section shows the available "fits" files. The formating for the list entries is "TESS - <sequence>" and "Kepler/K2 - <target table id>". The "combine" button combines temporary multiple "fits" files into one, which is then plotted. Selecting one or combining multiple "fits" files, enables the plot options.

The main plot options allow the user to change the type of flux that is plotted. This is either "SAP_FLUX" (simple aperture photometry) or "PDCSAP_FLUX" (presearch data conditioning simple aperture photometry) (Lightkurve Collaboration et al., 2018) with the latter being the default option. The PDCSAP_FLUX has parts of its data removed depending on the quality flags (e.g. indicating systematic errors like an attitude tweak or a cosmic ray (Twicken et al., 2020; Thompson et al., 2016)) as well as corrected long-term brightness changes (Lightkurve Collaboration et al., 2018). An example of a PDCSAP_FLUX is shown in figure 2.2.

The lightkurve python package also supports normalizing (to unscaled, percent, parts per thousands (ppt) or parts per million (ppm)) which can be seen in figure 2.4. Flattened lightcurves (see figure 2.5 as an example for $BD-08\ 995$) are used to identify flares. The "remove outliers", "remove nans/infs" and "bin" features are available in the GUI, but are not actively used in this thesis.

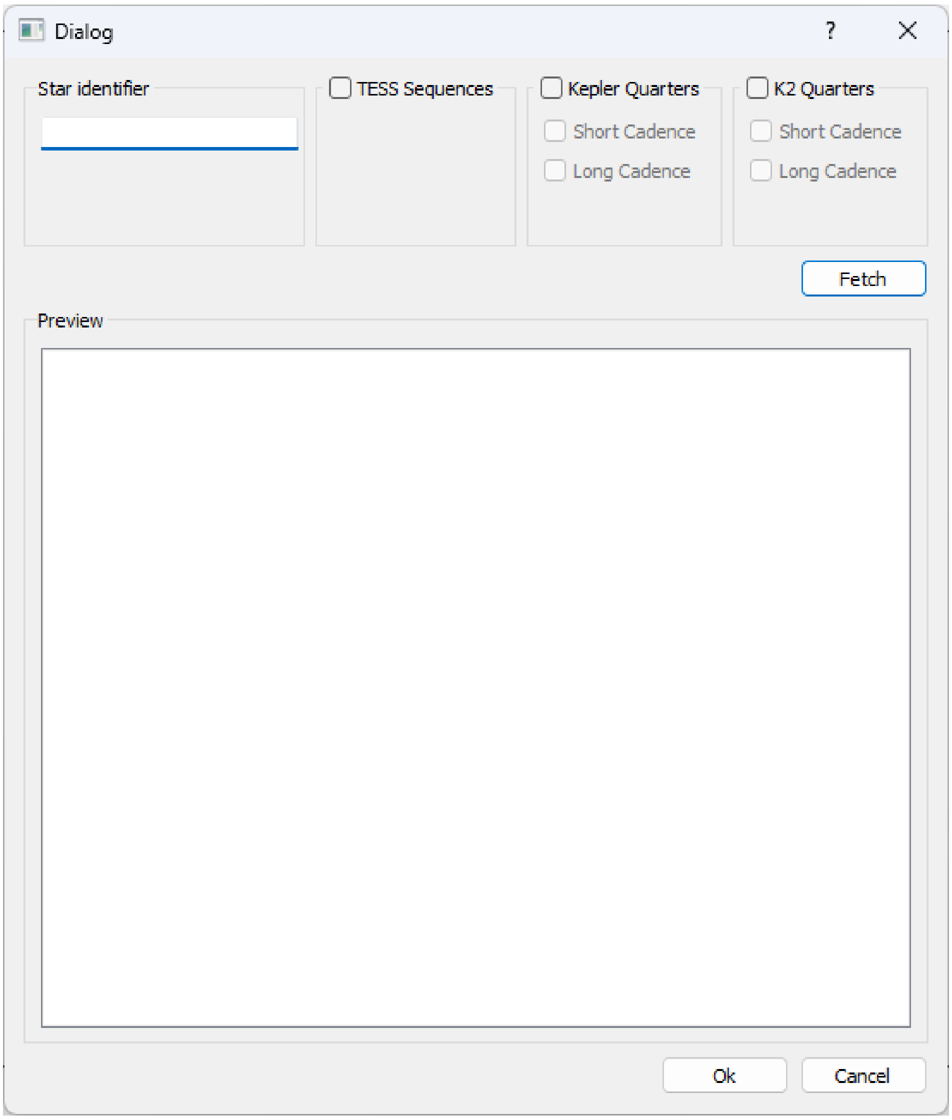

Fig. 2.1.: GUI window for downloading new "fits" files with astroquery designed using the Qt5 designer shipped with PyQt5 (Riverbank Computing Limited, 2025). The star identifier field supports one or more (separated by a semicolon) identifiers. There are checkboxes to select TESS, Kepler (long and/or short cadence) and K2 (long and/or short cadence) data. The preview field shows metadata (Identifier, TESS sector or Kepler/K2 target table ID) to check the data which was found and which can be downloaded. The "Ok" button then proceeds to download the data and hands information back to the main GUI.

The checkboxes to flatten the lightcurve, meaning removing all longterm trends like spot/rotational modulation but leaving short term events intact (figure 2.5), folding the lightcurve (figure 2.6) and showing the periodogram (figures 2.7 and 2.8) are exclusive of each other. Only one can be used at a time. The values for "Period" and "Epoch Time" are automatically calculated and used as default for the selected lightcurve. If "Optimize" in the "Fold" options is unchecked, the "Epoch Time" represents the first found minimum in the lightcurve, and the "Period" is set to the period of the highest peak found in the Lomb-Scargle periodogram. If "Optimize" is checked, it will use the found rotational period of the optimize fold algorithm described in 3.2.2. If "Show Spot Modulation" is selected, it will use the found spot modulation period instead of the rotational period (see section 3.2.2).

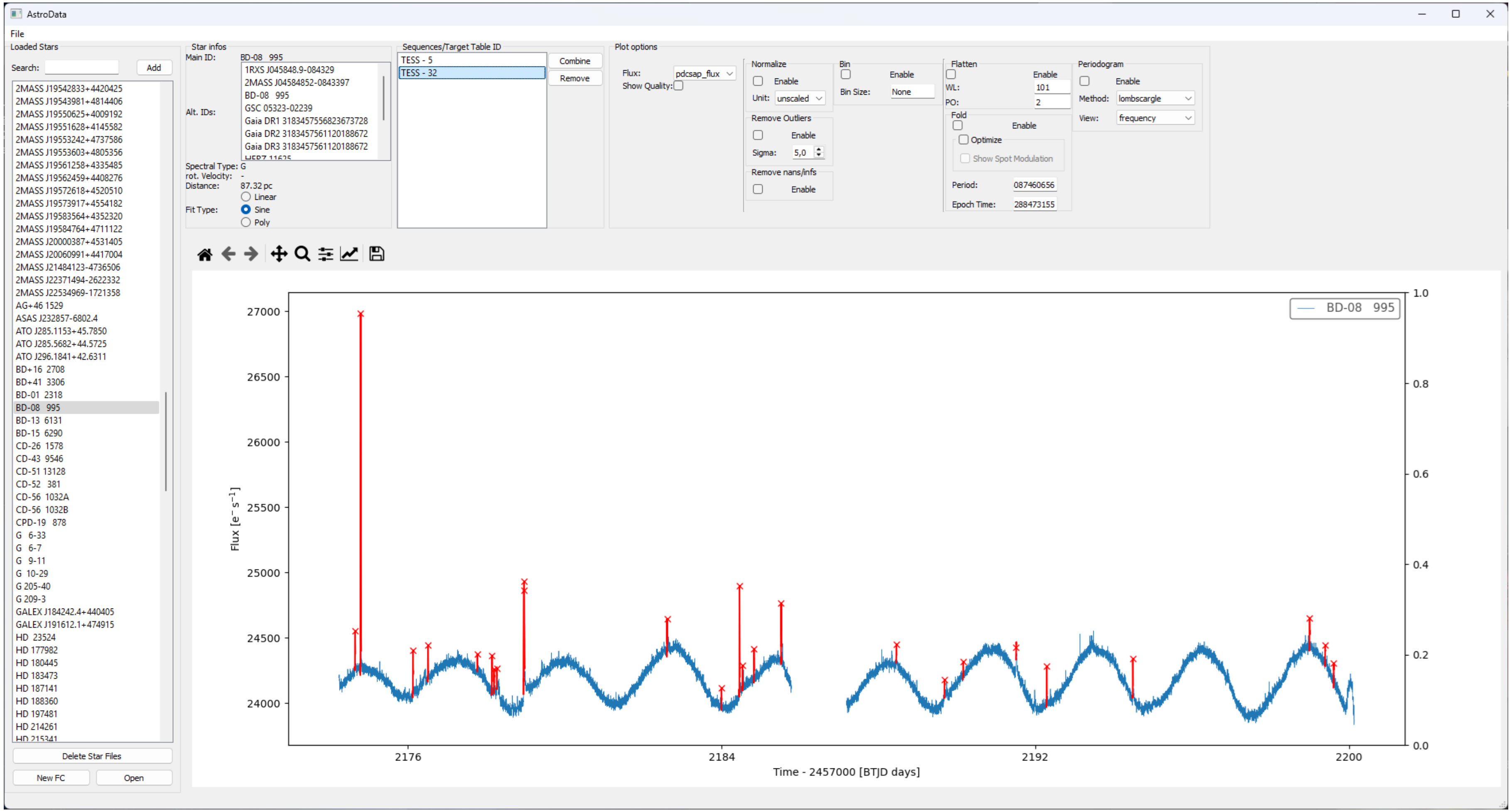

Fig. 2.2.: Main GUI window. This window was designed with the Qt5 designer shipped with PyQt5 (Riverbank Computing Limited, 2025). It shows a list of all available stars with their main identifier (taken from SIMBAD) sorted alphabetically. The "Star infos" box contains additional information on the star gathered from SIMBAD. The "Sequences/Target Table ID" box shows the list of all available lightcurves for the selected star, with an option to combine multiple "fits" files to plot at once. To the right of the list of available lightcurves are different plot options, which utilize the different capabilities of the lightkurve python package (Lightkurve Collaboration et al., 2018). In this image the TESS Sector 32 lightcurve of $BD - 08\ 995$ is shown. The red crosses show the peaks of the detected flares, while the red solid lines the lightcurve indicate the duration estimate of the flare.

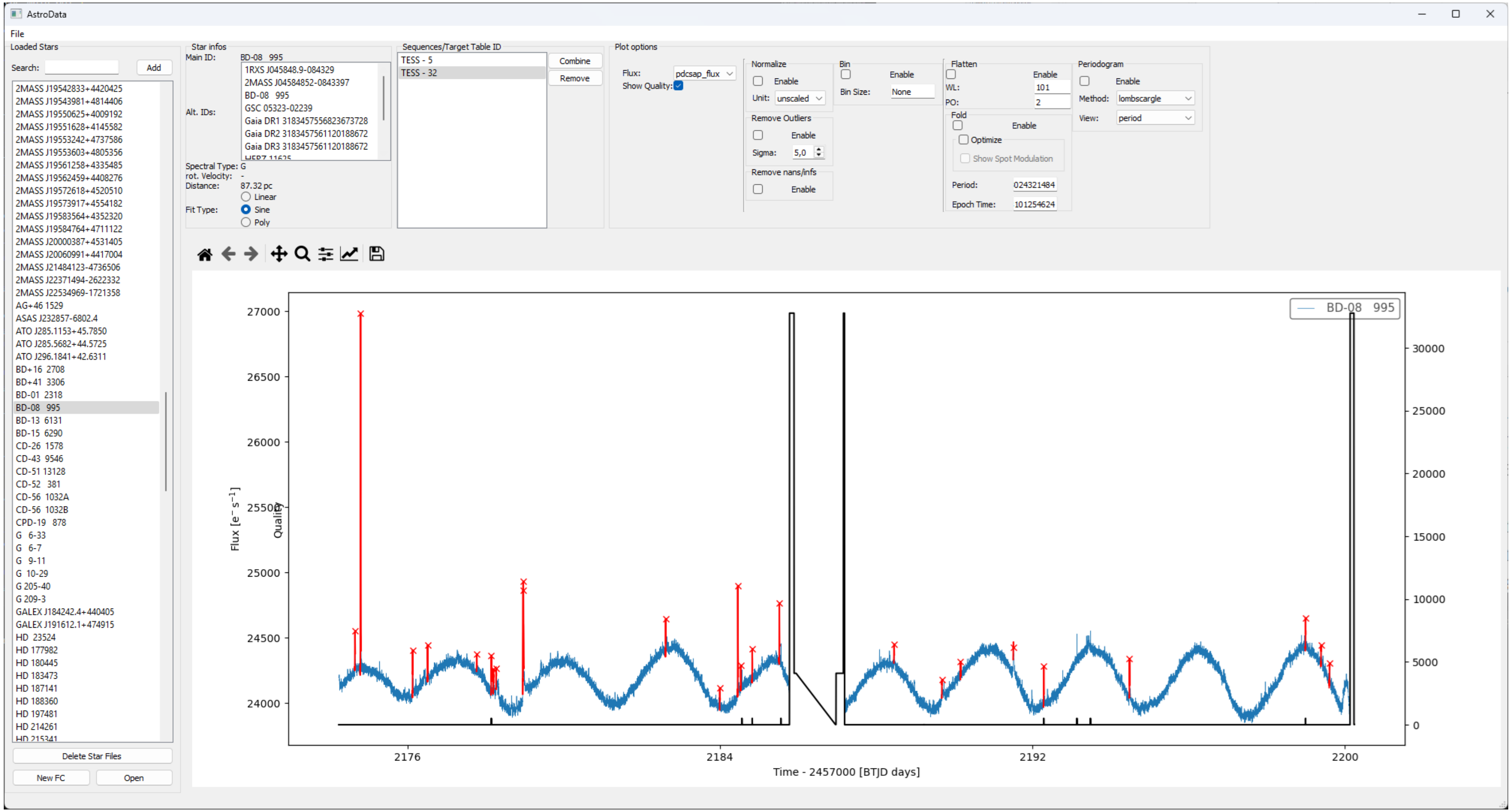

Fig. 2.3.: Main GUI window. Same as in figure 2.2, with the difference that the data quality flag (black solid line) is also shown.

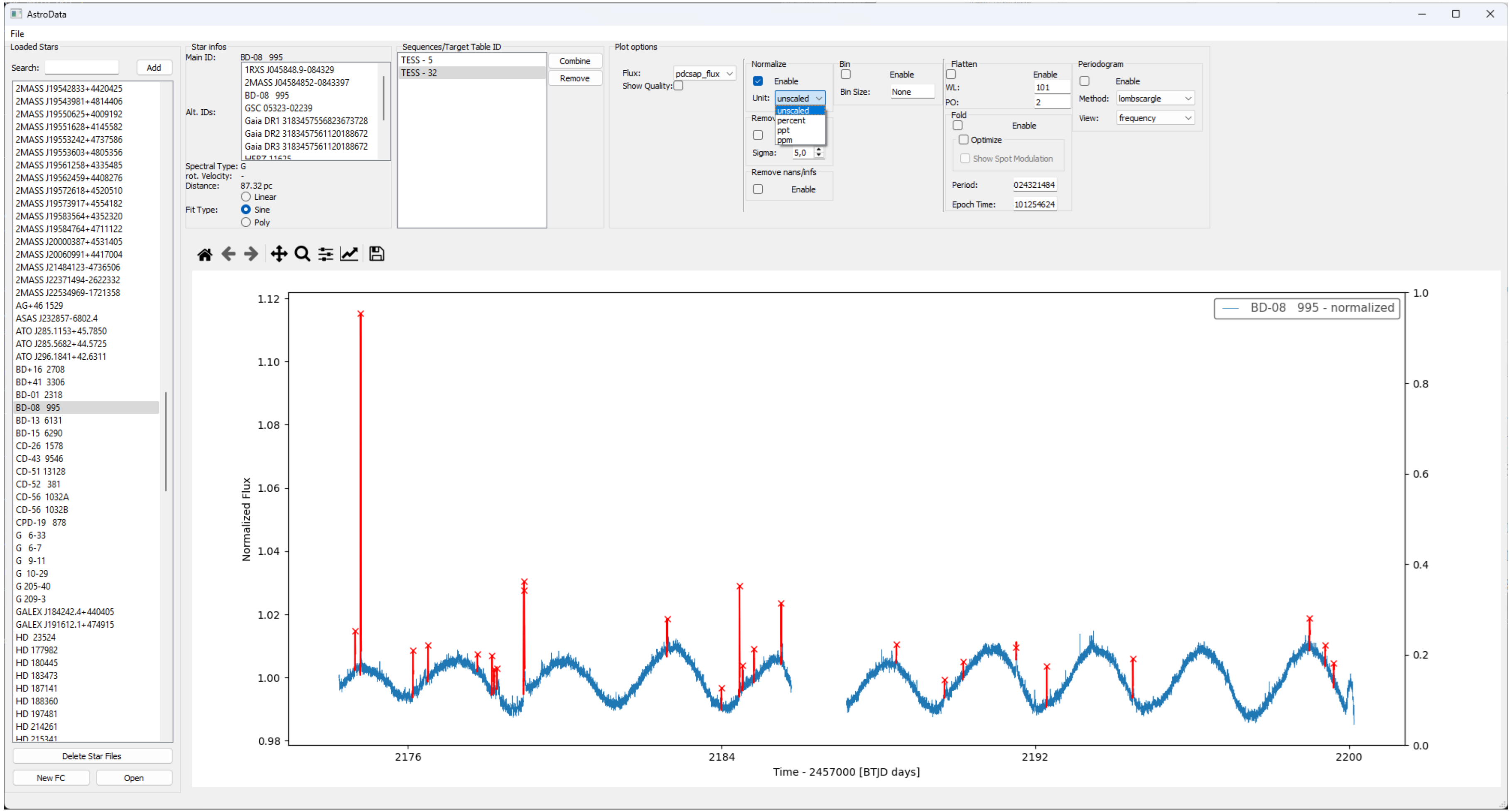

Fig. 2.4.: Main GUI window. Same as in figure 2.2, with the difference that the lightcurve was normalized. It also shows all possible normalize options the lightkurve python package (Lightkurve Collaboration et al., 2018) supports.

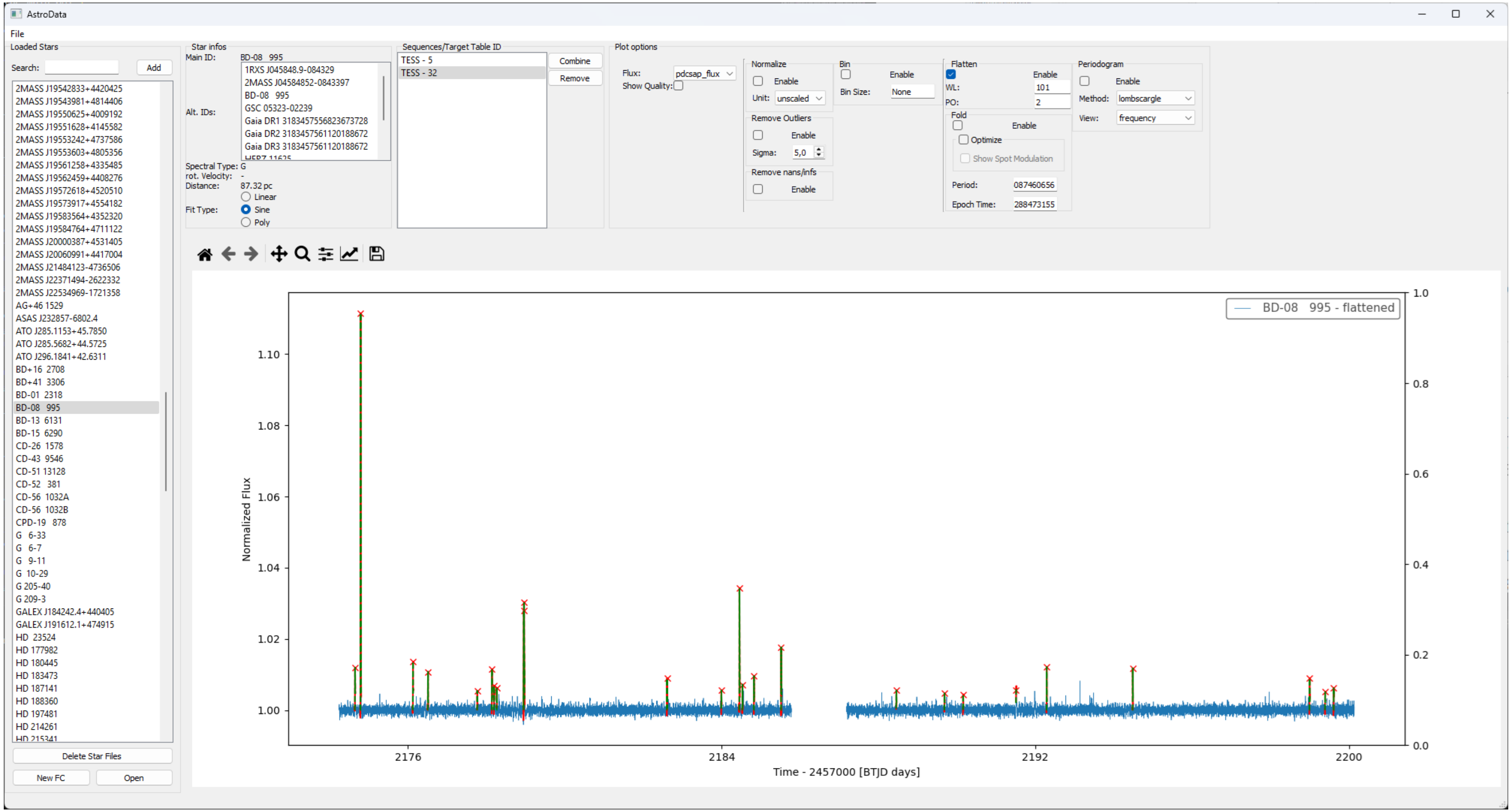

Fig. 2.5.: Main GUI window. Showing the same lightcurve as figure 2.2, with the difference that it is now flattened. The green lines show a fit of the flares. This is described in chapter 3.2.

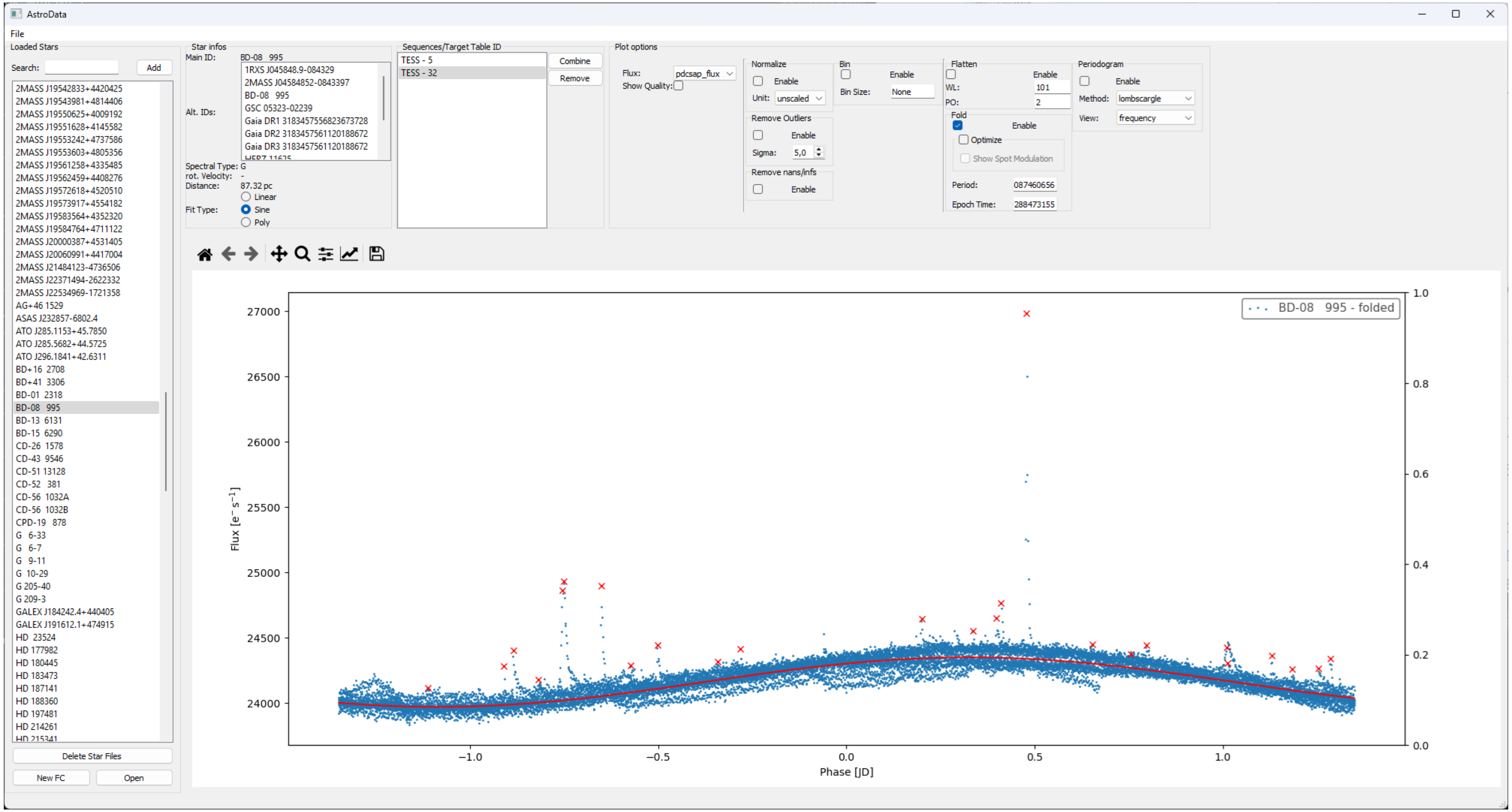

Fig. 2.6.: Main GUI window. Showing the same lightcurve as figure 2.2, with the difference that it is now folded with a period of 2.697 days.

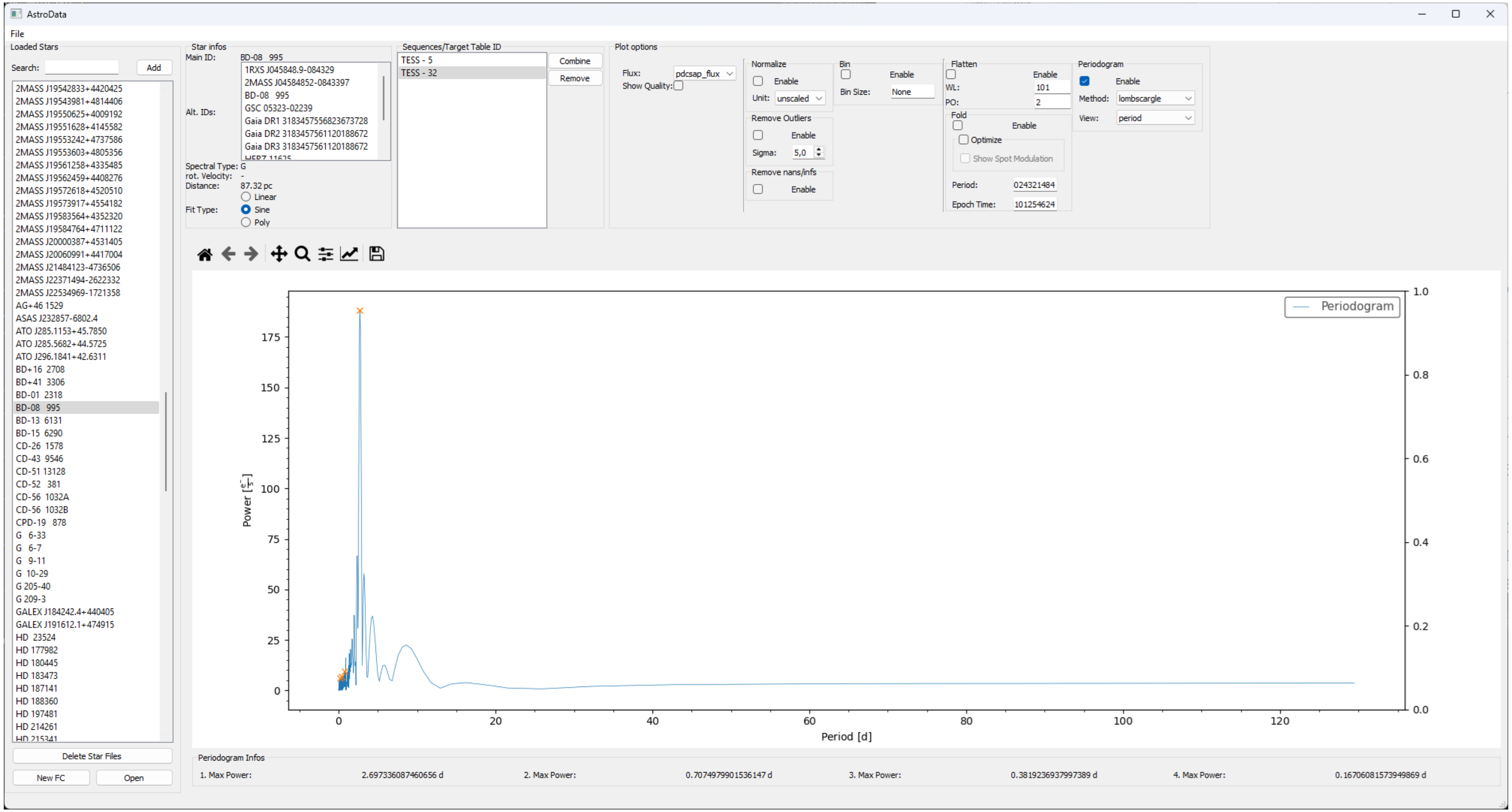

Fig. 2.7.: Main GUI window. Showing the periodogram of the lightcurve in figure 2.2 using the Lomb-Scargle algorithm. Furthermore it shows the four highest peaks (which are at least separated by 100 datapoints). The method is explained in chapter 3.2.

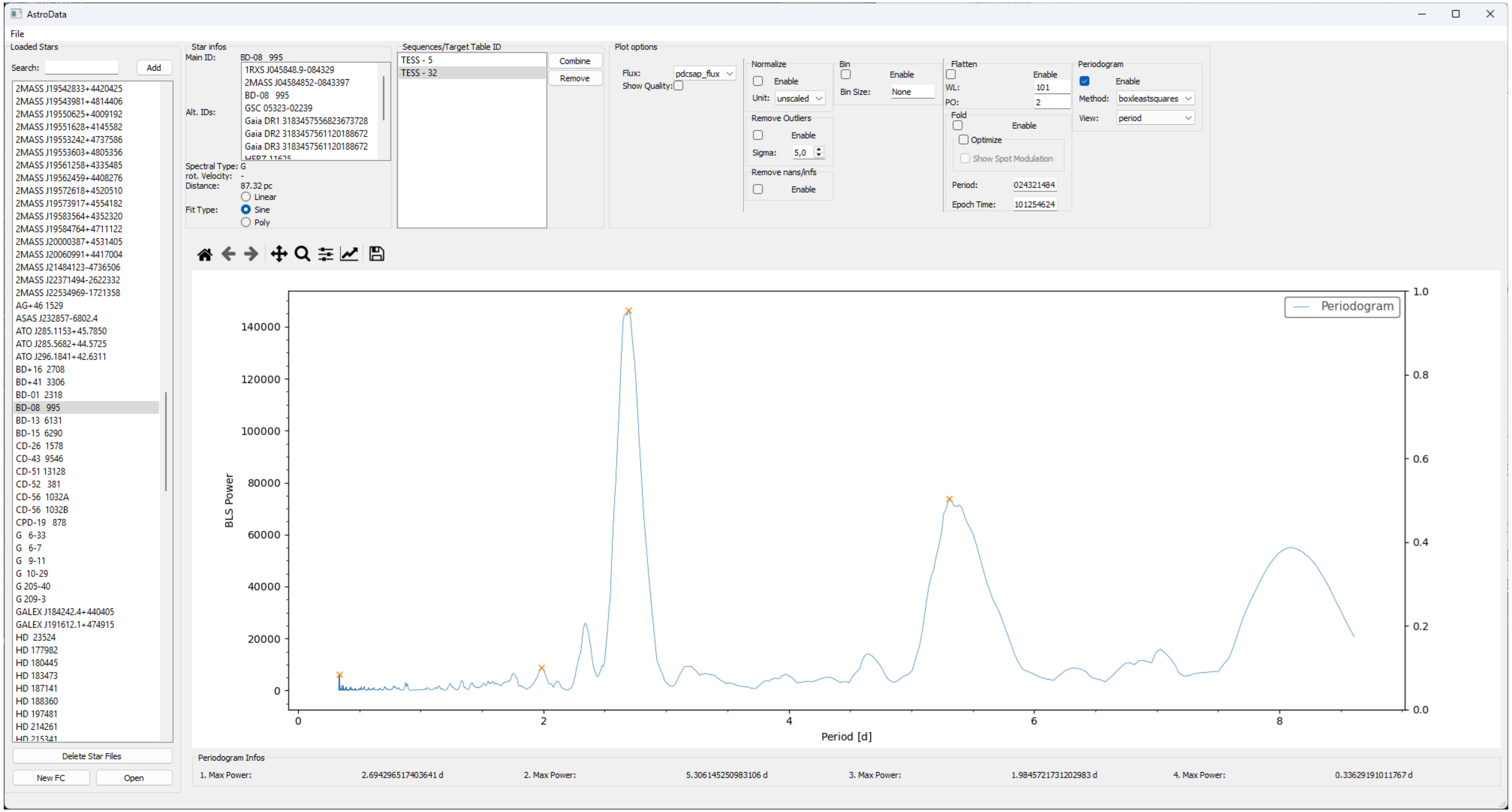

Fig. 2.8.: Main GUI window. Showing the periodogram of the lightcurve in figure 2.2 using the box least square algorithm. Similarly to figure 2.7 the four highest peaks are marked with a red "x".

2.3 Data processing

Pressing the button "New FC" will start the processing of all "fits" files in the current loaded database. It will sequentially go through all files and apply the flare detection algorithms described in section 3.2 to the lightcurves, as well as generate the periodogram and optimized folded lightcurves. This is done for the PDCSAP_FLUX. Additionally plots for each individual lightcurve and processing step are generated. The data provides:

- Flares (peak, timestamp, datapoint index in the lightcurve, TESS/Kepler data quality flags)
- Number of flares
- Fits for the flares (fit, timestamps, indices in the lightcurve, TESS/Kepler data quality flags)
- Uninterrupted timespans in the data
- Total length of timespans in seconds
- Rotational period
- Spot modulation period
- Folded lightcurve phase range
- Folded lightcurve flare positions (phase, peak)
- Period which was used to fold the lightcurve
- Additional boundaries around minima and maxima

And in the case the period and spot modulation of the star differs, it will seperately save the folded lightcurves and related data for the stars period as well.

After this process is finished, a new window will open. It allows to show multiple different debugging statistics like flares per file, flares per star (total, or normalized to a 7 day period) or mean periods for each star. This window can be seen in figure 2.9. The data can then be saved by clicking "File" and then "Save As", which uses the pandas (The pandas development team, 2020) "to_pickle" function. Similarly it can

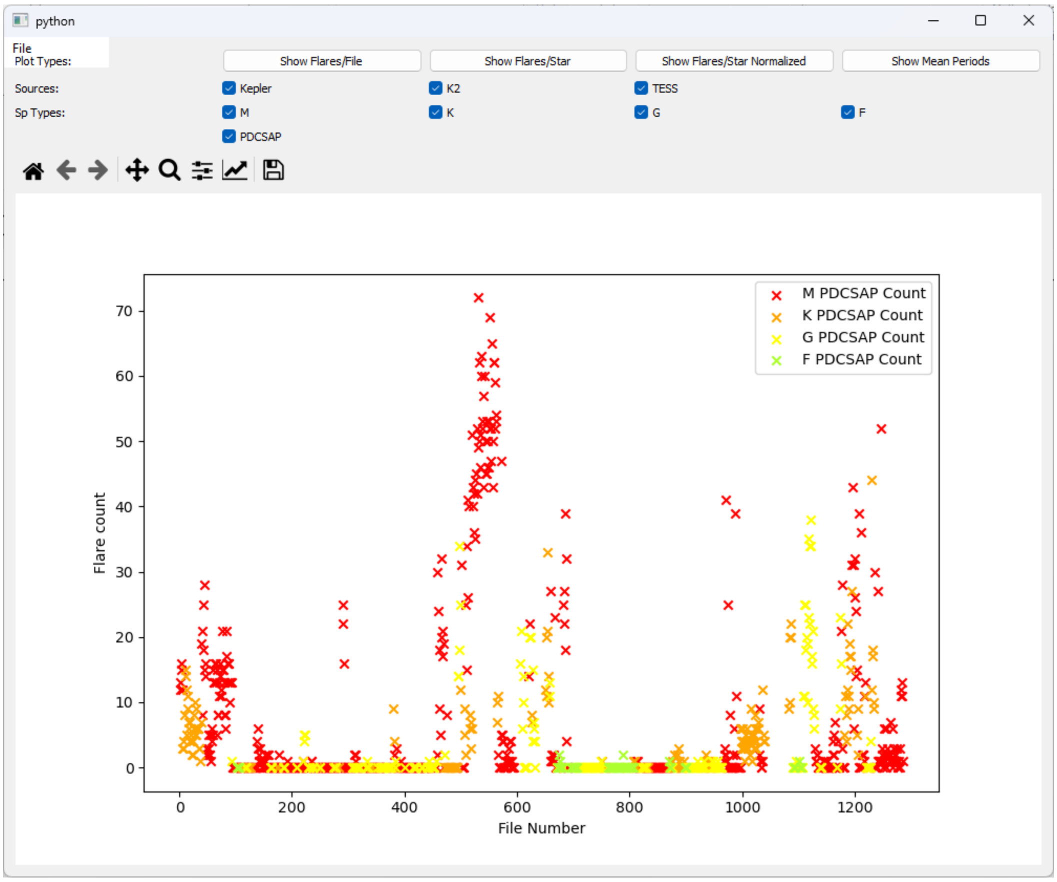

Fig. 2.9.: Debugging statistics window. It has the option to filter data by sources and spectral type for Kepler/K2/TESS pdcsap flux data. It has the ability to show various statistics like flares per "fits" file, flares per star (total or normalized to a period of 7 days), or the mean period detected. The figure shows statistics generated by pressing the "Show Flares/File" button.

be loaded again using the "read_pickle" function which is called either by "File" and then "Open" in the debugging statistics window, or by clicking "Open" in the main window next to "New FC".

3 Data and Methods

In this chapter the selection criteria for the data are explained (section 3.1). Furthermore a detailed description of the algorithm is given in section 3.2.

3.1 Data selection

This study uses a broad selection of Kepler/K2 and TESS lightcurves (427 for Kepler, 27 for K2, 1579 for TESS), which were downloaded from MAST with the help of the astroquery (Ginsburg et al., 2019) python package. For Kepler and its continuation mission K2 short-cadence data were used. Unlike long-cadence data with a cadence of 30 minutes, this allows the resolution of shorter events too, as the duration of flares can vary between a few tens of seconds to a few hours (Reep and Knizhnik, 2019). The initial dataset was taken from a list of well known flaring stars from Araújo and Valio (2021), Araújo and Valio (2023), Doyle et al. (2018), Doyle et al. (2019), Ilin and Poppenhaeger (2022) and Howard and Law (2021). These stars were selected because previous studies revealed that these stars showed detectable flares. This allowed a test of the algorithm described in the next section and a comparison with previous results. Additionally the dataset of M to F stars of Althukair and Tsiklauri (2023) which can be found at https://github.com/akthukair/AFD was parsed to the downloader GUI. As not all data were available as short cadence data from Kepler/K2, only a subset of this large sample was added. The full list of stars, for which datasets were downloaded and parsed can be found in appendix A table A.1.

3.2 Data reduction algorithms

This chapter explains the methods used in this study, split into the algorithms for flare detection and folding lightcurves. Everything, like the GUI discussed in chapter 2, was written in python 3 (Van Rossum and Drake, 2009). It also makes extensive use of the python packages astropy (Astropy Collaboration et al., 2018), numpy (Harris et al., 2020), scipy (Virtanen et al., 2020), pandas (The pandas development team, 2020) and lightkurve (Lightkurve Collaboration et al., 2018). The focus of this chapter lays in the description of the method used to create the final output, which is less customizable than the GUI, which exposes most parameters offered in the functions of the lightkurve API. Unless stated otherwise, the default parameters are used. Furthermore for the final output only PDCSAP_FLUX is used, which is set as the default flux in the lightkurve $LightCurve$ objects after reading the fit file. The methods are the same for both $KeplerLightCurve$ and $TessLightCurve$ subclasses.

3.2.1 Flare detection

The first step is to normalize the lightcurve. This is done to apply the same thresholds to all files in later steps. An example of this is shown in figure 2.4 in chapter 2.2. The normalization is done via the $normalize()$ function of the $LightCurve$ class of the lightkurve api. Afterwards the lightcurves are flattened by the function $flatten()$ of the $LightCurve$ objects. The resulting object is then used as the base for the detection of flares. This removes all longterm trends like brightness changes due to spot modulation or similar, while retaining short term events like flares or transits. A similar approach was used by Ilin and Poppenhaeger (2022).

The next step is then to call $calculateFlareFitsForLightcurve()$ with the flattened lightcurve as well as the normalized lightcurve as parameters. It returns two lists of python dictionaries with the data for the flare peak as well as a fit which is described in the following paragraphs. It parses the flattened lightcurve with the scipy $find\_peaks$ function. This function returns local maxima, which can be further filtered by their minimum height (optional) as well as the minimum distance of datapoints (optional). Afterwards the found peaks are sorted by height, and the highest 100 are returned. This was found to be a good amount as the largest number of flares per "fits" file found in this study were around 70 for CD-56 1032A and B.

Afterwards each individual peak is checked. The first step is to estimate a flare starting and end point. This is done by checking the datapoints before and after the peak. If it finds that the flux difference is below 0.005 for three consecutive datapoints, it stops, and assumes that the last checked point is the start/end of the flare. In the case it finds an infinite or NaN value (which can happen if there are gaps in the lightcurve data), or it reaches 100 datapoints before/after it will stop. This was found to cover most flares detected and provides a sufficient number of datapoints for the following steps.

Afterwards multiple checks are done. It first checks if the datapoints right before and after the peak are above a threshold of 0.003 (0.3%) above the mean flattened flux, or if the two datapoints right after the peak are above that threshold (which is a similar approach to Araújo and Valio (2021)). Afterwards it is checked if the datapoint at two indices before the peak is larger than the datapoint right before the registered peak. This eliminates possible false positives which were found by manually inspecting previously found events, but could not be guaranteed to be two seperate events. In such cases it will only count one flare. Then the flare lightcurve is fitted. For the impulsive phase, a gaussian function is used and for the gradual phase an exponential function is used to account for the exponential decay in flare lightcurves (similar approach to Ilin and Poppenhaeger (2022) and Doyle et al. (2018)). Then the residual sum of squares (RSS) between the fit and the flux of the flare, as well as the total sum of squares (TSS) are calculated. Afterwards R-squared is calculated, and if it is below 0.8, the flare is rejected as the flare would not have the typical form. In the last step, the locations of the flare in the normalized and flattened lightcurve are compared. This step has been introduced, as in some rare cases the flattening algorithm can produce a large artificial spike (values of 10 or higher when normalized).

3.2.2 Lightcurve folding

This section mainly describes how the $getOptimizedFold()$ function works. This function was written to optimize the lightcurve folding, to improve accuracy for the folding and lightcurve fitting process. It uses the normalized lightcurve as well as the preferred fitting function type (see chapter 2.2) as parameters. The fit type can either be "sine" for a sine fit, "poly" for a polynomlial fit, or "linear" for a linear fit. The default value is "sine", but can be changed for each individual star in the GUI. The function at first generates two periodograms with the $to\_periodogram$ function from the lightkurve python package. The first one uses the Lomb-Scargle algorithm, while the second one uses the box-least-squares algorithm. Afterwards the four highest peaks of each are taken and converted into periods (unit in days). Then each period found by each algorithm is compared with the periods found by the other, and in the case of a match (absolute value of the difference between the values of the two algorithms is smaller than 5% of the larger of the two periods) this is now used as the rotational period as well as the spot modulation period. If it does not find a match, it uses the period corresponding to the highest peak in the Lomb-Scargle periodogram. Afterwards it calculates the epoch time to the first minimum in the lightcurve using numpys $argrelextrema$ function. In the following loop, which is repeated up to 30 times, the lightcurve is folded (using the lightkurve $fold$ function) with the spot modulation period, and the epoch set to the first minima in the lightcurve. Then a fit is performed using the prefered fitting method. If the fitting process fails for the preferred fitting type, and it was set to "sine", it will fall back to "poly" (polynomial fit), and vice versa. If the resulting fit has two maxima, and they are further away from the edges than 10% of the used period, the algorithm checks if there is a signal for half the used period in any of the two periodograms. If this is the case, it will use this as the period for spot modulation. It will save the current folded lightcurve as folded by rotational period, and generate a new folded lightcurve with the newly found spot modulation period. Afterwards it checks the location of the minimum of the spot modulation folded lightcurve. If the minimum is within 1% of half the phase it will stop. If not, it will shift the epoch by the difference of the minimum to zero, which is the center of the folded lightcurve phase, and repeat the folding process.

The function then returns the rotational period, the spot modulation period, the periods found by both periodograms as well as the folded lightcurve, the corresponding phase and the fit and fit type ("sine", "poly" or "linear") as well as the epoch. If the spot modulation differs from the found rotational period, it will also return the folded lightcurve, phase, fit and fit type of the rotational period folded lightcurve. The last returned value is "isValid", which is set to false if the algorithm does not find a fit with its minimum at half the phase for the spot modulation period folded lightcurve within 30 iterations.

3.3 Spectral type classification

After the initial download and cross checking with SIMBAD, not all stars had a spectral type assigned. For these stars magnitudes in different wavelength bands were available. The stars with known magnitudes at least in the B and V bands are given in table 3.1, while the stars with only J, H and K bands are given in table 3.2. The B-V color index as well as other color indices (if available) have been compared to the table in Reid (2025) (https://www.stsci.edu/~inr/intrins.html). This allowed a rough classification of the stars in table 3.1. Additionally, also the effective temperature was taken into account from the TESS Input Catalogue (Stassun et al., 2019) from Vizier (Ochsenbein F. et. al, n.d.). The classification table for spectral types based on effective temperature has been taken from Berlind (2025) (https://lweb.cfa.harvard.edu/~pberlind/atlas/htmls/note.html).

The final spectral type for the stars can be found in table 3.3. If the spectral type calculated from the effective temperature and the indices is identical, it will use that spectral type as final. In the case of those differing, like for BD-08 995, which was found to be an early K type star (K0) by the intrinsic color method but being a G type star based on the effective temperature, the latter is prefered. For the four stars from table 3.2 which have no B or V measurements, the spectral type based on the effective temperature is used.

Table 3.1.: List of stars with no spectral type entry in SIMBAD, but available magnitudes in the B and V bands. Main Identifier according to SIMBADs "MAIN_ID" property, as well as TESS Input Catalogue and Kepler Input Catalogue numbers are given.

Main Identifier	TIC	KIC
1RXS J064643.6-770027	TIC 177255827	-
BD-08 995	TIC 43472154	-
CPD-19 878	TIC 93125144	-
PM J07058-5848	TIC 279615427	-
TYC 1360-957-1	TIC 247117382	-
TYC 4595-107-1	TIC 394030788	-

Table 3.2.: List of stars with no spectral type entry in SIMBAD, but available magnitudes in the J, H and K bands. Main Identifier according to SIMBADs "MAIN_ID" property (2MASS), as well as TESS Input Catalogue and Kepler Input Catalogue numbers are given.

Main Identifier	TIC	KIC
2MASS J18524052+4156057	-	KIC 6500181
2MASS J18534407+4208274	-	KIC 6668646
2MASS J18535462+4135227	-	KIC 6183672
2MASS J19335656+4010546	-	KIC 5016904

Table 3.3.: Final determined spectral types. Main Identifier taken from SIMBAD. The column B-V contains the value of B-V calculated from the respective magnitudes taken from SIMBAD. The columns T_{eff}, Mass and Radius contain the effective temperature, mass and radius for the star taken from the TESS Input Catalogue from Vizier. The column Spectral Type (B-V) contains the determined spectral type based on Reid (2025), while the column Spectral Type (T_{eff}) contains the spectral type based on the effective temperature from Berlind (2025). The last column contains the spectral type which is used in this study.

Main Identifier	B-V	T_{eff} $[K]$	Mass $[M_\odot]$	Radius $[R_\odot]$	Spectral Type (B-V)	Spectral Type (T_{eff})	Final Spectral Type
1RXS J064643.6-770027	1.320000	4082	0.640	0.654	K7.0	K	K
BD-08 995	0.820000	5316	0.920	0.905	K0.0	G	G
CPD-19 878	1.087001	4852	0.790	0.893	K5.0	K	K
PM J07058-5848	1.320001	4250	-	0.409	K7.0	K	K
TYC 1360-957-1	0.970000	4870	0.790	0.636	K3.0	K	K
TYC 4595-107-1	0.750000	5231	0.890	0.902	G8.0	G	G
2MASS J18524052+4156057	-	3559	0.577	0.587	-	K	K
2MASS J18534407+4208274	-	3637	0.534	0.538	-	K	K
2MASS J18535462+4135227	-	3735	0.619	0.639	-	K	K
2MASS J19335656+4010546	-	3495	0.384	0.393	-	M	M

4 Results

This chapter includes the main results of this study. The data for the plots in this section were generated using the "New FC" Button from the main GUI described in section 2.3. As every star has a different rotational/spot modulation period, the value range for the phases of the folded lightcurves do not match. To compare different stars (or spot modulation periods for the same star) with each other, the phase was normalized from 0 to 2π.

The results contain plots for the different spectral types M, K, G, and F as well as combined results of every possible combination. Additionally for all these possible combinations, plots with data limits, e.g. only stars with a rotational period of less than 2 days or minimal/maximal normalized flare peak limits, were also generated. Moreover plots for stars according to their spectral sub type like M0 or G5 were created. Furthermore there is a selection of individual star results. For every plot group a CSV file is generated, which contains information about every star and flare used to generate the plot. The results also only contain the data of folded lightcurves which could be fitted with a sine function and less than 30 iterations of the fold optimization. The data which uses polynomial fits or both sine and polynomial fits as well as all plots and the accompanying CSV files are available at `https://gitlab.com/SGCMarkus/flaredetector_results`.

4.1 M dwarfs

This section shows the results for 49 M dwarfs for which flares could be detected. The list of stars can be found in table A.2.

Figures 4.1a and 4.1b show flare count histograms, with 10 and 30 phase bins respectively, of the number of flares depending on the normalized phase. Looking at figure 4.1a there is an even distribution, within the error, of flares across the normalized phase, with the exception of the bin at phase 0.5π. The bin at phase 0.5π shows a significant dip of roughly twice the error below the surrounding bins. Looking at the same data, just with 30 instead of 10 bins (figure 4.1b), the same dip is visible. In this figure the dip spans 3 bins. Additionally there are additional dips around phase 0.7π, 1.3π and 1.4π. Including the error, the major dip (which

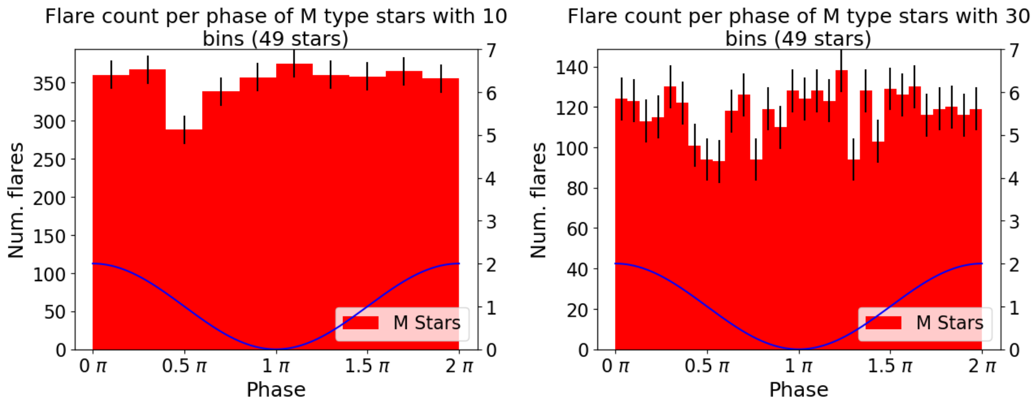

(a) 10 bins **(b)** 30 bins

Fig. 4.1.: Histogram showing the number of flares per phase of 49 M dwarfs for which a total of 3523 flares could be detected. The x-axis represents the normalized phase of the folded lightcurves. There are 10 bins (a)/30 bins (b) of the phase, showing the number of flares per bin. The error bar shows the standard deviation for the histogram. The blue line indicates an idealized phase (sine curve), with the maximum at phase $0\pi/2\pi$ and the minimum at phase 1π.

was already visible in figure 4.1a) is still significantly below the surrounding bins. The same is true for the dips at phases 0.7π and 1.3π. The dip at phase 1.4π on the other hand is not significant. Due to the dips surrounding the minimum at phase 1π, it looks like there is an increased number in flares around the phase minimum as well as phase maximum.

Filtering the data by the minimal flare peak, meaning only taking flares into account which have a normalized flare peak of greater than a fixed threshold (an example of flare peak distributions is seen in figures 4.16), is shown in figures 4.2a to 4.3b. There are more flares in the minima at phase 1π (more/bigger star spots) and maxima at phase 0 and 2π (less/smaller star spots) compared to the phase transition regions (phase regions between maximum and minimum). Taking a closer look at figure 4.2a, which accounts only for normalized flare peaks greater than 1.25 with 10 bins, the same dips (around phases 0.5π and 1.5π) as in the previous figure (figure 4.1b) are visible. Comparing those to the dip visible in figure 4.1a, it widened by 1 bin. From phase $\sim 1.7\pi$ to 2π there is a major peak. The same data, just with 30 bins can be seen in figure 4.2b. Peaks in this histogram appear at the same phases as in the histogram with 10 bins. Even though those bins are now partially seperated by bins with a low flare count at phases $\sim 0.2\pi$, 1π and $\sim 1.8\pi$. Additionally, at around phase 0.6π, there is now a smaller peak visible, while there was none in the histogram with 10 bins.

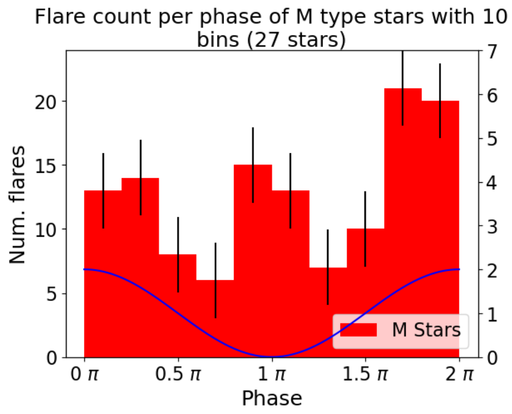

(a) 10 bins

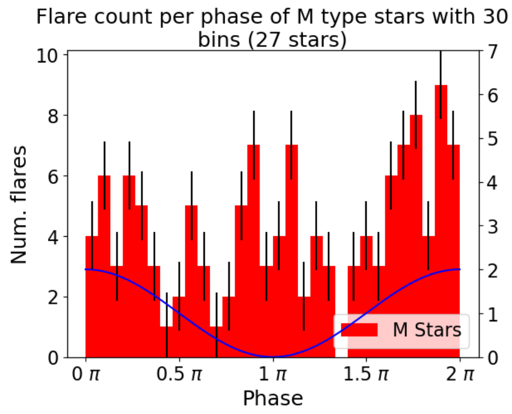

(b) 30 bins

Fig. 4.2.: Histograms showing the number of flares with a normalized peak of greater than 1.25 per phase of 27 M dwarfs for which a total of 127 such flares could be detected. The x-axis represents the normalized phase of the folded lightcurves. There are 10 (a) /30 (b) bins of the phase, showing the number of flares per bin. The error bar shows the standard deviation for the histogram. The blue line indicates an idealized phase (sine curve), with the maximum at phase $0\pi/2\pi$ and the minimum at phase 1π.

Increasing the normalized minimal flare peak threshold further to 1.5 decreases the total number of flares further, which results in a comparatively large error. This makes the error half the size or even larger than some of the bins in figure 4.3a. Nontheless it is visible that the largest flares seem to appear more often around phase 1π and phase $0\pi/2\pi$. Increasing the number of bins to 30 (see figure 4.3b) causes very large error bars which do not allow any proper analysis.

Doing the opposite and only plotting the histograms for flares with normalized peaks of less than 1.01 can be seen in figure 4.4. Figure 4.4a shows a similar picture to the histogram with no filtering (see figure 4.1a). The difference here though is that there are less flares in the phase region surrounding the minima around phase 0.5π to 1.5π. Increasing the resolution to 30 bins (figure 4.4b) shows overall a similar pattern, even though the scatter of bins, especially in the center during the phase minima are larger than twice the error.

Limiting the normalized flare peaks to <1.05 (figure 4.5) shows again a similar pattern as seen in the histograms with all data. In figure 4.5a the major difference is that there is a peak around normalized phase 1.1π. The difference becomes less obvious when increasing the bin size 30 (figure 4.5b). While it is similar to figure 4.1b, there appears a new dip around phase 0.25π which appears right after the maximum. Also the shape of the peak consisting of multiple bins around phase 1.1π changed slightly compared to the one in figure 4.1b.

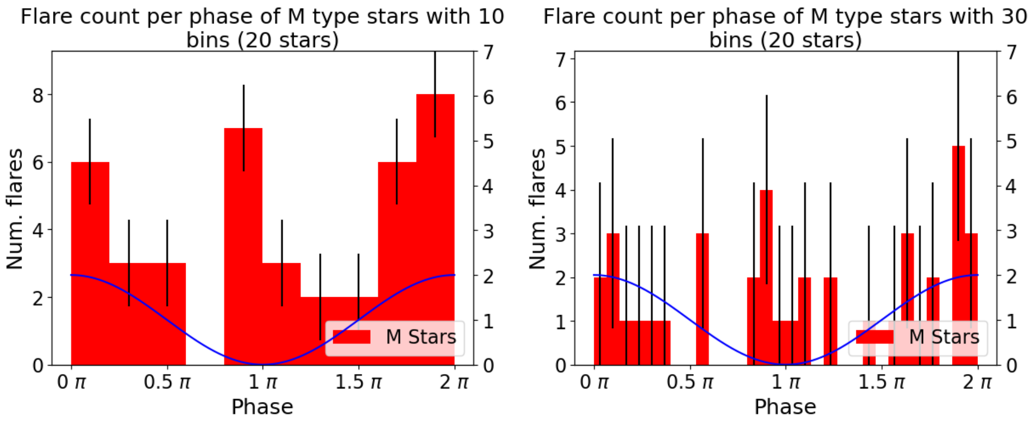

(a) 10 bins (b) 30 bins

Fig. 4.3.: Histograms showing the number of flares with a normalized peak of greater than 1.5 per phase for 20 M dwarfs for which a total of 40 such flares could be detected. The x-axis represents the normalized phase of the folded lightcurves. There are 10 (a)/30 (b) bins of the phase, showing the number of flares per bin. The error bar shows the standard deviation for the histogram. The blue line indicates an idealized phase (sine curve), with the maximum at phase $0\pi/2\pi$ and the minimum at phase 1π.

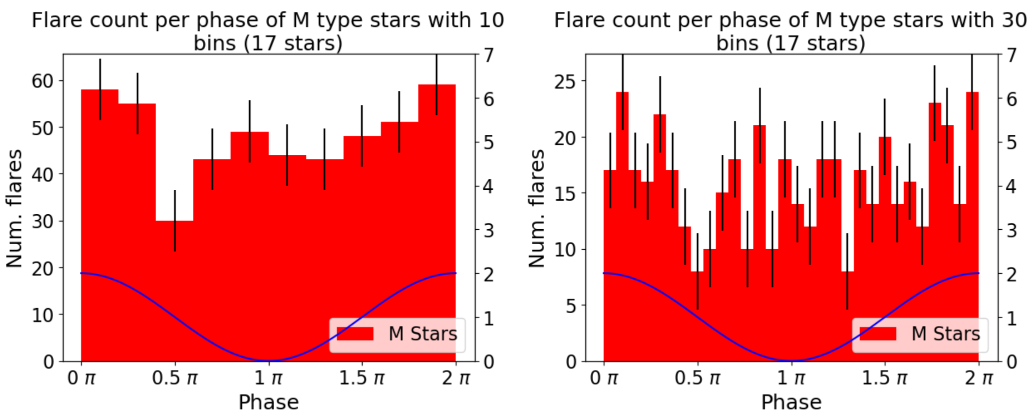

(a) 10 bins (b) 30 bins

Fig. 4.4.: Histograms showing the number of flares with a normalized peak of less than 1.01 per phase of 17 M dwarfs for which a total of 480 such flares could be detected. The x-axis represents the normalized phase of the folded lightcurves. There are 10 (a)/30 (b) bins of the phase, showing the number of flares per bin. The error bar shows the standard deviation for the histogram. The blue line indicates an idealized phase (sine curve), with the maximum at phase $0\pi/2\pi$ and the minimum at phase 1π.

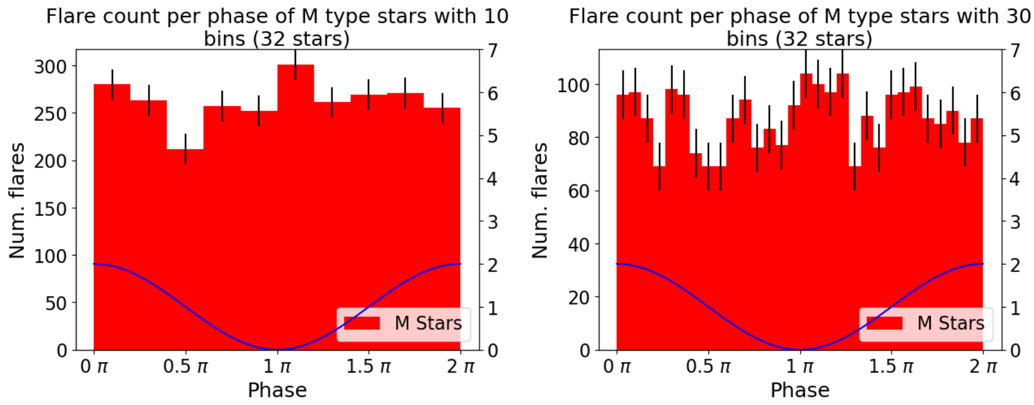

(a) 10 bins

(b) 30 bins

Fig. 4.5.: Histograms showing the number of flares with a normalized peak of less than 1.05 per phase of 32 M dwarfs for which a total of 2621 such flares could be detected. The x-axis represents the normalized phase of the folded lightcurves. There are 10 (a)/30 (b) bins of the phase, showing the number of flares per bin. The error bar shows the standard deviation for the histogram. The blue line indicates an idealized phase (sine curve), with the maximum at phase $0\pi/2\pi$ and the minimum at phase 1π.

4.2 K dwarfs

This section shows the results for 21 K dwarfs for which flares could be detected. A full list of the stars used can be found in table A.3.

Figure 4.6a shows the number of flares per phase with 10 bins of 21 K type dwarfs used in the present study. One can see a slight increase in the number of flares between the maximum and minimum of the lightcurve at phase 0.5π, and a slight decrease between minimum and maximum at phase 1.5π. There is also a peak around 1π with ~95 flares compared to the 60-80 flares per bin in the rest of the histogram. One of the major contributions is V* V471 Tau. The individual results for this star are presented in section 4.6. Looking at the same dataset with 30 bins for the histogram (figure 4.6b), the peak in the phase minimum at 1π is still visible. Additionally there appear more peaks at phase $> 1.3\pi$ $(1.3,\ 1.6,\ 1.9\pi)$, while the number of flares between phase 0π and 0.5π shows a slightly increasing trend in the number of flares. We see a larger dip right before and after the big peak at phase 1π which was also visible in figure 4.6a (10 bins). The major dips at phase 0.7π, 1.3π, 1.6π and 1.9π are significant to 1 σ, while the smaller ones between phase 0π and 1π are within the errors.

The histograms with normalized flare peaks limited to >1.05 are shown in figure 4.7. In figure 4.7a the histogram with 10 bins is shown, while figure 4.7b shows the histogram with 30 bins. There are multiple significant peaks visible in figure 4.7a.

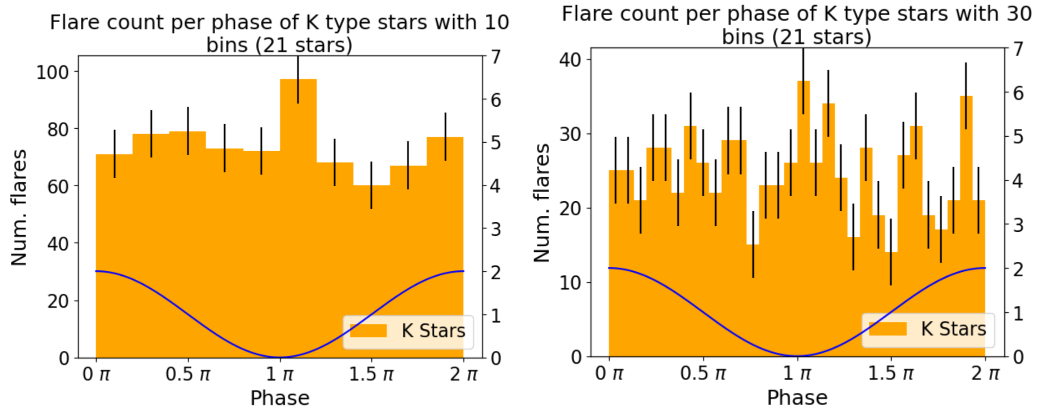

(a) 10 bins (b) 30 bins

Fig. 4.6.: Histogram showing the number of flares per phase of 21 K dwarfs for which a total of 742 flares could be detected. The x-axis represents the normalized phase of the folded lightcurves. There are 10 bins (a)/30 bins (b) of the phase, showing the number of flares per bin. The error bar shows the standard deviation for the histogram. The blue line indicates an idealized phase (sine curve), with the maximum at phase $0\pi/2\pi$ and the minimum at phase 1π.

The two highest being at phases 0.7π as well as 1.1π. From phase 1.1π onwards we see a decrease in the number of flares. These two peaks are seperated by a bin at phase 0.9π which is significantly lower (roughly twice the error). Moreover, we also see a peak at phase 0π which is slightly smaller than the other two at 0.7 and 1.1π. A similar picture forms when increasing the resolution to 30 bins (figure 4.7b). The main differences to figure 4.7a is though that the heights of the aformentioned peaks is now the same, and that the errorbars are of course larger than for the 10 bin representation. Additionally a new peak in the last bin, during the phase maximum, appeared having the same height as the other three peaks.

Similar to figures 4.4 and 4.5, we also show the histograms of flares with a normalized peak threshold of less than 1.01 and 1.05. In figure 4.8a, where we show the histogram of flares with a peak <1.01, there appears a siginificantly large peak around phase 1.2π which is at the phase minimum. Another, slightly smaller peak appears at the phase maximum at 1.9π. Both of these peaks are significant when comparing them to their surrounding bins. Checking for more specific phases for the peaks, by increasing the resolution to 30 bins, shows siginificant peaks at phases 1.6π and 1.9π. These two bins stand out with respect to their neighbouring bins.

Increasing the maximum flare peak threshold to 1.05 in figure 4.9 reveals a similar pattern as shown in figure 4.5 with the data for M dwarfs. The histogram is similar to the ones using all available flare data for K dwarfs (figure 4.6). The differences of figure 4.9a, which shows the histogram with 10 bins with flare peaks limited to

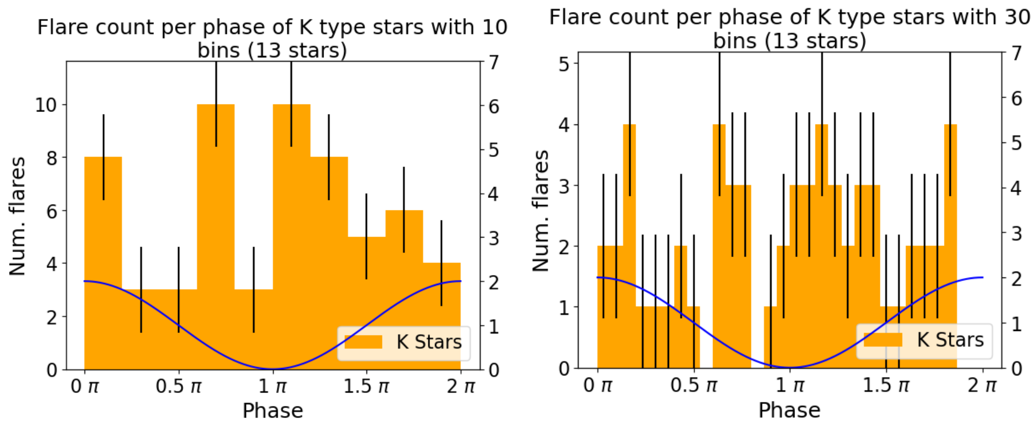

(a) 10 bins **(b)** 30 bins

Fig. 4.7.: Histograms showing the number of flares with a normalized peak of greater than 1.05 per phase of 13 K dwarfs for which a total of 60 such flares could be detected. The x-axis represents the normalized phase of the folded lightcurves. There are 10 (a)/30 (b) bins of the phase, showing the number of flares per bin. The error bar shows the standard deviation for the histogram. The blue line indicates an idealized phase (sine curve), with the maximum at phase $0\pi/2\pi$ and the minimum at phase 1π.

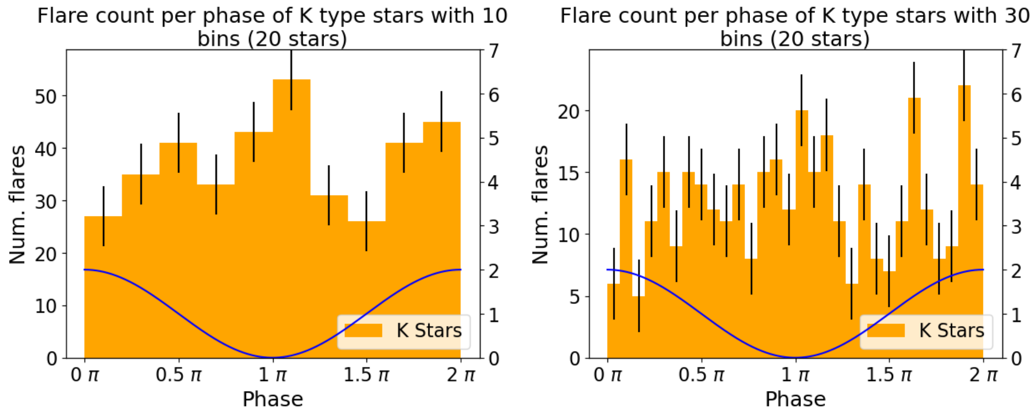

(a) 10 bins **(b)** 30 bins

Fig. 4.8.: Histograms showing the number of flares with a normalized peak of less than 1.01 per phase of 20 K dwarfs for which a total of 375 such flares could be detected. The x-axis represents the normalized phase of the folded lightcurves. There are 10 (a)/30 (b) bins of the phase, showing the number of flares per bin. The error bar shows the standard deviation for the histogram. The blue line indicates an idealized phase (sine curve), with the maximum at phase $0\pi/2\pi$ and the minimum at phase 1π.

<1.05, and 4.6a, which shows the histogram with 10 bins for all detected flares of K dwarfs, is that that the two bins at around phase 0.3π to 0.5π are now more pronounced, even though still not outside of the error of their surrounding bins. Similarly the last bin at around phase 1.9π is more pronounced. Increasing the bins to 30 (figure 4.9b) shows a very similar figure compared to figure 4.6b.

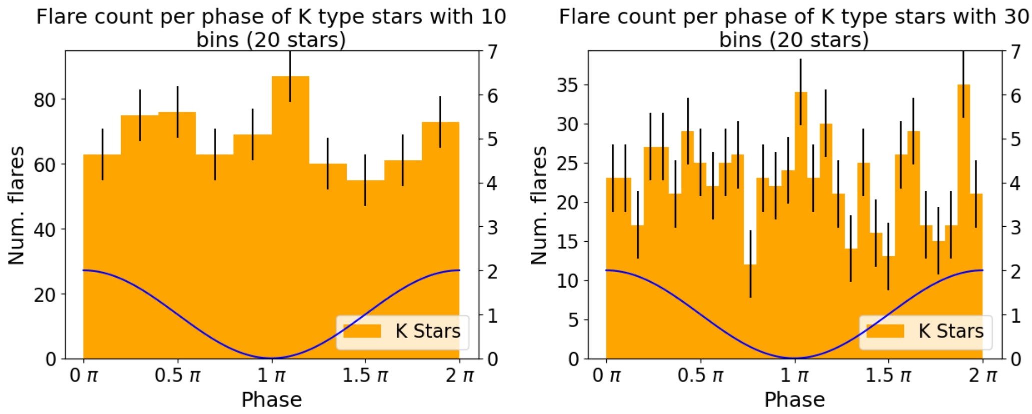

(a) 10 bins

(b) 30 bins

Fig. 4.9.: Histograms showing the number of flares with a normalized peak of less than 1.05 per phase of 20 K dwarfs for which a total of 682 such flares could be detected. The x-axis represents the normalized phase of the folded lightcurves. There are 10 (a)/30 (b) bins of the phase, showing the number of flares per bin. The error bar shows the standard deviation for the histogram. The blue line indicates an idealized phase (sine curve), with the maximum at phase $0\pi/2\pi$ and the minimum at phase 1π.

4.3 G dwarfs

This section shows the results for 21 G dwarfs for which flares could be detected. Table A.4 contains a list of all G type stars used.

The first histogram of all data of G type dwarfs with 10 bins in figure 4.10a shows a significant increase of flares occuring around phase 1π compared to the ones at phase $0\pi/2\pi$. The rise in flare number from phase 0π to 1.3π is gradual, while there is a steep fall off after the sixth bin at phase 1.1π. Due to the lower number of detected flares on G type stars, the error bars in figure 4.10b are rather large. The maximum of the histogram shown in figure 4.10a is now split into two peaks at phase 0.6π and 1π. An additional peak appears at phase 0.3π in figure 4.10b. This peak is significant with respect to its neighbouring bins. Right before this peak a significant dip is visible at phase 0.2π. From phase 1 to 2π we do not see any significant pattern.

Limiting the flare peaks to <1.05 (figure 4.11) does not significantly affect the histograms.

On the other side, looking at flares with peaks >1.05 reveals completely different histograms. Figure 4.12a shows the histogram with 10 bins, while figure 4.12b shows the one with 30 bins. The histogram with 10 bins shows 3 significant peaks. The first at around phase 0.5π with a width of 3 bins, the second at around 1.1π and

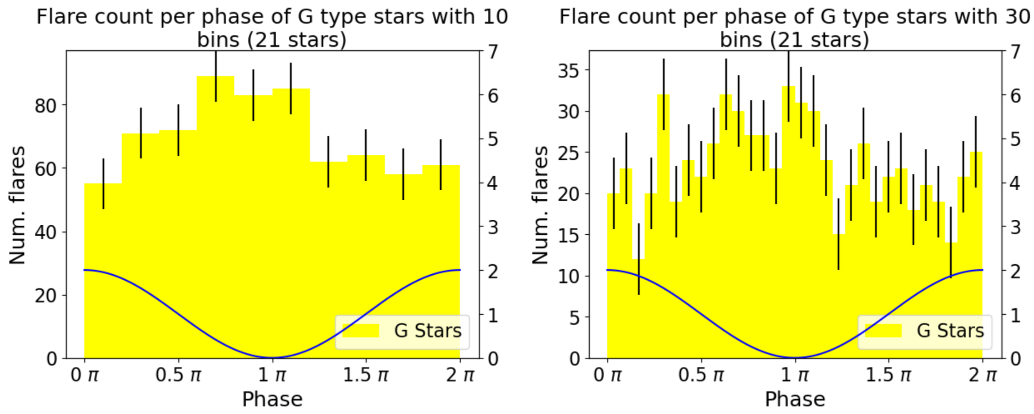

(a) 10 bins **(b)** 30 bins

Fig. 4.10.: Histogram showing the number of flares per phase of 21 G dwarfs for which a total of 700 flares could be detected. The x-axis represents the normalized phase of the folded lightcurves. There are 10 bins (a)/30 bins (b) of the phase, showing the number of flares per bin. The error bar shows the standard deviation for the histogram. The blue line indicates an idealized phase (sine curve), with the maximum at phase $0\pi/2\pi$ and the minimum at phase 1π.

the last at around 1.7π. All of these peaks lie significantly above their surrounding bins. Increasing the bins to 30, which is seen in figure 4.12b, does not give a clear picture, due to the overall lower total number of flares due to the threshold, and the increased bin count. Even though there are still singular bins at 0.4π, 1.1π and 1.7π which are larger than their surrounding, but well within the error range.

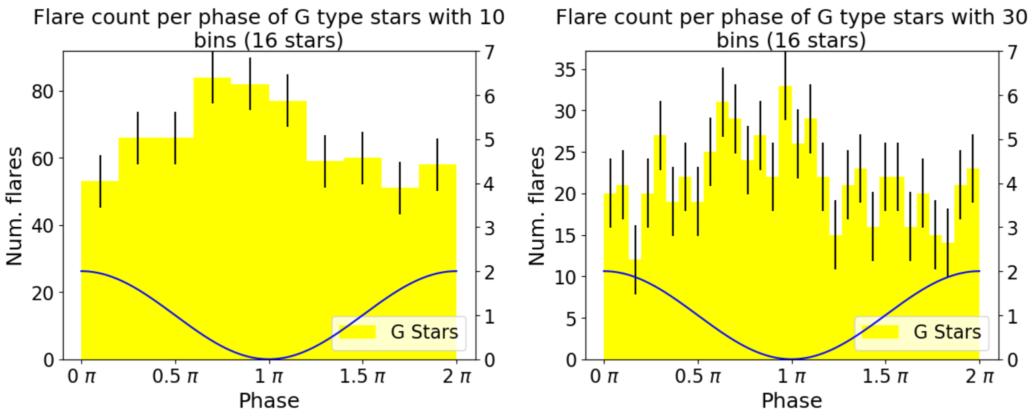

(a) 10 bins **(b)** 30 bins

Fig. 4.11.: Histograms showing the number of flares with a normalized peak of less than 1.05 per phase of 16 G dwarfs for which a total of 656 such flares could be detected. The x-axis represents the normalized phase of the folded lightcurves. There are 10 (a)/30 (b) bins of the phase, showing the number of flares per bin. The error bar shows the standard deviation for the histogram. The blue line indicates an idealized phase (sine curve), with the maximum at phase $0\pi/2\pi$ and the minimum at phase 1π.

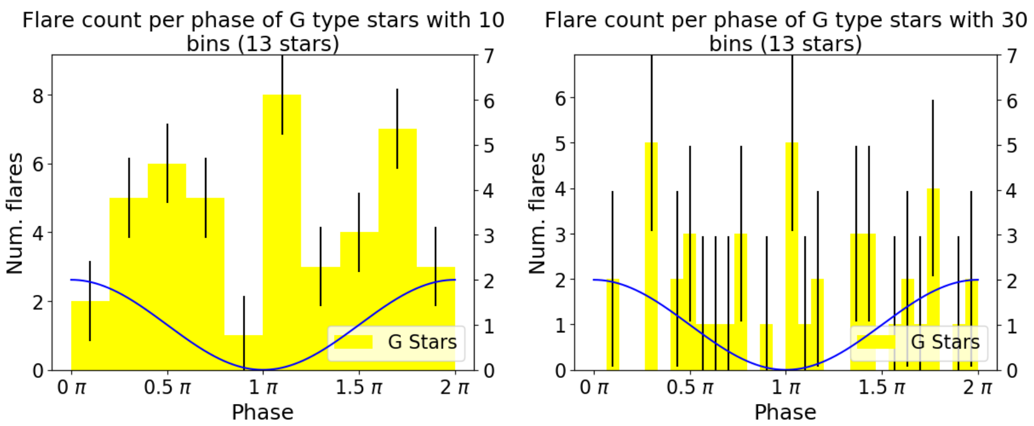

(a) 10 bins **(b)** 30 bins

Fig. 4.12.: Histograms showing the number of flares with a normalized peak of greater than 1.05 per phase of 13 G dwarfs for which a total of 44 such flares could be detected. The x-axis represents the normalized phase of the folded lightcurves. There are 10 (a)/30 (b) bins of the phase, showing the number of flares per bin. The error bar shows the standard deviation for the histogram. The blue line indicates an idealized phase (sine curve), with the maximum at phase $0\pi/2\pi$ and the minimum at phase 1π.

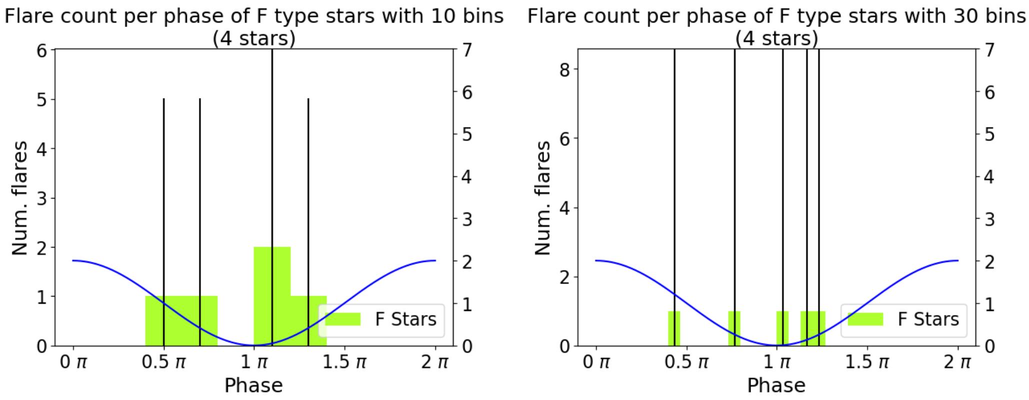

(a) 10 bins

(b) 30 bins

Fig. 4.13.: Histogram showing the number of flares per phase of four F dwarfs for which flares could be detected. The x-axis represents the normalized phase of the folded lightcurves. There are 10 bins (a)/30 bins (b) of the phase, showing the number of flares per bin. The error bar shows the standard deviation for the histogram. The blue line indicates an idealized phase (sine curve), with the maximum at phase $0\pi/2\pi$ and the minimum at phase 1π.

4.4 F dwarfs

This section shows the results for four F dwarfs for which a total of 5 flares could be detected. The list of F type stars can be found in table A.5.

The detected number of flares in the already low number of F type stars in this study in figures 4.13a and 4.13b is very low which causes large errorbars of the histogram. Nontheless all detected flares were around the minimum of the phasefolded lightcurves. However, due to the above mentioned large errorbars, the results of F-type main-sequence stars is not significant.

4.5 Combined results

The results combined for all 95 stars in the study for which flares could be detected is presented in this section. This includes the stars from tables A.2 to A.5. The histograms in figure 4.14a and 4.14b are stacked histograms. The flare number of the individual stars per bin are stacked on top of each other resulting in a total flare number histogram. Each color (red for M, orange for K, yellow for G and green for F type stars) represents the number of flares counted in the bin by the respective spectral type. For easier comparison, the histograms shown in the previous sections for M, K and G stars are shown again in figures 4.14c to 4.14h.

The dip at phase 0.5π which was present in the histogram for the M type stars (see figure 4.14c) dominates the total flare count histogram. From figures 4.14e/4.14f and 4.14g/4.14h one can see that no local minimum at phase 0.5π exists. The peak at phase 1π is a result of the data from the K and G type stars, as those show significant peaks in this bin. Due to the large number of overall flares, the errorbars are small and the peak in the center at phase 1π is significant. Looking at the same data with 30 bins over the phase in figure 4.14b, the histogram is shaped mostly by the data of the M type stars, which is clearly visible with the dip around phase 0.5π and 1.4π. Additionally the peaks from the data of K (figure 4.14f) and G (figure 4.14h) type stars cause a wider peak at around phase 1π. Additionally there are also smaller, especially less wide peaks at around phases 0.4π, 0.7π and 1.5π.

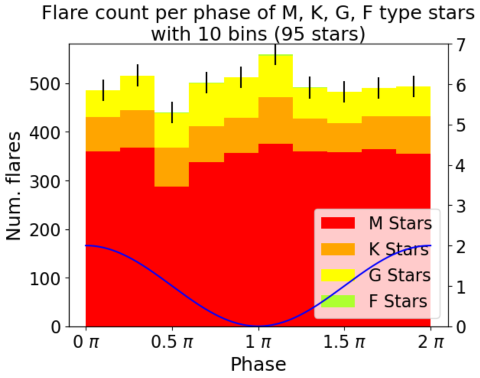

(a) M, K, G and F type stars, 10 bins

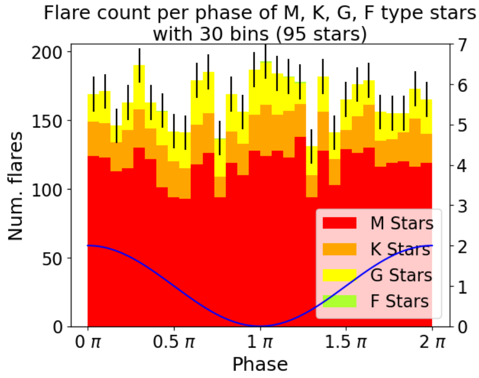

(b) M, K, G and F type stars, 30 bins

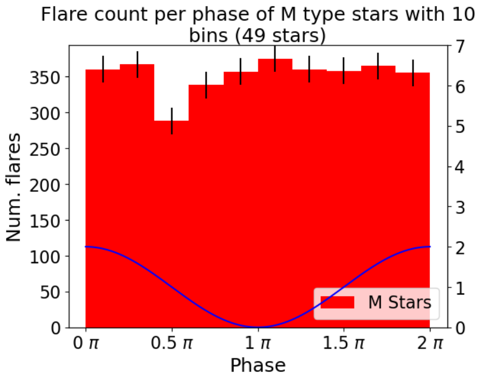

(c) M type stars, 10 bins

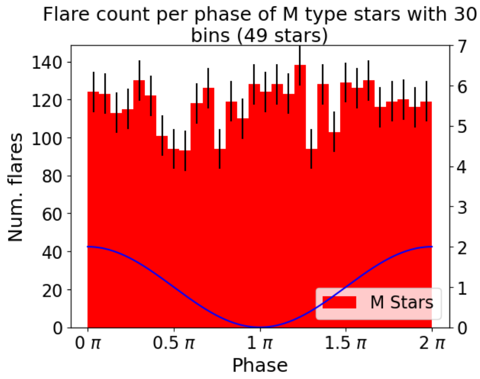

(d) M type stars, 30 bins

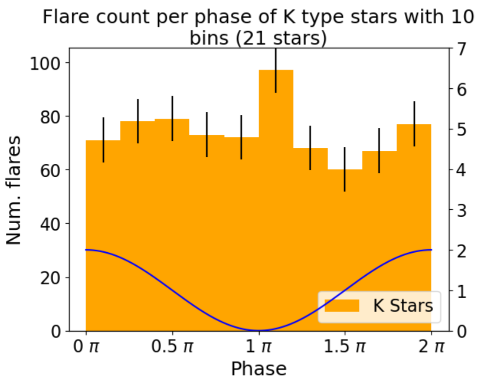

(e) K type stars, 10 bins

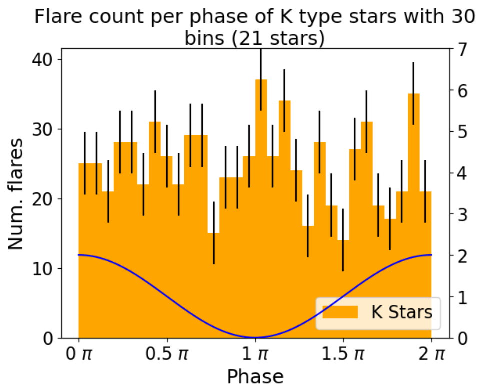

(f) K type stars, 30 bins

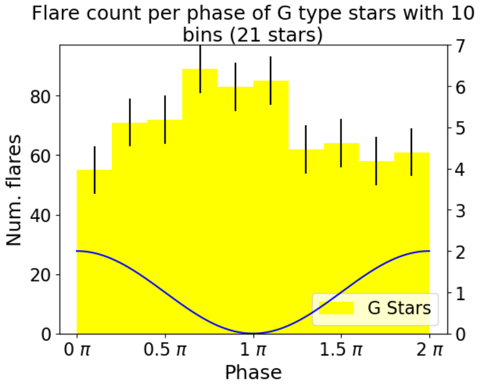

(g) G type stars, 10 bins

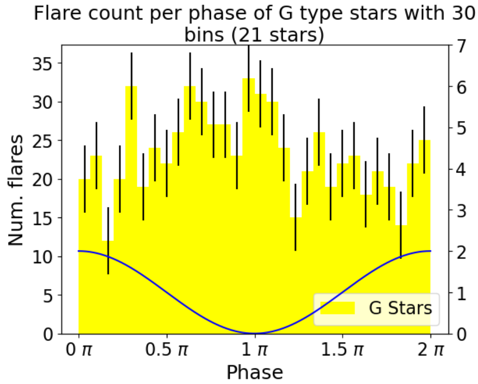

(h) G type stars, 30 bins

Fig. 4.14.: Histograms showing the number of flares per phase for all 95 dwarfs for which flares could be detected in panels a and b. Panels c to h repeat the histograms for spectral types M, K and G respectively as direct comparison (same as histograms shown in figures 4.1, 4.6 and 4.10).

4.6 Individual stars

This section contains a selection of results for individual stars. The results for this section were selected because either they represent the expected case of more flares on the more spotted hemisphere of the star but also the other way round, i.e. less flares on the more spotted hemisphere.

4.6.1 BD-08 995

BD-08 995, also known as TIC 43472154, is a G type main-sequence star with a surface temperature of 5316 K (Stassun et al., 2019), and a distance of ~87 pc (Wenger et al., 2000). It is a very active solar like star, producing over 200 superflares per year (Tu et al., 2020). It has a rotational period of 2.8 days (Tu et al., 2020). There are two TESS lightcurves available in sectors 5 and 32.

Looking at figure 4.15a, which shows the flare distribution across the normalized phase of the folded lightcurves with 10 bins, one can see a clear peak at phase 1π. The bins forming the peak are significantly enhanced with respect to the neighbouring bins. The bins of the phase maxima also show a slight increase in flare activity at phase $0/2\pi$ compared to the phase transition regions around phase 0.5π (maximum to minimum) and 1.5π (minimum to maximum). The peaks at the phase maxima are not as significant as the peaks in phase minimum. Figure 4.15b shows the same data just with 30 bins instead of 10, but less significant. It shows a similar picture as the previous figure. But due to the low number of total detected flares, and a relatively large bin count, the errorbars become large compared to the individual bins. Due to this, the errorbars of most bins overlap with each other, with the exceptions of the the first bin at phase 0π and the bin at phase $\sim 1.1\pi$, which errorbars only overlap with other larger bins like the ones at phase $\sim 0.9\pi$ and $\sim 1.4\pi$.

The distribution of normalized flare peaks for BD-08 995 in figure 4.16 shows that the highest flare peak appeared around phase 0.1π with a peak of ~1.11. Other high flare peaks were detected at phases $\sim 1\pi$ and $\sim 1.9\pi$.

Looking at the folded TESS lightcurves of sector 5 (4.17a) and 32 (4.17b) one can see the earlier presented distribution of flares and their peaks. In TESS sector 5 there appear comparatively many flares around phase -0.2 (not normalized, scaled between -phase/2 and +phase/2). The highest detected flare peak which was mentioned prior was detected in the TESS sector 32 lightcurve at phase -1.2.

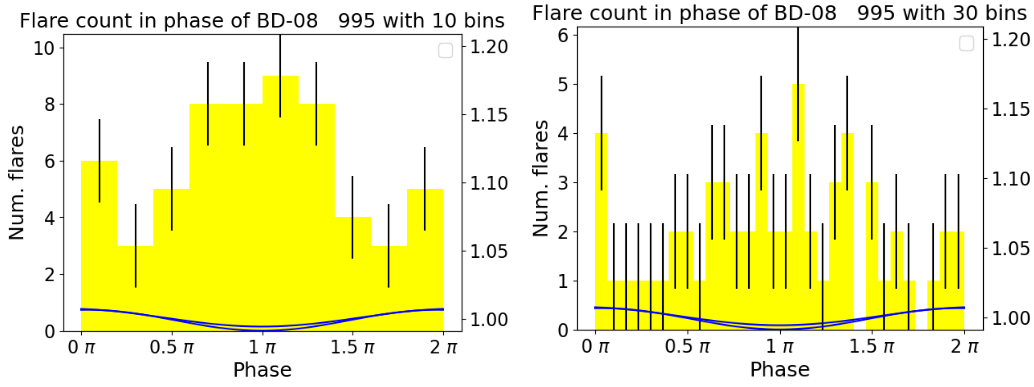

(a) 10 bins **(b)** 30 bins

Fig. 4.15.: Histograms of BD-08 995 across the phase showing the number of flares in each bin with a total of 59 flares. The error bar shows the standard deviation for the histogram. The blue lines show the various fits for the folded lightcurves used to generate the data, with the phase minimum at 1π and phase maximum at $0\pi/2\pi$.

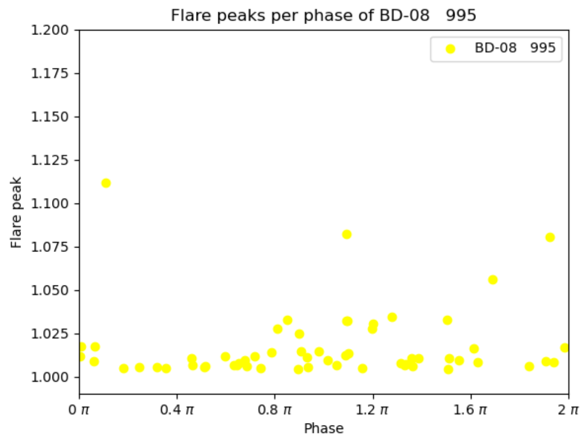

Fig. 4.16.: Distribution of flare peaks in relation to the normalized phase at which they occured for BD-08 995. The y-axis shows the flare peak and the x-axis shows the normalized phase.

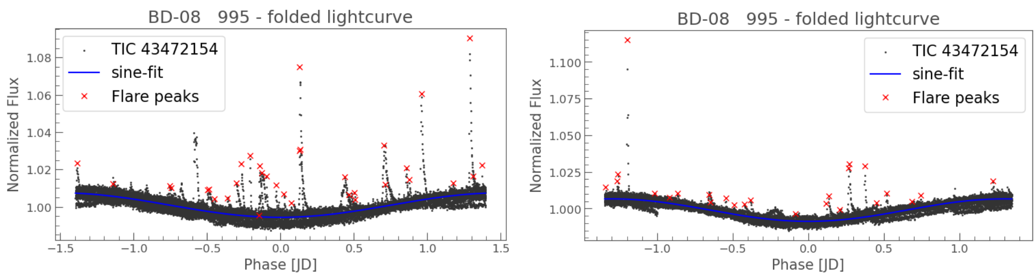

(a) TESS Sector 5 **(b)** TESS Sector 32

Fig. 4.17.: Folded lightcurves for BD-08 995. The blue lines show the calculated sine fits. The red crosses indicate the detected flare peaks.

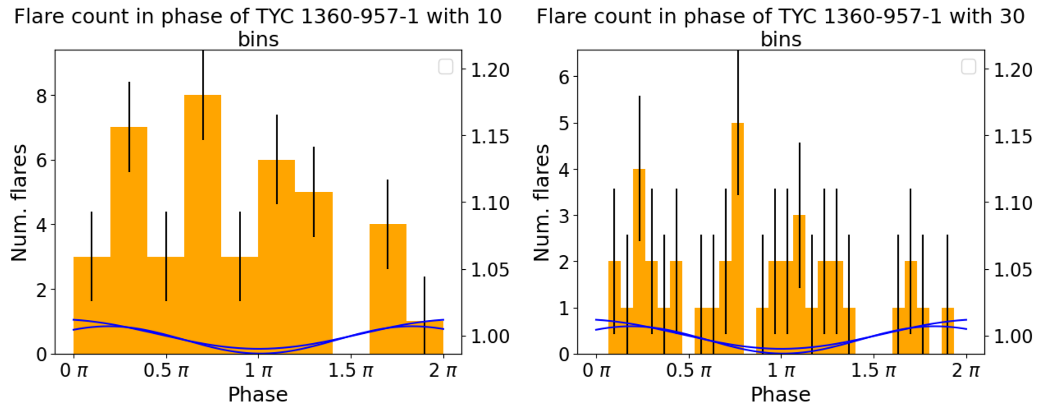

(a) 10 bins **(b)** 30 bins

Fig. 4.18.: Histograms of TYC 1360-957-1 across the phase showing the number of flares in each bin with a total of 40 flares. The error bars show the standard deviation for the histogram. The blue lines show the various fits for the folded lightcurves used to generate the data, with the phase minimum at 1π and phase maximum at $0\pi/2\pi$.

4.6.2 TYC 1360-957-1

Not much is published about TYC 1360-957-1. It has been categorized as spectral type K on SIMBAD (Wenger et al., 2000). It has the TESS Input Catalogue number 247117382, and has been observed by TESS in sectors 44, 45 and 46.

Looking at the flare distribution histogram with 10 bins for this star in figure 4.18a one can see that the largest peaks in order are at phase $\sim 0.7\pi$, $\sim 0.4\pi$ and $\sim 1.2\pi$, the last one being two bins wide. The first two are significant with respect to their neighboring bins and errors, while the third peak is only partly significant. Looking at the histogram with 30 bins of the same dataset (figure 4.18b), the first 2 peaks mentioned for the histogram with 10 bins are still pronounced. But compared to figure 4.18a, the low number of flares and the large number of bins result in a rather large error. Therefore these two peaks are not significant as those are within the error of the histogram.

Figure 4.19 presents the overall distribution of flares across the normalized phase detected for TYC 1360-957-1 in this study. The three largest flare peaks detected were at a normalized phase of $\sim 0.8\pi$, which is close to the phase minimum at 1π. This could indicate that they originate from the same spot or spot group. Three more larger flare peaks stand out at phase 1.2π. While they are not as large as the previous three, they have a higher peak than the rest of the detected flares.

The used folded lightcurves can be seen in figure 4.20. This figure is split into the three different TESS sectors. In the upper left panel of 4.20 the folded lightcurve of

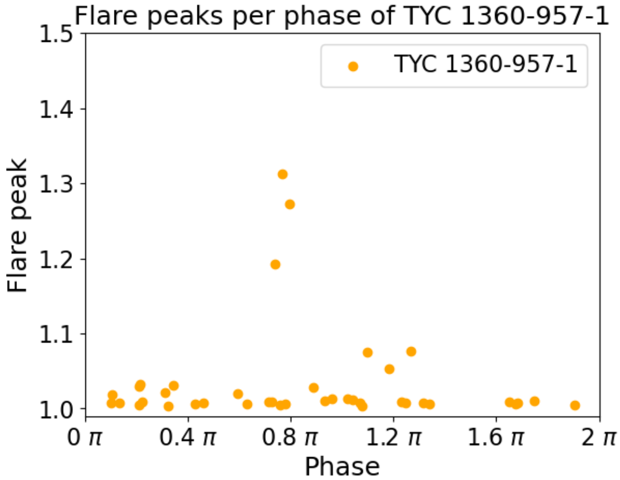

Fig. 4.19.: Distribution of flare peaks in relation to the normalized phase at which they occured for TYC 1360-957-1. The y-axis shows the flare peak and the x-axis shows the normalized phase.

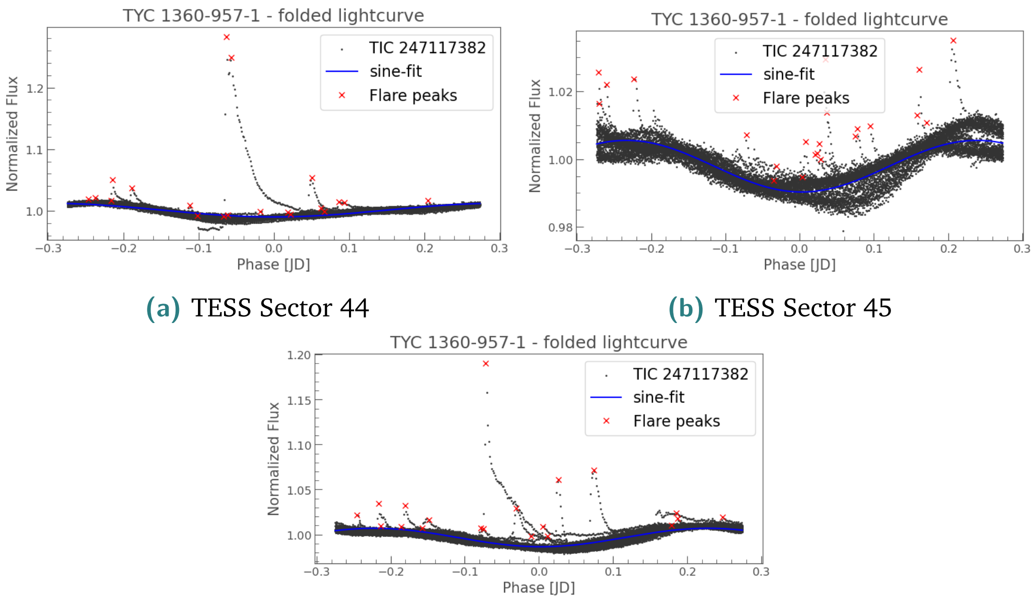

(a) TESS Sector 44

(b) TESS Sector 45

(c) TESS Sector 46

Fig. 4.20.: Folded lightcurves for TYC 1360-957-1. The blue lines shows the sine fits. The red crosses indicate the detected flare peaks.

sector 44 is shown. The minimum of the folded lightcurve is slightly shifted from the center. This is represented by the lowest point of the sine fit. One can also see that two large flares occured at the minimum of the phasefolded lightcurve. No such large flares can be seen in sector 45 (upper right panel of figure 4.20). Again in sector 46 (lower panel of figure 4.20) we see a large flare at the minimum of the phasefolded lightcurve.

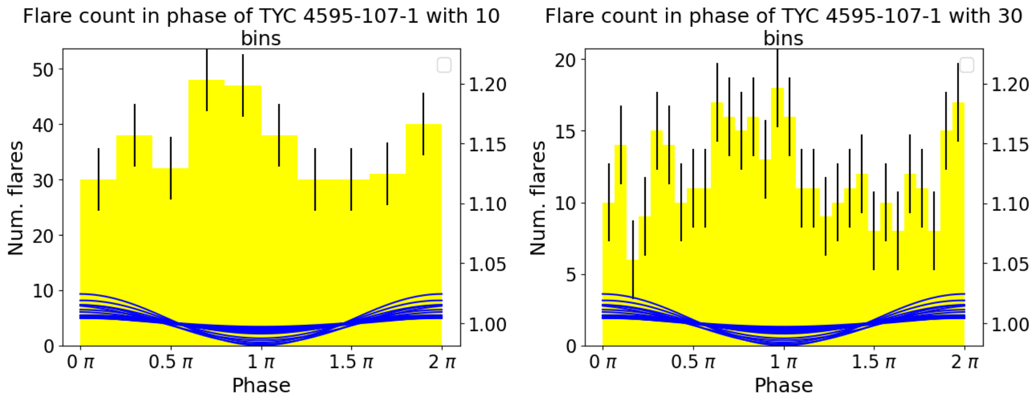

(a) 10 bins

(b) 30 bins

Fig. 4.21.: Histograms of TYC 4595-107-1 across the phase showing the number of flares in each bin with a total of 365 flares. The error bar shows the standard deviation for the histogram. The blue lines show the various fits for the folded lightcurves used to generate the data, with the phase minimum at 1π and phase maximum at $0\pi/2\pi$.

4.6.3 TYC 4595-107-1

TYC 4595-107-1, also known as TIC 394030788, is an active G-type main-sequence star with an effective temperature of 5231 K, a radius of 0.9 $R_\odot$ (Tu et al., 2021; Crowley et al., 2022), a mass of 0.89 $M_\odot$ (Crowley et al., 2022) and a rotational period of 3.3 days (Tu et al., 2021; Crowley et al., 2022) and was observed in 20 TESS sectors. The folded lightcurves for TYC 4595-107-1 can be found in appendix B.1.

The first histogram, figure 4.21a, with 10 bins shows the accumulated data for all 20 observed lightcurves. Due to the high number of available lightcurves, and TYC 4595-107-1 being a very active star (Tu et al., 2021; Crowley et al., 2022), the total flare count is very high. There seems to be a base level of flares per bin of around 30 over the phase, with a large and two bin wide peak at around phase 0.6 to 0.8π. This increase in flare number is sufficiently large to be outside of the error of the average distribution. Another peak, even though less significant as its errorbar overlaps with the surrounding bins, appears at the bin at phase 1.9π. A similar, but a bit weaker increase in flares can be seen at the bin at 0.2π. The histogram with 30 bins (figure 4.21b) shows a similar result. It shows an increase in flare number around phase 0.6 to 1π, as well as at 1.9 to 0.1π and 0.4π. Only the first mentioned peak managed to be large enough though, to be significantly above the error of the average distribution.

The flare peak of the normalized phase distribution can be seen in figure 4.22. The strongest flare was detected at normalized phase $\sim 0.8\pi$. Also, pronounced flare

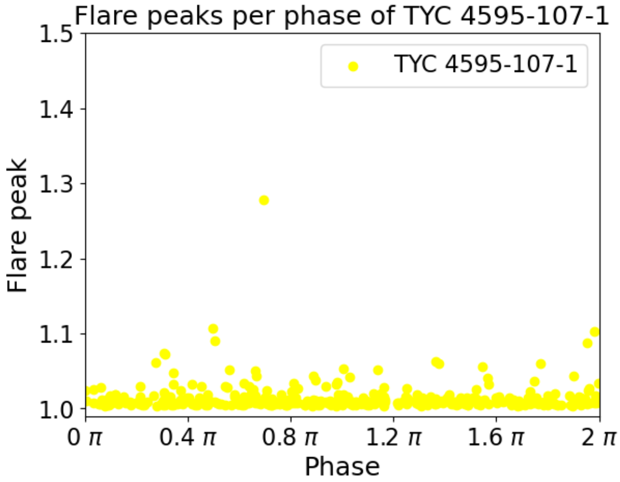

Fig. 4.22.: Distribution of flare peaks in relation to the normalized phase at which they occured for TYC 4595-107-1. The y-axis shows the flare peak and the x-axis shows the normalized phase.

peaks have been detected at phases 0.5π and 2π respectively. Apart from that we do not see any other energetic flares. The majority of flares reveal flare peaks in the range of 1.01 to 1.05.

All of the folded lightcurves of TYC 4595-107-1 can be found in appendix B.1, figures B.1 and B.2.

4.6.4 V* V471 Tau

V471 Tau is a post-common envelope binary system consiting of a K2 and a white dwarf (Muirhead et al., 2022). The K2 dwarf has a dominant spot facing the white dwarf all the time, as the system shows a bound rotation (Kővári et al., 2021).

Figures 4.23a and 4.23b show the histograms of five TESS folded lightcurves for V471 Tau with 10 and 30 bins respectively. The TESS lightcurves used are from sectors 42, 43, 44, 70 and 71. The lightcurve of K2 target table ID 80 was rejected by the algorithm described in section 3.2. Due to the lightcurve spanning 90 days, and the variability due to spots, the folding and fitting algorithm could not produce a reliable output. The blue lines show the used fits for the individual folded lightcurves. In the first figure, there appear two different peaks. The first being at phase 0.5π, and the second one at phase 1.1π. These bins are significantly higher than the remaining bins with 13/15 flares respectively compared to 1 to 8 in the other bins. Increasing the bins to 30 (figure 4.23b) does not change the result much. Due to the individual flare count being lower per bin compared to figure 4.23a, the errorbars are comparatively larger. There are still peaks at $\sim 0.5\pi$ and 1π.

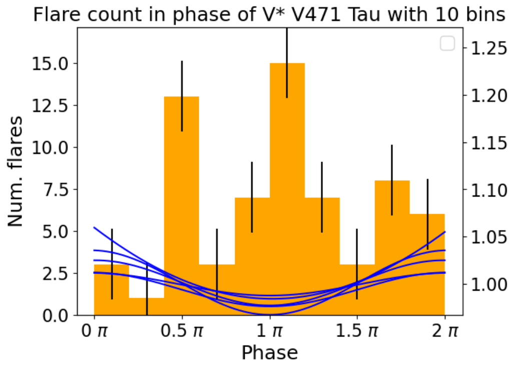

(a) 10 bins

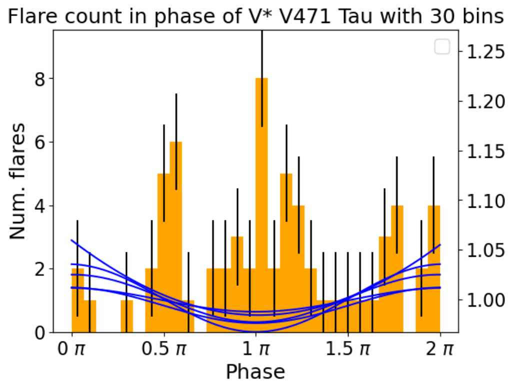

(b) 30 bins

Fig. 4.23.: Histograms of V471 Tau across the phase showing the number of flares in each bin with a total of 66 flares. The error bar shows the standard deviation for the histogram. The blue lines show the various fits for the folded lightcurves used to generate the data, with the phase minimum at 1π and phase maximum at $0\pi/2\pi$.

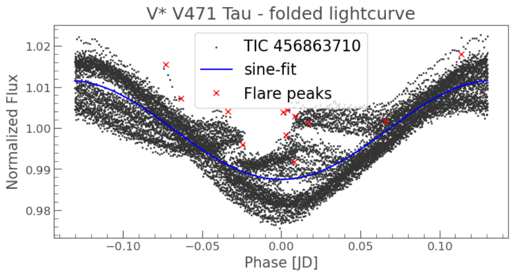

(a) TESS Sector 42

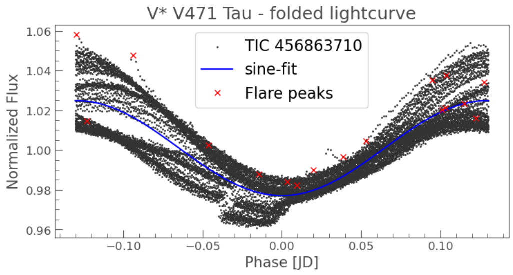

(b) TESS Sector 43

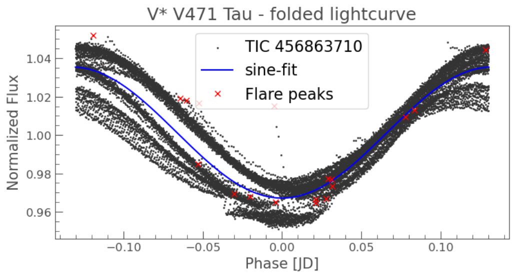

(c) TESS Sector 44

Fig. 4.24.: Folded lightcurves for V* V471 Tau. The blue lines show the calculated sine fits. The red crosses indicate the detected flare peaks.

Looking at the folded lightcurves for this star (see figures 4.24a, 4.24b and 4.24c), the transit of the white dwarf (sudden dip in the folded lightcurve) is clearly visible, and occurs happens around phase 0. Additionally lightcurves folded by the rotational period for the sectors which have a spot modulation period different from the rotational period can be seen in figure B.3 from appendix B.2.

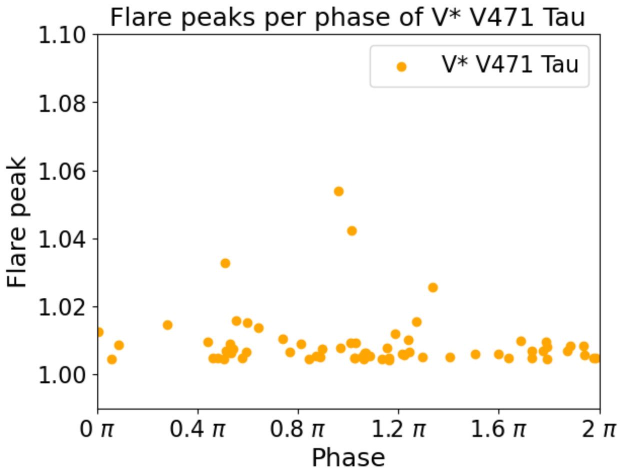

Fig. 4.25.: Distribution of flare peaks in relation to the normalized phase at which they occured. The y-axis shows the flare peak and the x-axis shows the normalized phase.

In figure 4.25 the flare peak across the normalized phase distribution can be seen. It reveals that the largest flares occured around phase 0.5π, 1π and 1.5π. The phase in which the white dwarf transit occurs is around phase 1π.

4.6.5 V* HK Aqr

HK Aqr is an M dwarf with a mass of 0.57 $M_{\odot}$, a radius of 0.53 $R_{\odot}$ and a distance of 22.3 pc. Its effective temperature is 3800 K (Gaidos et al., 2014). It was observed in four TESS sectors. For the analysis of HK Aqr the optimize fold algorithm partially broke. This happened for its lightcurves for TESS sectors 29 and 42. The algorithm found for both periodograms a second signal for a possible period. This resulted in the folded lightcurves seen in figures 4.27b and 4.28a. Figures 4.26a and 4.26b were created with this dataset.

In figure 4.26a one can see an increase in flare number at phase 1.3π. This peak is sufficiently large to be outside the error range of the lower flare count bins between phase 0 to 1π. Figure 4.26b shows a similar picture. Additionally it shows a peak at phase 0π though, which means during the phase maximum, as well as one around phase 1.6π which is in the transition from minimum to maximum.

Figures 4.29a and 4.29b show the histograms for the data of the two folded TESS lightcurves of sectors 29 and 42 which were period folded with 10 and 30 bins respectively. The folded lightcurves can be found in figure 4.30. In figure 4.29a the overall flare distribution seems to be relatively high from phase 0.2π to 1.4π, with a peak at phase 1.2π. The number of detected flares during the maximum of the

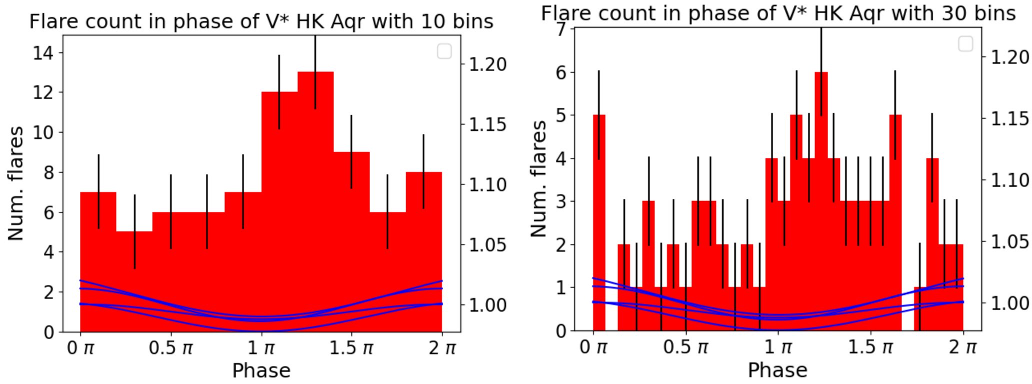

(a) 10 bins **(b)** 30 bins

Fig. 4.26.: Histograms of V* HK Aqr across the phase showing the number of flares in each bin with a total of 79 flares. The error bar shows the standard deviation for the histogram. The blue lines show the various fits for the folded lightcurves used to generate the data, with the phase minimum at 1π and phase maximum at $0\pi/2\pi$.

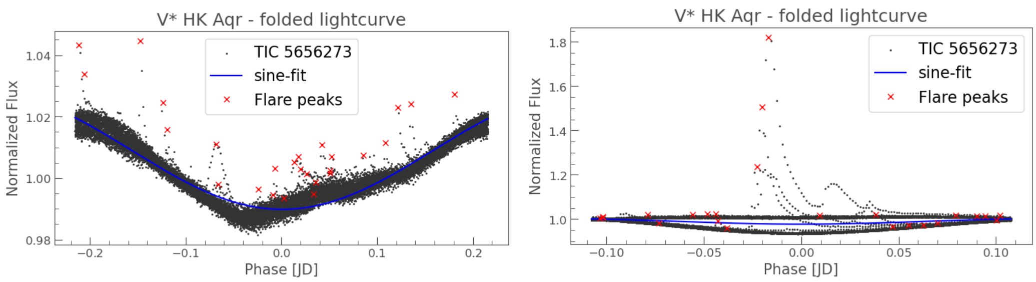

(a) TESS Sector 2 **(b)** TESS Sector 29

Fig. 4.27.: Folded lightcurves for V* HK Aqr. The blue lines shows the sine fits calculated. The red crosses indicate the detected flare peaks.

lightcurves at phase 1.8 to 0.2π is low compared to that. An additional dip of the same flare count can be seen at phase 1.5π. The flare count in figure 4.29b together with larger number of bins results in large errors. Nontheless there are two bins which stand out at phases $\sim 0.4\pi$ and $\sim 1.25\pi$ which would be in the transition from maximum to minimum, and shortly after the minimum respectively. In figure 4.27 we see that the three strongest (according to their flare peak) flares all occur at the same phase. Also here, and similar to the strong flares seen in figure 4.19, those may originate from the same spot or spot group.

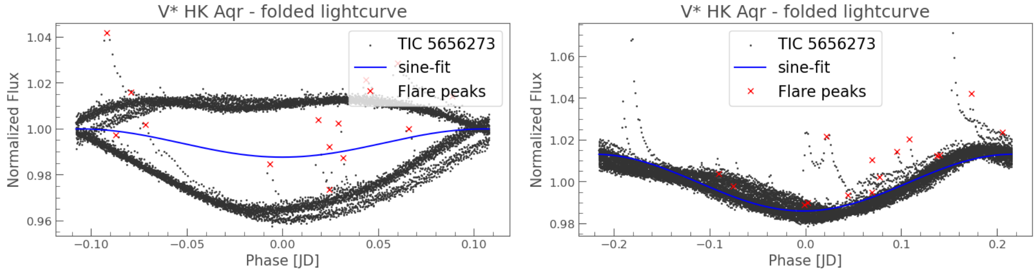

(a) TESS Sector 42 (b) TESS Sector 69

Fig. 4.28.: Folded lightcurves for V* HK Aqr. The blue lines show the calculated sine fits. The red crosses indicate the detected flare peaks.

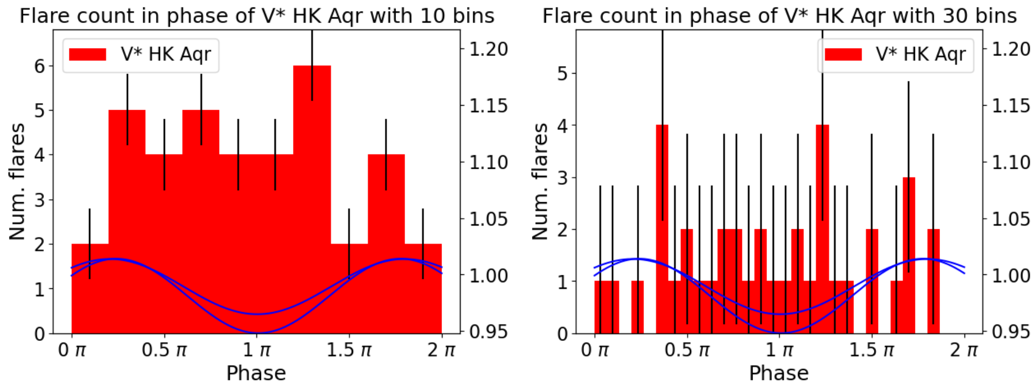

(a) 10 bins (b) 30 bins

Fig. 4.29.: Histograms of V* HK Aqr across the phase showing the number of flares in each bin with a total of 38 flares. The error bar shows the standard deviation for the histogram. The blue lines show the various fits for the folded lightcurves used to generate the data, with the phase minimum at 1π and phase maximum at $0\pi/2\pi$.

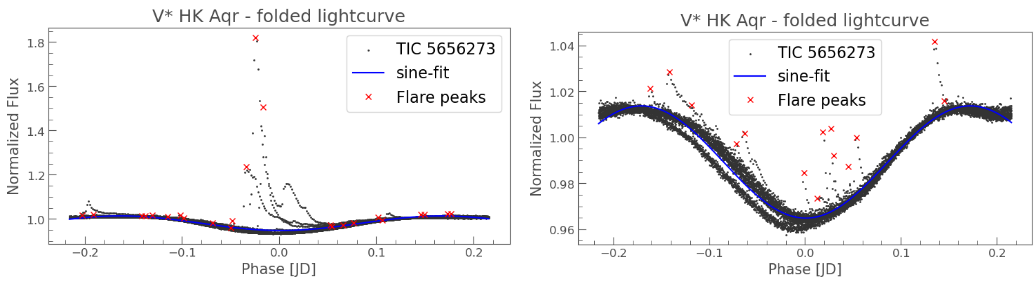

(a) TESS Sector 29 (b) TESS Sector 42

Fig. 4.30.: Folded lightcurves for V* HK Aqr. The blue lines show the calculated sine fits. The red crosses indicate the detected flare peaks.

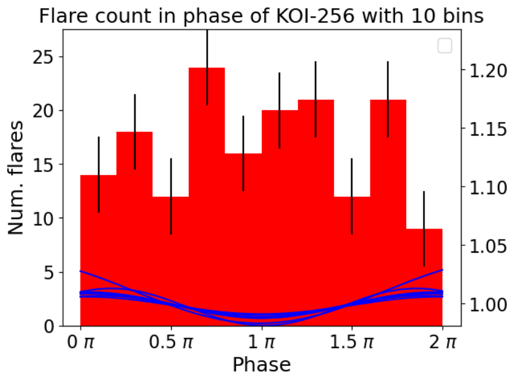

(a) 10 bins

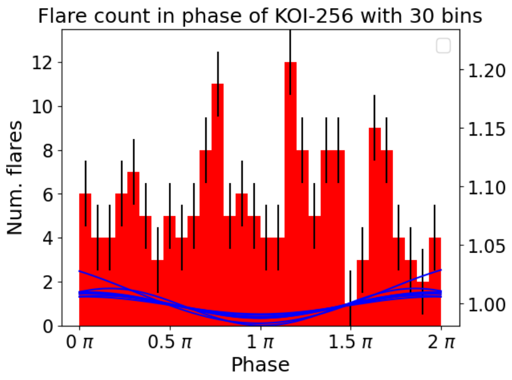

(b) 30 bins

Fig. 4.31.: Histograms of KOI-256 across the phase showing the number of flares in each bin with a total of 167 flares. The error bar shows the standard deviation for the histogram. The blue lines show the various fits for the folded lightcurves used to generate the data, with the phase minimum at 1π and phase maximum at $0\pi/2\pi$.

4.6.6 KOI-256

KOI-256 is, similarly to V471 Tau, a binary system consisting of an M dwarf and a white dwarf (Muirhead et al., 2013; Morgan, 2017). It has a mass of 0.51 $M_\odot$, a radius of 0.540 $R_\odot$ and an effective temperature of 3450 K (Muirhead et al., 2013). Similarly to HK Aqr, a second periodicity was detected, which was used to fold for spot modulation. This happened for Kepler target table ids 37, 38, 53 and TESS sector 80.

Figure 4.31a shows the histogram with 10 bins for KOI-256 with all detected spot modulations, including the mentioned ones that were wrongly detected. This figure shows an increase in flare count around phase 1π, which peaks at phases 0.7π and a bit weaker around 1.4π. Additionally there appears a peak at phase 1.7π. Increasing the bins to 30 (figure 4.31b) shows more distinct peaks at phase 0.7π as well as at 1.2π. The mentioned peaks of both figures are significantly above their surrounding bins.

Figures 4.32a and 4.32b show the histograms based on the, by the optimized fold algorithm determined, period folded lightcurves. Therefore only the period folded lightcurves from Kepler target table id 37, 38, 53 and TESS sector 80 were used. The folded lightcurves can be found in appendix B.3, figures B.4 and B.6. In figure 4.32a, which shows the histogram with 10 bins for the flare distribution across the normalized phase, there is a clear increase of flare number seen around the minimum at phase 1π. The distribution is nearly comparable to a normal distribution, except for the last two bins.

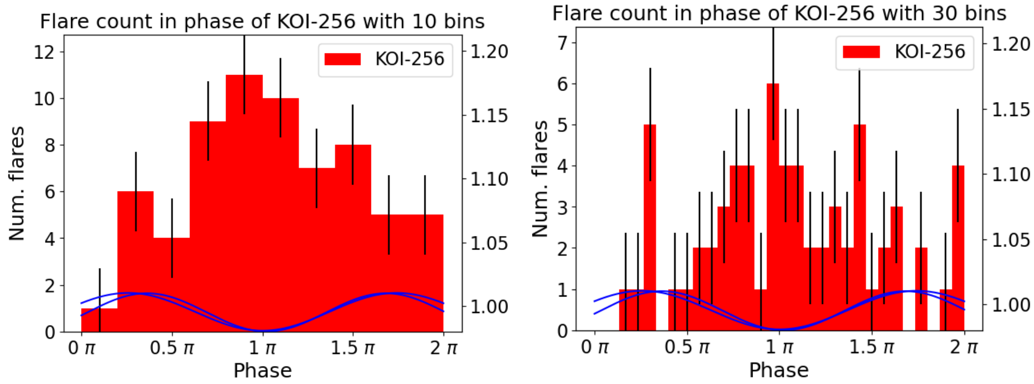

(a) 10 bins (b) 30 bins

Fig. 4.32.: Histograms of KOI-256 across the phase showing the number of flares in each bin with a total of 66 flares. The error bar shows the standard deviation for the histogram. The blue lines show the various fits for the folded lightcurves used to generate the data, with the phase minimum at 1π and phase maximum at $0\pi/2\pi$.

Looking at figure 4.32b which shows the same data, just with 30 bins, the peak at the phase minimum at 1π is still present. Additionally there are three more peaks visible around phases 0.3π, 1.4π, and 2π. These three peaks are only 1 bin wide and stand out far from their surrounding by around 1.5 times the errorbar. The peak in the center on the other hand shows gradual increases/decreases before and after, with the exception of the dip in the bin right before phase 0.9π.

Comparing the results of the flare peak distributions across the normalized phases of the two datasets in figure 4.33 shows that the highest normalized flare peaks of up to 1.7 were detected in the lightcurves with proper period detection (folded lightcurves in appendix B.3, figures B.5 and B.7). Comparing flare peaks which exist in both data samples, one can see that the highest peak of 4.33b around phase 0.8π and a normalized peak of ~1.3 was moved to phase 0.4π in figure 4.33a due to the additional detected periodicity.

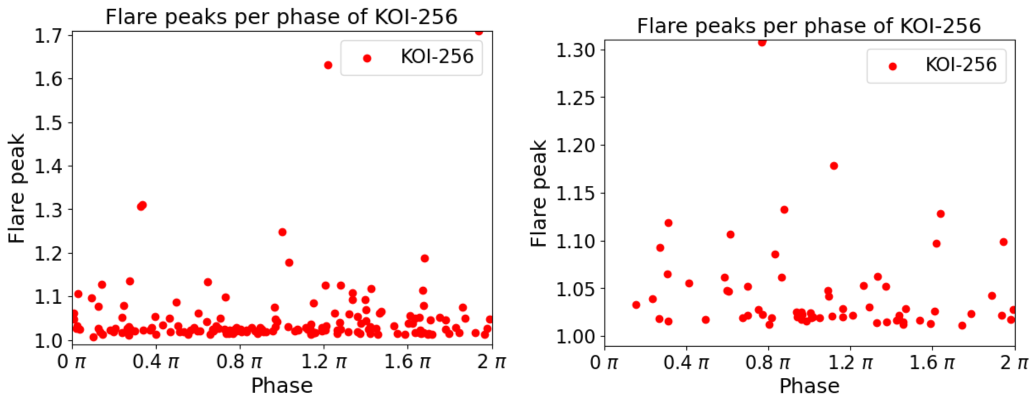

(a) Spot modulation folded

(b) Period folded

Fig. 4.33.: Distributions of flare peaks for KOI-256 in relation to the normalized phase at which they occured. Y-Axis shows the flare peak and is limited to the value of the highest peak detected. The x-axis shows the normalized phase. Panel a flare peak distribution on the normalized phase for the detected spot modulation. Panel b shows the flare distribution for the detected rotational periods.

4.6.7 2MASS J19230963+3739397

2MASS J19230963+3739397, also known as KIC 2300039 or TIC 122672447, is an M dwarf around 213 pc away from our solar system (Wenger et al., 2000). It was observed in three Kepler target table IDs as well as four TESS sectors.

The results for its flare distributions can be seen in figure 4.34. It was selected as an example as it shows the opposite of what is expected. As seen in the histogram with 10 bins (figure 4.34a) it shows an increased flare occurrence during the transition between phase minimum and maximum and during the maximum (phase 1.3π to 2π). An additional significant peak is seen in the second bin. The flare count during the phase minimum at phase 1π is lowest. Increasing the bin count to 30 (see figure 4.34b) creates a similarly shaped histogram. The errorbars are larger, and the distribution less significant. The folded lightcurves for the Kepler target table IDs 47, 48 and 49 can be seen in figure 4.35. There were no flares detected in the TESS lightcurves. As seen in the Kepler lightcurves, flare peaks as high as 1.5 have been detected, all around the phase maxima.

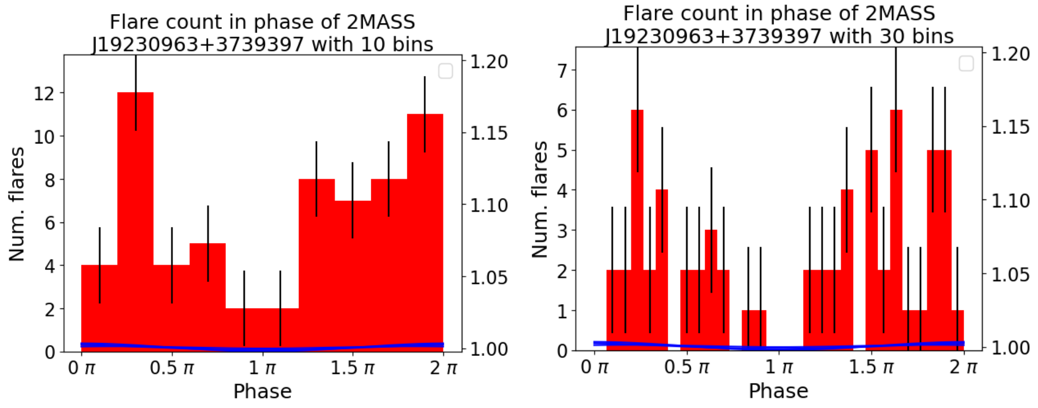

(a) 10 bins (b) 30 bins

Fig. 4.34.: Histograms of 2MASS J19230963+3739397 across the phase showing the number of flares in each bin with a total of 63 flares. The error bar shows the standard deviation for the histogram. The blue lines show the various fits for the folded lightcurves used to generate the data, with the phase minimum at 1π and phase maximum at $0\pi/2\pi$.

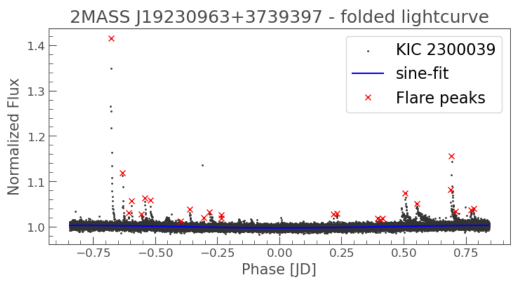

(a) Kepler target table ID 47

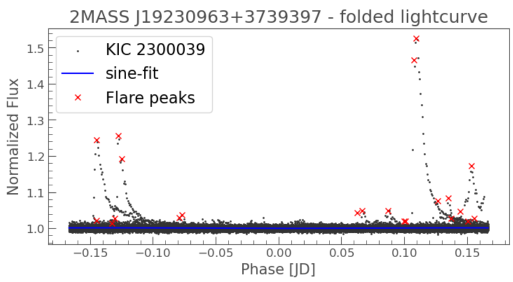

(b) Kepler target table ID 48

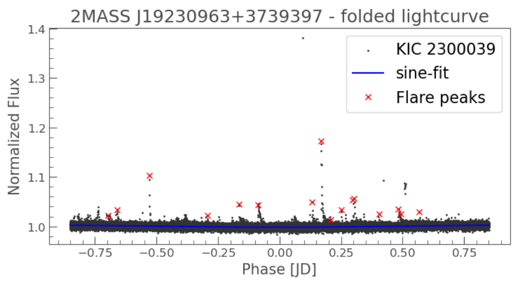

(c) Kepler target table ID 49

Fig. 4.35.: Folded lightcurves for 2MASS J19230963+3739397. The blue lines show the calculated sine fits. The red crosses indicate the detected flare peaks.

5 Discussion

The investigation of a flare to spot relation in this study is based on a large sample of known active stars, which were observed by the Kepler/K2 and TESS missions. To also catch shorter events, short-cadence data was used for Kepler/K2. Not all stars which have been analysed were used though to generate the plots in the results section (see table A.6). This list contains stars that either did not match the spectral types which were analysed in this study (e.g. some A type stars from the list of stars by Althukair and Tsiklauri (2023)), could not produce valid fits (reached 30 iterations during the fit optimization for folded lightcurves) or no consistent period was found. The full list of stars analyzed can be found in table A.1.

5.1 Analysis

The analysis was done with a self written python program (discussed in chapter 2). The reason for developing a GUI was to ease the management of the data (e.g. easily looking up parameters of a star), as well as checking individual results in a fast and easy way during the development stage. This also allowed to quickly compare the outputs of the algorithms between different "fits" files of the same star as well as between different stars. The algorithms are based on the approaches of Araújo and Valio (2021), Ilin and Poppenhaeger (2022) and Doyle et al. (2018). The thresholds described in section 3.2.1 for the flare detection algorithm have been set by trial and visual inspection of the lightcurves of multiple stars/"fits" files. The last step of the flare detection algorithm, as discussed in section 3.2.1, was implemented to prevent failures due to the flattening algorithm massively inverting dips in the lightcurves. This happened for the lightcurves of 2MASS J19033576+3941263 (TESS sectors 40, 41 and 53), 2MASS J19370439+4626209 (TESS sector 54) and V* V452 Lyr (Kepler target table ID 55). 2MASS J19033576+3941263, also known as KOI-6423 or KIC 4544623 shows regular dips in its lightcurve, which could indicate one or multiple transiting planets. It has currently been marked as a false positive candidate in the NASA Exoplanet Archive[1] (NASA Exoplanet Archive, YYYY). The TESS lightcurves for KOI-6423 can be found in appendix C in figures C.1 and C.2. While there are no noteworthy dips upon manual inspection in the lightcurve for 2MASS J19370439+4626209, flattening still generates peaks with values of over

[1] https://exoplanetarchive.ipac.caltech.edu/overview/KOI-6423

800 on a normalized lightcurve. V* V452 Lyr was observed in multiple Kepler target table IDs, with the only detected flares (4 total) in target table ID 55. The lightcurve itself is very flat (see figure C.3 in appendix C). Further to notice, the flare detection can only distinguish between high and low flare peaks, but it does not calculate the flare energy. But we can say that all flares detected on G type stars in broad-band photometry such as Kepler/K2 and TESS are superflares, as the lowest detectable flare peak by this algorithm is 1.003, and Maehara et al. (2012), using Kepler data, found that an increase of 0.1% in flux (flare peak of 1.001) is enough for those flares to be categorized as superflares.

While the folding algorithm (see section 3.2.2) works on most stars/"fits" files, it has its limitations in edge cases like V* HK Aqr or KOI-256 as described in sections 4.6.5 and 4.6.6. It is set to check for an additional periodicity signal if the fit for the folded lightcurve has two peaks which are further away than 10% of the total phase from the edge. While it is expected to find two peaks when folding and fitting a sine function due to marging of error of the fitting parameters, there has to be set a limit for when to search for additional periodicity. A well working (and near perfect) example is V471 Tau. It shows additional periodicity in the TESS lightcurves 42, 32 and 44 (see figure B.3 in appendix B), but not in 70 and 71. Additionally the shift by the difference of the fit minimum to the (currently used) epoch for the fold is necessary to generate reliable results, as otherwise it has been found that the minimum of the fit/folded lightcurve can vary by up to ~25% depending on which first minimum is detected in the lightcurve.

5.2 Flares and superflares on M-F stars and their spot dependence

Out of a total of ~160 M dwarfs in the list of stars to be analyzed, flares could only be detected on 49 stars. This could be due to the algorithm or instruments being possibly not sufficiently sensitive, too noisy data or it could be that there were simply no flares during the observations. For the remaining 49 stars, a total of ~3500 flares was detected. Using all available flares, there was no significant spot dependency detected in the histogram with 10 bins. In the third bin at phase 0.5π there were ~50 flares less detected compared to other bins. This bin is located in the transition from the phase maxima to minima. While not being significant, the 6th bin around phase 1.1π has the most flares detected, and is located at the phase minimum. This could show a possible dependency with more available data, similarly to what was found for K type dwarfs. The data also contain the detected flares from KOI-256 and V* HK Aqr, which were not folded correctly. Manually comparing the results for V* HK Aqr (figures 4.26a and 4.29a), the folded lightcurves show that for TESS sector

29 the detected minimum ($\pm$ a quarter of the phase) the amount of detected flares flipped. While more flares should be counted in the minimum (see figure 4.30a) compared to the maximum (see figure 4.27b), the opposite is the case. Similarly for TESS sector 42. Overall these changes make the spot dependence of flares on V* HK Aqr more clear, as the histogram (10 bins) with only the rotational period folded lightcurves indicates a spot dependency. There are significantly more flares counted around the minimum compared to the phase maximum. The flares with the highest peaks on V* HK Aqr were also detected during the phase minimum in TESS sector 29 with a normalized peak of up to 1.8. KOI-256 shows a similar behaviour, revealing a clear spot dependence when using only period folded lightcurves for the histogram, while having more spread out peaks around the phase minimum when using all spot modulation folded lightcurves.

2MASS J19230963+3739397 on the other hand is a star, which shows an inverted spot dependency. This could be an indication that similarly to what Araújo and Valio (2023) found, the spot area is not the only important parameter.

Limiting the flare by maximum flare peak indicates a dependency of flares on spots, which can be seen in figures 4.2a to 4.5a. While no flare energies were calculated in this study, this could be parameters to look at in the future. Limiting the flare peaks to a maximum of 1.01 shows a higher count in the phase maxima compared to the phase minima. The same dip as with all flares can be seen here already too. Increasing the flare peak limit to 1.05 shows a nearly identical histogram to the one with all flares. A noteworthy difference here is the peak in the bin at the phase minimum at 1π. Roettenbacher and Vida (2018) found an increase of flares in M and K dwarfs at phase minimum with flares which had a flux increase at their peaks between 1% and 5%. The differences could be due to a different set of stars and flare detection methods.

Out of a total of ~40 K dwarfs in the list of stars to be analyzed, flares could only be detected on 21 stars. This could be due to the algorithm or instruments being possibly not sufficiently sensitive, too noisy data or it could be that there were simply no flares during the observations. Overall the results for the flare distribution of K dwarfs is similar to those of M dwarfs, with the exception of the bin (bins for the histogram with 30 bins) around the phase minimum. This bin shows a significantly increased flare count. One of the causes for this, but not the sole one, is V* V471 Tau (see section 4.6.4), which is in close orbit with a white dwarf (Muirhead et al., 2022; Kővári et al., 2021). This can lead to magnetic interactions between the K dwarf and the white dwarf (Kővári et al., 2021), which may lead to the increased flare count seen.

Limiting the flare peaks to greater than 1.05 shows two peaks around the center bin, with one higher bin being at the maximum at phase 0π. While the two peaks around the phase minimum could indicate a dependency on spots, it is not the only relevant bin found. Limiting the flare peaks to a maximum of 1.01 shows an interesting pattern. There is a larger count of flares found during the phase minimum, but also during the phase maximum, while less flares have been detected in the transition between phase miminum/maximum. Increasing the allowed flare peak to 1.05 shows a similar pattern, but the gaps between peaks/dips vanishes and the histogram becomes already very similar to the histogram with all flares.

Out of a total of ~80 G dwarfs in the list of stars to be analyzed, flares could only be detected on 21 stars. This could be due to the algorithm or instruments being possibly not sufficiently sensitive, too noisy data or it could be that there were simply no flares during the observations. Most of the flares detected show a peak of below 1.05, but as Maehara et al. (2012) found, flares with a flux increase between 0.1 to 1% (peaks of 1.001 to 1.01) would already be categorized as superflares for G-star flares detected in broad-band photometry such as Kepler/K2 and TESS. Therefore all flares detected for G stars shown in figure 4.10 are superflares as the threshold of the flare detection algorithm is 0.3%. For the flares found in this study for G type stars, there is a spot dependency, as the flare count peaks around the phase minimum. Unlike the other results, there is a gradual fall off to each sides till the phase maximum is reached. As no energies have been deduced from the Kepler/K2 and TESS observations a categorization in flares and superflares is difficult for all stars investigated in the present study.

Limiting the flare peaks to a minimum of 1.05 shows three major peaks. The largest being at the phase minimum, while the other two are in the transition between maximum and miminum and minimum and maximum. This does not indicate a pure spot dependency, and a more detailed look at the individual events is necessary.

BD-08 995, which is according to its B-V color index and effective temperature a late G type star, reflects this trend well. It shows the same bell curve style histogram as the overall flare number histogram of G-stars. Additionally though it also shows a slight increase in flare number around the phase maximum, its highest flare peak was detected around the phase maximum (see figure 4.16). The maximum flare count for TYC 4595-107-1 on the other hand is slightly offset before the phase minimum (see figure 4.21a). It also shows a slight increase of flares around the maximum. Its highest flare peak was detected in the same bin as the highest flare count (see figure 4.22).

Out of a total of ∼13 F dwarfs in the list of stars to be analyzed, flares could only be detected on four stars. This could be due to the algorithm or instruments being possibly not sufficiently sensitive, too noisy data or it could be that there were simply no flares during the observations. While all flares detected are centered around the phase minimum, the total of 5 flares detected is not a sufficiently large sample to draw a definite conclusion on the spot to flare/superflare relation.

For two stars, namely the K-dwarf TYC 1360-957-1 and the M-dwarf HK Aqr we find that the most energetic flares occur at the same phase. For TYC 1360-957-1 (see figure 4.19) the flares with largest flare peak originate all from phase 0.7 to 0.8π. Two flares were detected in TESS sector 44 and one two sectors later (sector 46). From the Sun we know that spots can have lifetimes of several rotation periods i.e. several months. This maybe also the case for the spot or spot group being the origin of the three strong flares on TYC 1360-957-1.

A similar finding was made on HK Aqr. Also the three strongest flares have been found to occur at the same phase. For HK Aqr this happened in one TESS sector (sector 29, see figure 4.30a). Also here it is reasonable to assume that these three flares have been generated by the same spot or spot group. For both stars the phases at which these strong flares have occurred are close to the phase minimum, i.e. correspond to hemispheres of the stars showing a huge spottedness.

Looking at all results together, there is a trend that more flares occur when a more spotted stellar hemisphere is visible, than vice versa. This is mostly influenced by the results for K and G stars. The dip in the otherwise seemingly flat histogram for the results of M dwarfs dominates the overall results. There is at the moment no explanation for the significant dip in the histogram and we doubt that it has a physical meaning.

All results will be published on github. The program will be available at `https://gitlab.com/SGCMarkus/flaredetector` while the data will be available at `https://gitlab.com/SGCMarkus/flaredetector_results`. The different branches define which fitting function was used for the data, e.g. the results containing all plots which used a sine function to fit, are found in the "sine" branch on Github.

6 Conclusion and Outlook

In conclusion the only cumulative results which shows a significant spot dependence are those for G type stars. This distribution shows a significant increase in flares during the phase minimum over the overall flare distribution. The distribution shows a strong similarity to a normal distribution. The same accounts for the two selected G type stars BD-08 995 and TYC 4595-107-1 which were presented and discussed individually. The histograms for K dwarfs on the other hand do not reveal similarities to a normal distribution. There appears a singular peak in the histogram with 10 bins at the phase minimum, with a few additional narrower peaks in the histogram with 30 bins. This could indicate a dependence of some sort, but a more detailed view at the individual stars is needed. As this category includes V* V471 Tau (close binary system with a white dwarf), similar interactions could happen on other stars. While there is no significant result for a spot dependence of the detected flares on M dwarfs, some individual stars show a behaviour similar to G-stars. HK Aqr and KOI-256 are here good examples, whereas 2MASS J19230963+3739397 shows few flares in the minimum but more flares in the maximum of the phasefolded lightcurve.

Overall improvements to the folding algorithms are required to handle edge cases better (e.g. KOI-256) , while not breaking for others. This could either be done automatically, or by setting special parameters for individual stars. Even though the latter would require manual user interaction and checking the edge cases manually. Additionally a common folding epoch for multiple "fits "files of the same star could be implemented. A good example would be V471 Tau, which showed a consistent spot modulation in some of its TESS lightcurves which differed from its rotational period. Implementing something like this could guarantee that the (in this case) transit of the white dwarf would always be at the same position in the phase, and not "jumping" between the center and the edges. Furthermore the energy for the flares could be calculated. To achieve this, improvement of the flare duration algorithm is required though, as it currently makes just an estimation of the flare duration and does not account for the longest flare durations. It neither makes a distinction between TESS lightcurves with a 2 minute cadence and the Kepler/K2 short cadence data which has a cadence of 1 minute.

Furthermore more stars could be taken into consideration. While the Kepler/K2 missions are complete, the TESS mission is being extended and still observing as of writing this thesis. One could also take into account Kepler long cadence data (30 minute cadence), which would not be able to detect shorter duration flares, but being available for a larger amount of stars.

Bibliography

Allen, Jesse S. (2025). *The Classification of Stellar Spectra* (cit. on pp. 3, 4).

Althukair, A. K. and D. Tsiklauri (Aug. 2023). „Main Sequence Star Super-flare Frequency based on Entire Kepler Data". In: *Research in Astronomy and Astrophysics* 23.8, 085017, p. 085017. DOI: 10.1088/1674-4527/acdc09. arXiv: 2212.10224 [astro-ph.SR] (cit. on pp. 25, 59).

Araújo, Alexandre and Adriana Valio (Dec. 2021). „Kepler-411 Star Activity: Connection between Starspots and Superflares". In: *The Astrophysical Journal Letters* 922.2, L23, p. L23. DOI: 10.3847/2041-8213/ac3767. arXiv: 2111.05452 [astro-ph.SR] (cit. on pp. 2, 25, 26, 59).

– (June 2023). „The connection between starspots and superflares: a case study of two stars". In: *Monthly Notices of the RAS* 522.1, pp. L16–L20. DOI: 10.1093/mnrasl/slad034. arXiv: 2303.16051 [astro-ph.SR] (cit. on pp. 2, 25, 61).

Aschwanden, Markus J. and Samuel L. Freeland (Aug. 2012). „Automated Solar Flare Statistics in Soft X-Rays over 37 Years of GOES Observations: The Invariance of Self-organized Criticality during Three Solar Cycles". In: *The Astrophysical Journal* 754.2, 112, p. 112. DOI: 10.1088/0004-637X/754/2/112. arXiv: 1205.6712 [astro-ph.SR] (cit. on p. 1).

Astropy Collaboration, A. M. Price-Whelan, B. M. SipHocz, et al. (Sept. 2018). „The Astropy Project: Building an Open-science Project and Status of the v2.0 Core Package". In: *aj* 156.3, 123, p. 123. DOI: 10.3847/1538-3881/aabc4f. arXiv: 1801.02634 [astro-ph.IM] (cit. on pp. vii, 25).

Astropy Collaboration, T. P. Robitaille, E. J. Tollerud, et al. (Oct. 2013). „Astropy: A community Python package for astronomy". In: *Astronomy and Astrophysics* 558, A33, A33. DOI: 10.1051/0004-6361/201322068. arXiv: 1307.6212 [astro-ph.IM] (cit. on p. vii).

Australian Space Weather Forecasting Centre (2025). *The Magnetic Fields around Sunspots* (cit. on p. 5).

Berlind, Perry (2025). *A note on the spectral atlas and spectral classification* (cit. on pp. 3, 4, 28, 30).

Borucki, William J., David Koch, Gibor Basri, et al. (Feb. 2010). „Kepler Planet-Detection Mission: Introduction and First Results". In: *Science* 327.5968, p. 977. DOI: 10.1126/science.1185402 (cit. on pp. 1, 7, 8).

Cannon, Annie Jump and Edward Charles Pickering (Jan. 1912a). „Classification of 1,477 stars by means of their photographic spectra“. In: *Annals of Harvard College Observatory* 56.4, pp. 65–114 (cit. on p. 3).

– (Jan. 1912b). „Classification of 1,688 southern stars by means of their spectra“. In: *Annals of Harvard College Observatory* 56.5, pp. 115–164 (cit. on p. 3).

Carrington, R. C. (Nov. 1859). „Description of a Singular Appearance seen in the Sun on September 1, 1859“. In: *Monthly Notices of the RAS* 20, pp. 13–15. DOI: 10.1093/mnras/20.1.13 (cit. on pp. 1, 6).

Crowley, James, Michael S. Wheatland, and Kai Yang (Dec. 2022). „Observed Rate Variations in Superflaring G-type Stars“. In: *The Astrophysical Journal* 941.2, 193, p. 193. DOI: 10.3847/1538-4357/aca476. arXiv: 2212.00993 [astro-ph.SR] (cit. on p. 48).

Cuntz, Manfred, Steven H. Saar, and Zdzislaw E. Musielak (Apr. 2000). „On Stellar Activity Enhancement Due to Interactions with Extrasolar Giant Planets“. In: *The Astrophysical Journal Letters* 533.2, pp. L151–L154. DOI: 10.1086/312609 (cit. on p. 1).

Doyle, L., G. Ramsay, J. G. Doyle, and K. Wu (Oct. 2019). „Probing the origin of stellar flares on M dwarfs using TESS data sectors 1-3“. In: *Monthly Notices of the RAS* 489.1, pp. 437–445. DOI: 10.1093/mnras/stz2205. arXiv: 1908.02698 [astro-ph.SR] (cit. on pp. 2, 8, 9, 25).

Doyle, L., G. Ramsay, J. G. Doyle, K. Wu, and E. Scullion (Oct. 2018). „Investigating the rotational phase of stellar flares on M dwarfs using K2 short cadence data“. In: *Monthly Notices of the RAS* 480.2, pp. 2153–2164. DOI: 10.1093/mnras/sty1963. arXiv: 1807.08592 [astro-ph.SR] (cit. on pp. 2, 25, 27, 59).

Fox, Karen (2025). *The Dynamic Solar Magnetic Field with Introduction* (cit. on p. 4).

Gaidos, E., A. W. Mann, S. Lépine, et al. (Sept. 2014). „Trumpeting M dwarfs with CONCH-SHELL: a catalogue of nearby cool host-stars for habitable exoplanets and life“. In: *Monthly Notices of the RAS* 443.3, pp. 2561–2578. DOI: 10.1093/mnras/stu1313. arXiv: 1406.7353 [astro-ph.SR] (cit. on p. 51).

Gilliland, Ronald L., William J. Chaplin, Edward W. Dunham, et al. (Oct. 2011). „KEPLER MISSION STELLAR AND INSTRUMENT NOISE PROPERTIES“. In: *The Astrophysical Journal Supplement Series* 197.1, p. 6. DOI: 10.1088/0067-0049/197/1/6 (cit. on p. 8).

Ginsburg, A., B. M. Sipőcz, C. E. Brasseur, et al. (Mar. 2019). „astroquery: An Astronomical Web-querying Package in Python“. In: *The Astronomical Journal* 157, 98, p. 98. DOI: 10.3847/1538-3881/aafc33. arXiv: 1901.04520 [astro-ph.IM] (cit. on pp. vii, 11, 25).

Gopika, V. S., V. Blessy, V. A. Asha, et al. (Aug. 2025). „Investigating the impact of solar flares on the geomagnetic field at Resolute Bay in 2012: A comparative statistical analysis“. In: *Journal of Atmospheric and Solar-Terrestrial Physics* 273, 106544, p. 106544. DOI: 10.1016/j.jastp.2025.106544 (cit. on p. 1).

Harris, Charles R., K. Jarrod Millman, Stéfan J. van der Walt, et al. (Sept. 2020). „Array programming with NumPy“. In: *Nature* 585.7825, pp. 357–362. DOI: 10.1038/s41586-020-2649-2 (cit. on pp. vii, 25).

Hayakawa, Hisashi, Sabrina Bechet, Frédéric Clette, et al. (Sept. 2023). „Magnitude Estimates for the Carrington Flare in 1859 September: As Seen from the Original Records“. In: *The Astrophysical Journal Letters* 954.1, L3, p. L3. DOI: 10.3847/2041-8213/acd853 (cit. on p. 6).

Hodgson, R. (Nov. 1859). „On a curious Appearance seen in the Sun“. In: *Monthly Notices of the RAS* 20, pp. 15–16. DOI: 10.1093/mnras/20.1.15a (cit. on p. 6).

Howard, Ward S. and Nicholas M. Law (Oct. 2021). „EvryFlare. IV. Detection of Periodicity in Flare Occurrence from Cool Stars with TESS“. In: *The Astrophysical Journal* 920.1, 42, p. 42. DOI: 10.3847/1538-4357/ac142a. arXiv: 2107.06293 [astro-ph.SR] (cit. on pp. 1, 2, 25).

Hunter, J. D. (2007). „Matplotlib: A 2D Graphics Environment“. In: *Computing in Science Engineering* 9.3, pp. 90–95 (cit. on p. vii).

Ilin, E. and K. Poppenhaeger (July 2022). „Searching for flaring star-planet interactions in AU Mic TESS observations“. In: *Monthly Notices of the RAS* 513.3, pp. 4579–4586. DOI: 10.1093/mnras/stac1232. arXiv: 2204.14090 [astro-ph.SR] (cit. on pp. 1, 2, 25–27, 59).

Ip, Wing-Huen, Andreas Kopp, and Juei-Hwa Hu (Feb. 2004). „On the Star-Magnetosphere Interaction of Close-in Exoplanets“. In: *The Astrophysical Journal* 602.1, p. L53. DOI: 10.1086/382274 (cit. on p. 1).

Joy, A. H. and M. L. Humason (June 1949). „Observations of the Faint Dwarf Star L 726-8“. In: *Publications of the Astronomical Society of the Pacific* 61.360, pp. 133–134. DOI: 10.1086/126150 (cit. on p. 1).

Kővári, Zs., L. Kriskovics, K. Oláh, et al. (June 2021). „A confined dynamo: Magnetic activity of the K-dwarf component in the pre-cataclysmic binary system V471 Tauri“. In: *Astronomy and Astrophysics* 650, A158, A158. DOI: 10.1051/0004-6361/202140707. arXiv: 2103.02041 [astro-ph.SR] (cit. on pp. 49, 61).

Lightkurve Collaboration, J. V. d. M. Cardoso, C. Hedges, et al. (Dec. 2018). *Lightkurve: Kepler and TESS time series analysis in Python*. Astrophysics Source Code Library. ascl: 1812.013 (cit. on pp. 11, 12, 15, 17, 25).

Luyten, W. J. (Aug. 1949). „A THIRD FLARE OF L 726-8B“. In: *Publications of the Astronomical Society of the Pacific* 61.361, p. 179. DOI: 10.1086/126169 (cit. on p. 1).

Lysenko, Alexandra, Dmitry Frederiks, Gregory Fleishman, et al. (June 2019). „X-ray and gamma-ray emission of solar flares“. In: *Physics-Uspekhi* 63. DOI: 10.3367/UFNe.2019.06.038757 (cit. on p. 7).

Maehara, Hiroyuki (Oct. 2017). „Starspot Activity and Superflares on Solar-type Stars“. In: *Living Around Active Stars*. Ed. by D. Nandy, A. Valio, and P. Petit. Vol. 328. IAU Symposium, pp. 22–29. DOI: 10.1017/S1743921317003945 (cit. on p. 1).

Maehara, Hiroyuki, Yuta Notsu, Shota Notsu, et al. (July 2018). „Starspots on late-type stars and their correlation with flare activity“. In: *20th Cambridge Workshop on Cool Stars, Stellar Systems and the Sun*. Cambridge Workshop on Cool Stars, Stellar Systems, and the Sun, 69, p. 69. DOI: 10.5281/zenodo.1487829 (cit. on p. 1).

Maehara, Hiroyuki, Takuya Shibayama, Shota Notsu, et al. (May 2012). „Superflares on solar-type stars“. In: *Nature* 485.7399, pp. 478–481. DOI: 10.1038/nature11063 (cit. on pp. 60, 62).

Maehara, Hiroyuki, Takuya Shibayama, Yuta Notsu, et al. (Dec. 2015). „Statistical properties of superflares on solar-type stars based on 1-min cadence data“. In: *Earth, Planets and Space* 67, 59, p. 59. DOI: 10.1186/s40623-015-0217-z. arXiv: 1504.00074 [astro-ph.SR] (cit. on p. 1).

McKinney, Wes (2010). „Data Structures for Statistical Computing in Python“. In: *Proceedings of the 9th Python in Science Conference*. Ed. by Stéfan van der Walt and Jarrod Millman, pp. 56–61. DOI: 10.25080/Majora-92bf1922-00a (cit. on p. vii).

McLean, M., E. Berger, and A. Reiners (Feb. 2012). „The Radio Activity-Rotation Relation of Ultracool Dwarfs“. In: *The Astrophysical Journal* 746.1, 23, p. 23. DOI: 10.1088/0004-637X/746/1/23. arXiv: 1108.0415 [astro-ph.SR] (cit. on p. 2).

Mikulski Archive for Space Telescopes (2025). *K2* (cit. on p. 8).

Mohanty, Subhanjoy and Gibor Basri (Jan. 2003). „Rotation and Activity in Mid-M to L Field Dwarfs“. In: *The Astrophysical Journal* 583.1, pp. 451–472. DOI: 10.1086/345097. arXiv: astro-ph/0201455 [astro-ph] (cit. on p. 2).

Morgan, D. P. (Jan. 2017). „The effects of close binaries on the magnetic activity of M dwarfs as probed using close white dwarf companions“. PhD thesis. Boston University, Massachusetts (cit. on p. 54).

Muirhead, Philip S., Jason Nordhaus, and Maria R. Drout (Jan. 2022). „Revised Stellar Parameters for V471 Tau, A Post-common Envelope Binary in the Hyades“. In: *The Astronomical Journal* 163.1, 34, p. 34. DOI: 10.3847/1538-3881/ac390f. arXiv: 2111.06905 [astro-ph.SR] (cit. on pp. 49, 61).

Muirhead, Philip S., Andrew Vanderburg, Avi Shporer, et al. (Apr. 2013). „Characterizing the Cool KOIs. V. KOI-256: A Mutually Eclipsing Post-common Envelope Binary“. In: *The Astrophysical Journal* 767.2, 111, p. 111. DOI: 10.1088/0004-637X/767/2/111. arXiv: 1304.1165 [astro-ph.SR] (cit. on p. 54).

NASA Exoplanet Archive (YYYY). *Kepler Objects of Interest DR25*. Version Version: YYYY-MM-DD HH:MM. DOI: 10.26133/NEA5 (cit. on p. 59).

Norton, Aimee (2025). *Unravelling magnetic knots in sunspots* (cit. on p. 6).

Notsu, Yuta, Takuya Shibayama, Hiroyuki Maehara, et al. (July 2013). „Superflares on Solar-type Stars Observed with Kepler II. Photometric Variability of Superflare-generating Stars: A Signature of Stellar Rotation and Starspots“. In: *The Astrophysical Journal* 771.2, 127, p. 127. DOI: 10.1088/0004-637X/771/2/127. arXiv: 1304.7361 [astro-ph.SR] (cit. on p. 1).

Ochsenbein F. et. al (n.d.). *The VizieR database of astronomical catalogues*. DOI: 10.26093/cds/vizier (cit. on p. 28).

Payne-Gaposchkin, Cecilia Helena (Jan. 1925). „Stellar atmospheres: A contribution to the observational study of high temperature in the reversing layers of stars“. PhD thesis. Radcliffe College, United States (cit. on p. 3).

Priest, Eric and T.G. Forbes (Jan. 2002). „The magnetic nature of solar flares“. In: *Astronomy and Astrophysics Review* 10, pp. 313–377. DOI: 10.1007/s001590100013 (cit. on p. 6).

Priest, Eric and Terry Forbes (2000). *Magnetic Reconnection: MHD Theory and Applications*. DOI: 10.1017/CBO9780511525087 (cit. on p. 6).

Reep, Jeffrey W. and Will T. Barnes (Oct. 2021). „Forecasting the Remaining Duration of an Ongoing Solar Flare“. In: *Space Weather* 19.10, e02754, e02754. DOI: 10.1029/2021SW002754. arXiv: 2103.03957 [astro-ph.SR] (cit. on p. 6).

Reep, Jeffrey W. and Kalman J. Knizhnik (Apr. 2019). „What Determines the X-Ray Intensity and Duration of a Solar Flare?“ In: *The Astrophysical Journal* 874.2, 157, p. 157. DOI: 10.3847/1538-4357/ab0ae7. arXiv: 1903.10564 [astro-ph.SR] (cit. on p. 25).

Reid, Neill (2025). *Intrinsic colours as a function of spectral type* (cit. on pp. 28, 30).

Ricker, George R., Joshua N. Winn, Roland Vanderspek, et al. (2014a). „Transiting Exoplanet Survey Satellite“. In: *Journal of Astronomical Telescopes, Instruments, and Systems* 1.1, p. 014003. DOI: 10.1117/1.JATIS.1.1.014003 (cit. on p. 9).

Ricker, George R., Joshua N. Winn, Roland Vanderspek, et al. (Aug. 2014b). „Transiting Exoplanet Survey Satellite (TESS)“. In: *Space Telescopes and Instrumentation 2014: Optical, Infrared, and Millimeter Wave*. Ed. by Jacobus M. Oschmann Jr., Mark Clampin, Giovanni G. Fazio, and Howard A. MacEwen. Vol. 9143. Society of Photo-Optical Instrumentation Engineers (SPIE) Conference Series, 914320, p. 914320. DOI: 10.1117/12.2063489. arXiv: 1406.0151 [astro-ph.EP] (cit. on p. 1).

Riverbank Computing Limited (2025). *PyQt5* (cit. on pp. 11, 13, 15).

Roettenbacher, Rachael M. and Krisztián Vida (Nov. 2018). „The Connection between Starspots and Flares on Main-sequence Kepler Stars“. In: *The Astrophysical Journal* 868.1, 3, p. 3. DOI: 10.3847/1538-4357/aae77e. arXiv: 1810.04762 [astro-ph.SR] (cit. on pp. 1, 2, 61).

Rowe, Jason F., Jaymie M. Matthews, Sara Seager, et al. (Feb. 2009). „Towards the Albedo of an Exoplanet: MOST Satellite Observations of Bright Transiting Exoplanetary Systems“. In: *Transiting Planets*. Ed. by Frédéric Pont, Dimitar Sasselov, and Matthew J. Holman. Vol. 253. IAU Symposium, pp. 121–127. DOI: 10.1017/S1743921308026318. arXiv: 0807.1928 [astro-ph] (cit. on p. 8).

Shibata, Kazunari, Hiroaki Isobe, Andrew Hillier, et al. (June 2013). „Can Superflares Occur on Our Sun?“ In: *Publications of the Astronomical Society of Japan* 65.3, 49, p. 49. DOI: 10.1093/pasj/65.3.49. arXiv: 1212.1361 [astro-ph.SR] (cit. on p. 1).

Shibata, Kazunari and Tetsuya Magara (Dec. 2011). „Solar Flares: Magnetohydrodynamic Processes“. In: *Living Reviews in Solar Physics* 8.1, 6, p. 6. DOI: 10.12942/lrsp-2011-6 (cit. on pp. 1, 6).

Solanki, Sami K. (Jan. 2003). „Sunspots: An overview“. In: *The Astronomy and Astrophysics Review* 11.2-3, pp. 153–286. DOI: 10.1007/s00159-003-0018-4 (cit. on p. 4).

SQLite Development Team (2025). *SQLite* (cit. on pp. 11, 12).

Stassun, Keivan G., Ryan J. Oelkers, Martin Paegert, et al. (Oct. 2019). „The Revised TESS Input Catalog and Candidate Target List“. In: *The Astronomical Journal* 158.4, 138, p. 138. DOI: 10.3847/1538-3881/ab3467. arXiv: 1905.10694 [astro-ph.SR] (cit. on pp. 28, 44).

The pandas development team (Feb. 2020). *pandas-dev/pandas: Pandas*. Version latest. DOI: 10.5281/zenodo.3509134 (cit. on pp. vii, 22, 25).

The SOHO Team (2025). *SOHO* (cit. on p. 5).

Thompson, Susan E., Dorothy Fraquelli, Jeffrey E. Van Cleve, and Douglas A. Caldwell (May 2016). „Kepler Archive Manual“. In: (cit. on p. 12).

Tu, Zuo-Lin, Ming Yang, H. -F. Wang, and F. Y. Wang (Apr. 2021). „Superflares, Chromospheric Activities, and Photometric Variabilities of Solar-type Stars from the Second-year Observation of TESS and Spectra of LAMOST“. In: *The Astrophysical Journal Supplement* 253.2, 35, p. 35. DOI: 10.3847/1538-4365/abda3c. arXiv: 2101.02901 [astro-ph.SR] (cit. on p. 48).

Tu, Zuo-Lin, Ming Yang, Z. J. Zhang, and F. Y. Wang (Feb. 2020). „Superflares on Solar-type Stars from the First Year Observation of TESS“. In: *The Astrophysical Journal* 890.1, 46, p. 46. DOI: 10.3847/1538-4357/ab6606. arXiv: 1912.11572 [astro-ph.SR] (cit. on p. 44).

Twicken, Joseph D., Douglas A. Caldwell, Jon M. Jenkins, et al. (Sept. 2020). „TESS Science Data Products Description Document“. In: (cit. on p. 12).

Van Rossum, Guido and Fred L. Drake (2009). *Python 3 Reference Manual*. Scotts Valley, CA: CreateSpace (cit. on pp. 11, 25).

Vasilyev, Valeriy, Timo Reinhold, Alexander I. Shapiro, et al. (Dec. 2024). „Sun-like stars produce superflares roughly once per century“. In: *Science* 386.6727, pp. 1301–1305. DOI: 10.1126/science.adl5441. arXiv: 2412.12265 [astro-ph.SR] (cit. on p. 1).

Virtanen, Pauli, Ralf Gommers, Travis E. Oliphant, et al. (2020). „SciPy 1.0: Fundamental Algorithms for Scientific Computing in Python“. In: *Nature Methods* 17, pp. 261–272. DOI: 10.1038/s41592-019-0686-2 (cit. on pp. vii, 25).

Wenger, M., F. Ochsenbein, D. Egret, et al. (Apr. 2000). „The SIMBAD astronomical database. The CDS reference database for astronomical objects“. In: *Astronomy and Astrophysics Supplement Series* 143, pp. 9–22. DOI: 10.1051/aas:2000332. arXiv: astro-ph/0002110 [astro-ph] (cit. on pp. 11, 44, 46, 56).

Zhang, Jie, Xin Cheng, and Ming-De Ding (Mar. 2012). „Observation of an evolving magnetic flux rope before and during a solar eruption“. In: *Nature Communications* 3, 747, p. 747. DOI: 10.1038/ncomms1753. arXiv: 1203.4859 [astro-ph.SR] (cit. on p. 1).

A List of stars

Table A.1.: Table containing all stars which where analysed. The first column (Main Identifier) is matched with SIMBADs "MAIN_ID" value for the star. The second column specifies the spectral type of the star according to SIMBAD (with the exception of the stars mentioned in section 3.3, for which the method described in that section has been applied). The TIC and KIC columns represent the TESS and Kepler Input Catalogue identifiers respectively. The list is sorted first by spectral type, and then by main identifier.

Main Identifier	Sp. Type	TIC	KIC	Fit Type
HD 225391	A	TIC 139156518	KIC 5632093	sine
HD 226712	A	TIC 171882897	KIC 5905878	sine
TYC 3125-2237-1	A	TIC 121274152	KIC 4641547	sine
HD 187141	A0	TIC 360021868	KIC 6381306	sine
HD 188360	A0	TIC 28359846	KIC 10815604	sine
HD 177982	A2	TIC 120821069	KIC 4995049	sine
HD 225493	A4V	TIC 184163024	KIC 5201872	sine
TYC 3551-561-1	A5IV	TIC 26418553	KIC 11296464	sine
HD 225333	A5V	TIC 139037071	KIC 3458671	sine
AG+46 1529	A7III	TIC 273380253	KIC 9604762	sine
TYC 3560-1923-1	A9IV–V	TIC 271167267	KIC 10281360	sine
TYC 3565-514-1	A9V	TIC 27458214	KIC 11197934	sine
KOI-3818	B9.5Vn	TIC 159102838	KIC 6515722	sine
2MASS J18491671+4410445	F	TIC 123449867	KIC 8212826	sine
KOI-4698	F	TIC 159643077	KIC 10663738	sine
Kepler-1271	F	TIC 120825510	KIC 1996180	sine
Kepler-1443	F	TIC 164525743	KIC 10057494	sine
Kepler-380	F	TIC 48132154	KIC 11121752	sine
Kepler-494	F	TIC 169176556	KIC 6305192	sine
TYC 3134-301-1	F	TIC 137483286	KIC 3852772	sine
KOI-19	F3/F5V	TIC 123201406	KIC 7255336	sine
TYC 3557-727-1	F3/F5V	TIC 273684688	KIC 9788113	sine
TYC 3140-1658-1	F5	TIC 138967825	KIC 5802601	sine
TYC 3557-1501-1	F6IV	TIC 273043859	KIC 9724820	sine
KOI-44	F7IV	TIC 239276046	KIC 8845026	sine
Kepler-1084	F8V	TIC 267749737	KIC 10857519	sine

Main Identifier	Sp. Type	TIC	KIC	Fit Type
2MASS J18425375+4345336	G	TIC 123198563	KIC 7936748	sine
2MASS J18495232+4309276	G	TIC 123489639	KIC 7503439	
2MASS J18525868+4530560	G	TIC 164458315	KIC 9137611	sine
2MASS J18582492+4446498	G	TIC 164779298	KIC 8609289	sine
2MASS J19012927+4104159	G	TIC 120496415	KIC 5773205	sine
2MASS J19043346+4427484	G	TIC 158171605	KIC 8417863	sine
2MASS J19061691+4654395	G	TIC 158272786	KIC 10000509	sine
2MASS J19065549+3937268	G	TIC 121012476	KIC 4546541	sine
2MASS J19080680+4450500	G	TIC 158391683	KIC 8678334	sine
2MASS J19100183+4257041	G	TIC 158552191	KIC 7350021	sine
2MASS J19182441+4439465	G	TIC 159097797	KIC 8554173	sine
2MASS J19184939+4418233	G	TIC 159107064	KIC 8359762	sine
2MASS J19185028+4633324	G	TIC 159171504	KIC 9765670	sine
2MASS J19250540+3734332	G	TIC 137097085	KIC 2159377	sine
2MASS J19280249+3911165	G	TIC 137402956	KIC 4058829	sine, poly
2MASS J19283146+3837123	G	TIC 137484235	KIC 3547283	sine
2MASS J19313155+4628249	G	TIC 63452929	KIC 9712781	sine
2MASS J19320792+3933052	G	TIC 137972488	KIC 4469481	sine
2MASS J19350077+4608423	G	TIC 270698467	KIC 9531002	sine
2MASS J19354814+4118464	G	TIC 138431713	KIC 6049426	sine
2MASS J19354900+4623499	G	TIC 270789534	KIC 9654338	sine
2MASS J19364457+4403341	G	TIC 270859571	KIC 8172597	sine
2MASS J19370439+4626209	G	TIC 270957778	KIC 9716208	sine
2MASS J19390861+4046149	G	TIC 138725759	KIC 5544024	sine
2MASS J19395042+4622296	G	TIC 271354512	KIC 9657062	sine
2MASS J19415575+4522369	G	TIC 271664690	KIC 9032578	sine
2MASS J19450785+5108395	G	TIC 27778260	KIC 12367153	sine
2MASS J19484658+5002007	G	TIC 28084005	KIC 11825619	sine
2MASS J19491761+4638356	G	TIC 273131067	KIC 9845711	sine
2MASS J19535154+4211197	G	TIC 274119294	KIC 6719122	sine
2MASS J19551628+4145582	G	TIC 171093514	KIC 6390935	sine
2MASS J19553242+4737586	G	TIC 268382866	KIC 10491422	sine
2MASS J19562459+4408276	G	TIC 268606798	KIC 8257716	sine
2MASS J19572618+4520510	G	TIC 268712881	KIC 9048032	sine
2MASS J19583564+4352320	G	TIC 269121724	KIC 8055957	sine
2MASS J20060991+4417004	G	TIC 185335830	KIC 8332459	sine
ATO J285.5682+44.5725	G	TIC 352012409	KIC 8481574	sine
BD-08 995	G	TIC 43472154	-	sine
KOI-1747	G	TIC 159717069	KIC 7032421	sine
KOI-2324	G	TIC 159105557	KIC 7746958	poly

Main Identifier	Sp. Type	TIC	KIC	Fit Type
KOI-5796	G	TIC 63070665	KIC 10470779	sine
KOI-5810	G	TIC 123494489	KIC 10581308	sine
KOI-5825	G	TIC 27183790	KIC 10737437	sine
KOI-5952	G	TIC 27845077	KIC 12071775	sine
KOI-741	G	TIC 272840512	KIC 10418797	sine
Kepler-1060	G	TIC 120691237	KIC 4544907	
Kepler-1198	G	TIC 158843826	KIC 8681734	sine
Kepler-1839	G	TIC 27082730	KIC 11818607	sine
Kepler-513	G	TIC 48503953	KIC 11802615	sine
Kepler-725	G	TIC 164652841	KIC 8672910	sine
Kepler-739	G	TIC 159225155	KIC 9766437	
TYC 4595-107-1	G	TIC 394030788	-	sine
UCAC4 640-067417	G	TIC 122517231	KIC 2709412	sine
UCAC4 686-075120	G	TIC 269030397	KIC 10098932	sine
V* V452 Lyr	G	-	KIC 7742289	sine
BD-01 2318	G0	TIC 78234015	-	sine
HD 295290	G0	TIC 53417036	-	sine
TYC 3560-458-1	G0	TIC 26815845	KIC 10922836	sine
TYC 3557-1509-1	G0.5V	TIC 273379797	KIC 9726613	sine
TYC 3139-951-1	G0V	TIC 138215507	KIC 4660797	sine
Kepler-1424	G1.5Vb	TIC 122706631	KIC 5096590	sine
KOI-6202	G1V	TIC 164669854	KIC 9389245	sine
Kepler-400	G2V	TIC 122707140	KIC 5272233	sine
TYC 3131-2137-1	G2V	TIC 164460243	KIC 7871914	sine
TYC 3146-672-1	G2V	TIC 159448893	KIC 7523785	sine
TYC 3545-2661-1	G2V	TIC 399827121	KIC 10850420	sine
HD 183473	G5	TIC 63120335	KIC 7201012	sine, poly
HD 214261	G5	TIC 200501090	-	sine
KOI-644	G5	TIC 122138452	KIC 5356593	sine
TYC 3550-241-1	G5	TIC 299088815	KIC 12008308	sine
HD 23524	G5V	TIC 428761512	-	sine
TYC 3562-2088-1	G5V	TIC 273872314	KIC 10093680	sine
V* AG Lep	G5V	TIC 92845906	-	sine
HD 222259A	G6V	TIC 410214986	-	sine
Kepler-605	G7	TIC 158423850	KIC 7595157	sine, poly
TYC 3128-2312-1	G8V	TIC 120686876	KIC 5944209	sine
HD 180445	G8V(e)	TIC 97914505	-	sine
HD 220186	G9Ve	TIC 49619607	-	sine
1RXS J064643.6-770027	K	TIC 177255827	-	sine
2MASS J18524052+4156057	K	-	KIC 6500181	sine

Main Identifier	Sp. Type	TIC	KIC	Fit Type
2MASS J18534407+4208274	K	-	KIC 6668646	sine
2MASS J18535462+4135227	K	-	KIC 6183672	sine
2MASS J19004200+3903124	K	TIC 399794444	KIC 3935803	sine
2MASS J19082791+4337114	K	TIC 158389986	KIC 7879384	sine
2MASS J19324909+4229041	K	TIC 275495685	KIC 6953069	sine
2MASS J19404949+5046469	K	TIC 27398219	KIC 12166457	sine
ATO J296.1841+42.6311	K	TIC 272184059	KIC 7133807	sine
CPD-19 878	K	TIC 93125144	-	sine
KOI-7449	K	TIC 279918401	KIC 11495989	sine
KOI-8047	K	TIC 290034561	KIC 11294822	sine
Kepler-1259	K	TIC 273592350	KIC 10028535	sine
Kepler-1782	K	TIC 123202646	KIC 8142942	sine
Kepler-1856	K	TIC 27687265	KIC 12469800	sine
Kepler-1966	K	TIC 137627194	KIC 5962262	sine
Kepler-246	K	TIC 272484980	KIC 7134976	sine
Kepler-693	K	TIC 237159318	KIC 5164255	sine
PM J07058-5848	K	TIC 279615427	-	sine
TYC 1360-957-1	K	TIC 247117382	-	sine
HD 245924	K0IV	TIC 19934471	-	sine
2MASS J19200703+4335050	K0V	TIC 159220196	KIC 7816999	sine
BD+41 3306	K0V	TIC 394172596	KIC 6278762	sine, poly
CD-26 1578	K0V	TIC 44797824	-	sine
TYC 553-33-1	K0V:e	TIC 405405298	-	sine
RX J1925.0+4429	K1V	TIC 159721038	KIC 8429280	sine
V* V4371 Sgr	K1V	TIC 151839506	-	poly
HD 215341	K1Ve	TIC 145752454	-	sine
TYC 582-114-1	K1Ve	TIC 344163180	-	sine
V* LQ Hya	K1Vp	TIC 46907042	-	sine
Kepler-1558	K2	TIC 158322085	KIC 10000941	sine
HD 283750	K2.5Ve	TIC 125838647	-	sine
CD-52 381	K2V(e)	TIC 229151691	-	sine
V* V471 Tau	K2V+DA	TIC 456863710	-	sine
Kepler-411	K3V	TIC 399954349	KIC 11551692	sine
BD-13 6131	K3Ve	TIC 437696706	-	sine
V* BY Dra	K4Ve+K7.5Ve	TIC 47579336	-	sine
2MASS J19400800+4923036	K5	TIC 27390487	KIC 11461764	sine
V* CC Eri	K7V	TIC 142206123	-	sine
2MASS J18460555+4332131	M	TIC 123317330	KIC 7800087	
2MASS J18472701+4348011	M	TIC 123410529	KIC 8007234	sine
2MASS J18491356+4619042	M	TIC 123447780	KIC 9631548	sine

Main Identifier	Sp. Type	TIC	KIC	Fit Type
2MASS J18511354+4227227	M	TIC 164411695	KIC 6925256	sine
2MASS J18511902+4837594	M	TIC 48216443	KIC 11069034	sine
2MASS J18512069+4846013	M	TIC 48216303	KIC 11122350	sine
2MASS J18524238+4828368	M	TIC 48304549	KIC 10960823	sine
2MASS J18525314+4818044	M	TIC 48304703	KIC 10905192	sine
2MASS J18525455+4634012	M	TIC 164457389	KIC 9754582	sine
2MASS J18531060+4050093	M	TIC 237158804	KIC 5597695	sine
2MASS J18535987+4741070	M	TIC 164525174	KIC 10452840	sine
2MASS J18541728+4305206	M	TIC 164529739	KIC 7422811	sine
2MASS J18545269+4107528	M	TIC 350987684	KIC 5855808	sine
2MASS J18561787+4457391	M	TIC 164670879	KIC 8737443	sine
2MASS J18565158+4448162	M	TIC 164671055	KIC 8673358	sine
2MASS J18570619+4516101	M	TIC 164677934	KIC 8935942	sine
2MASS J18572876+4035369	M	TIC 120251682	KIC 5342558	sine
2MASS J18574689+4115593	M	TIC 120254207	KIC 5941226	sine
2MASS J18592859+4351465	M	TIC 164786997	KIC 8012943	sine
2MASS J19000393+4109460	M	TIC 120419969	KIC 5858361	sine
2MASS J19001025+4045358	M	TIC 120422710	KIC 5515142	sine
2MASS J19005916+4400190	M	TIC 164889286	KIC 8150479	sine
2MASS J19011064+4206175	M	TIC 164886887	KIC 6672948	sine
2MASS J19011256+4152067	M	TIC 399822429	KIC 6425989	sine
2MASS J19020142+4110533	M	TIC 120576193	KIC 5859365	sine
2MASS J19023480+4539052	M	TIC 352013620	KIC 9205855	sine
2MASS J19024516+4429007	M	TIC 352012319	KIC 8417053	
2MASS J19030585+4046008	M	TIC 120579026	KIC 5516671	sine
2MASS J19033576+3941263	M	TIC 120684614	KIC 4544623	sine
2MASS J19034709+4317208	M	TIC 158166384	KIC 7592133	sine
2MASS J19035284+4338273	M	TIC 158165866	KIC 7877209	sine
2MASS J19041026+4530403	M	TIC 158172860	KIC 9142714	sine
2MASS J19053703+4235308	M	TIC 158218091	KIC 7018323	sine
2MASS J19061507+5029221	M	TIC 399825094	KIC 12004872	sine
2MASS J19061662+4502422	M	TIC 158274889	KIC 8807085	sine
2MASS J19063685+4928043	M	TIC 399825963	KIC 11498106	sine
2MASS J19064350+5020087	M	TIC 399825217	KIC 11955208	sine
2MASS J19064648+4931162	M	TIC 399825921	KIC 11550428	sine
2MASS J19074075+3752413	M	TIC 121022434	KIC 2557669	sine
2MASS J19081745+3902346	M	TIC 121085753	KIC 3940372	sine
2MASS J19083962+4221137	M	TIC 158388172	KIC 6849112	sine
2MASS J19085407+4320395	M	TIC 158423632	KIC 7670700	sine
2MASS J19103260+4322147	M	TIC 158551504	KIC 7671594	sine

Main Identifier	Sp. Type	TIC	KIC	Fit Type
2MASS J19104382+4039368	M	TIC 121329525	KIC 5435958	sine
2MASS J19110814+4024571	M	TIC 121333779	KIC 5262561	sine
2MASS J19114749+4048205	M	TIC 121461193	KIC 5608002	sine
2MASS J19130891+5127421	M	TIC 298961665	KIC 12505054	sine
2MASS J19135561+4319299	M	TIC 158725435	KIC 7673428	sine
2MASS J19141052+4559479	M	TIC 158787568	KIC 9396972	sine
2MASS J19143720+4243450	M	TIC 158795349	KIC 7190459	
2MASS J19152845+5001374	M	TIC 299088298	KIC 11808734	sine
2MASS J19160242+4726491	M	TIC 158983853	KIC 10332732	sine
2MASS J19170322+4953087	M	TIC 299159305	KIC 11708034	sine
2MASS J19200001+3844383	M	TIC 122225323	KIC 3640527	sine
2MASS J19200978+4954168	M	TIC 267747418	KIC 11760021	sine
2MASS J19205088+5018194	M	TIC 406950619	KIC 11961075	sine
2MASS J19210354+4523201	M	TIC 159303166	KIC 9017693	sine
2MASS J19213187+4459115	M	TIC 159387244	KIC 8749769	sine
2MASS J19230963+3739397	M	TIC 122672447	KIC 2300039	sine
2MASS J19232149+5107053	M	TIC 417655942	KIC 12356051	sine
2MASS J19233077+5035350	M	TIC 417656504	KIC 12060710	sine
2MASS J19233788+4518061	M	TIC 159520226	KIC 9019435	sine
2MASS J19240851+3747169	M	TIC 122781970	KIC 2441562	sine
2MASS J19242752+5106364	M	TIC 350738203	KIC 12356489	sine
2MASS J19255059+4532219	M	TIC 159761686	KIC 9153754	sine
2MASS J19291103+4821243	M	TIC 424864617	KIC 10921009	sine
2MASS J19304396+4112528	M	TIC 137759349	KIC 5962956	sine
2MASS J19304840+4142454	M	TIC 137758161	KIC 6366739	sine
2MASS J19335656+4010546	M	-	KIC 5016904	sine, poly
2MASS J19343395+4137235	M	TIC 138222062	KIC 6290811	sine
2MASS J19353467+3943573	M	TIC 138436033	KIC 4662431	sine
2MASS J19353874+4708324	M	TIC 270790828	KIC 10146539	
2MASS J19365745+4628121	M	TIC 270957843	KIC 9716117	sine
2MASS J19374745+4341098	M	TIC 271047224	KIC 7898781	sine
2MASS J19421615+4928069	M	TIC 27531488	KIC 11515276	sine
2MASS J19423900+5108356	M	TIC 27639064	KIC 12365719	sine
2MASS J19433653+4758149	M	TIC 27645448	KIC 10676126	sine
2MASS J19443380+4843497	M	TIC 27770198	KIC 11147271	sine
2MASS J19444493+4720327	M	TIC 272279258	KIC 10285642	sine
2MASS J19450930+4754591	M	TIC 27771932	KIC 10677397	sine
2MASS J19451164+4345265	M	TIC 272270363	KIC 7973675	sine
2MASS J19454134+3906345	M	TIC 184471264	KIC 4077867	sine
2MASS J19471875+4123248	M	TIC 239228371	KIC 6060845	sine

Main Identifier	Sp. Type	TIC	KIC	Fit Type
2MASS J19471987+4747258	M	TIC 272841049	KIC 10548508	sine
2MASS J19480997+4310160	M	TIC 272943707	KIC 7547969	sine
2MASS J19503771+4705359	M	TIC 273378083	KIC 10091786	sine
2MASS J19503804+4041450	M	TIC 169816129	KIC 5471468	sine
2MASS J19505785+4630250	M	TIC 273379615	KIC 9786877	sine
2MASS J19510637+4505045	M	TIC 273383619	KIC 8836388	sine
2MASS J19525571+4743328	M	TIC 273874034	KIC 10553513	sine
2MASS J19542833+4420425	M	TIC 268158580	KIC 8387621	sine
2MASS J19543981+4814406	M	TIC 264508845	KIC 10880514	sine
2MASS J19550625+4009192	M	TIC 171101426	KIC 5041192	sine
2MASS J19553603+4805356	M	TIC 416528859	KIC 10753072	sine
2MASS J19561258+4335485	M	TIC 268485803	KIC 7847566	sine
2MASS J19584764+4711122	M	TIC 269029909	KIC 10165815	sine
2MASS J20000387+4531405	M	TIC 239234887	KIC 9179906	sine
ATO J285.1153+45.7850	M	TIC 164882037	KIC 9267818	sine
KOI-1654	M	TIC 48355200	KIC 11546211	sine
UCAC4 639-062929	M	TIC 120963868	KIC 2284919	sine
UCAC4 643-073385	M	TIC 138647610	KIC 3454793	sine
UCAC4 651-066418	M	TIC 120354289	KIC 4904647	sine
UCAC4 661-082974	M	TIC 268288304	KIC 6720765	sine
UCAC4 664-071715	M	TIC 158430593	KIC 7104739	sine
UCAC4 668-073165	M	TIC 158432884	KIC 7741987	sine
UCAC4 683-066189	M	TIC 351897570	KIC 9692206	sine
UCAC4 707-062317	M	TIC 299097784	KIC 12403318	sine
1RXS J060224.9-163451	M0	TIC 95328477	-	sine
V* MY Tau	M0.5e	TIC 348638763	-	sine
WOH S 209	M0:	TIC 179038379	-	sine
Kepler-210	M0V	TIC 63283780	KIC 7447200	poly
MCC 428	M0V	TIC 434136638	-	
V* HK Aqr	M0Ve	TIC 5656273	-	sine
HG 7-26	M1	TIC 345454031	-	
V* OT Ser	M1.0V	TIC 355793860	-	sine, poly
V* V631 Tau	M1.5	TIC 348638813	-	sine
2MASS J18563342+4513481	M1.5V	TIC 164670606	KIC 8935655	sine
G 6-33	M1.5V	TIC 434160946	-	sine
V* FF And	M1Ve+M1Ve	TIC 267802440	-	sine
HD 197481	M1VeBa1	TIC 441420236	-	poly
[LM84] 3-13	M2	TIC 165124012	-	sine
V* AX Cnc	M2.0	TIC 175233993	-	sine, poly
2MASS J19412234+5104273	M2.1	TIC 27454242	KIC 12314646	sine

Main Identifier	Sp. Type	TIC	KIC	Fit Type
1RXS J004211.1-425245	M2.2	TIC 80427281	-	sine
2MASS J04133314-5231586	M2.4	TIC 219229275	-	sine
PM J19399+3950	M2.5	TIC 138893136	KIC 4758595	sine
UCAC4 647-065171	M2.5	TIC 121215155	KIC 4142890	sine
G 10-29	M2.5V	TIC 396951485	-	sine
LP 474-124	M2.5V	TIC 348663808	-	
2MASS J19130537+5020559	M2.5Ve	TIC 298962893	KIC 11957647	sine
ASAS J232857-6802.4	M2.5Ve	TIC 229807000	-	sine
2MASS J19324802+4200580	M2.7	TIC 275496670	KIC 6610837	sine
2MASS J19445931+4812415	M2.8	TIC 27772498	KIC 10872868	sine
V* V497 Tau	M2.9	TIC 258032026	-	sine
CD-51 13128	M2Ve	TIC 140045538	-	sine
2MASS J19183060+4153031	M3	TIC 122067236	KIC 6436291	sine
[PS78] 219	M3+	TIC 11652986	-	
UCAC4 698-065839	M3.0	TIC 48504458	KIC 11495571	sine
G 9-11	M3.0V	TIC 21246336	-	sine
UCAC4 673-078334	M3.0Ve	TIC 272272592	KIC 8507979	sine
G 209-3	M3.4	TIC 28231379	KIC 10877432	sine
V* LT Tau	M3.5	TIC 258067389	-	sine
BD-15 6290	M3.5V	TIC 188580272	-	sine
LP 426-35	M3.5V	TIC 197247983	-	
LP 737-14	M3.5V	TIC 335628483	-	
2MASS J22371494-2622332	M3.5Ve	TIC 326446019	-	sine
BD+16 2708	M3V	TIC 258105174	-	
KOI-256	M3V	TIC 48528261	KIC 11548140	sine
LAMOST J192817.82+410412.2	M3V	TIC 137410897	KIC 5791720	sine
2MASS J18535530+4310389	M3Ve	TIC 164529625	KIC 7505644	sine
2MASS J18592696+4548446	M3Ve	TIC 164784762	KIC 9328653	sine
2MASS J19015564+4134218	M3Ve	TIC 120576760	KIC 6187812	sine
CD-43 9546	M3Ve	TIC 334524122	-	poly
CD-56 1032A	M3Ve	TIC 220433363	-	sine
2MASS J04534379-5836247	M3e	TIC 220432563	-	sine
2MASS J22534969-1721358	M4	TIC 188586529	-	
LP 873-37	M4	TIC 99566892	-	
1RXS J185504.7+425952	M4.0V	TIC 164644375	KIC 7341653	sine
HG 8-80	M4.0V	TIC 435916078	-	sine
V* EV Lac	M4.0Ve	TIC 154101678	-	sine
2MASS J01275875-6032243	M4.2	TIC 237910557	-	sine
2MASS J19150930+5101139	M4.5V	TIC 299089441	KIC 12302994	
2MASS J19573917+4554182	M4.5V	TIC 268711231	KIC 9426508	sine

Main Identifier	Sp. Type	TIC	KIC	Fit Type
G 6-7	M4.5V	TIC 456938518	-	sine
UCAC4 683-069625	M4.5V	TIC 159171299	KIC 9705079	sine
2MASS J18432784+4727325	M4Ve	TIC 123205792	KIC 10318386	sine
2MASS J18474286+4218039	M4Ve	TIC 123408865	KIC 6837702	sine
2MASS J18535193+4327449	M4Ve	TIC 164529313	KIC 7734382	sine
2MASS J19005766+4428279	M4Ve	TIC 164889852	KIC 8416220	sine
2MASS J19045588+3738361	M4Ve	TIC 120825083	KIC 2283749	sine
CD-56 1032B	M4Ve	TIC 220433364	-	sine
Kepler-1646	M4Ve	TIC 158552258	KIC 7350067	sine
2MASS J21484123-4736506	M5	TIC 147421845	-	sine
UCAC3 53-724	M5.5V	TIC 425937691	-	sine
G 205-40	M5V	TIC 164458193	KIC 9201463	sine
LP 357-206	M5e	TIC 14079970	-	sine
LP 760-3	M6.5V	-	-	
2MASS J19202351+5037161	M6Ve	TIC 267746625	KIC 12108566	sine
V* V692 Tau	M:	TIC 149923415	-	sine
L 762-51	dM3.5	TIC 286942673	-	
GALEX J184242.4+440405	sdB	TIC 123198279	KIC 8142623	sine
GALEX J191612.1+474915	sdB+F/G	TIC 158984345	KIC 10593239	sine
SDSS J192715.88+380808.2	sdB+dM	-	KIC 2991403	sine

Table A.2.: Table containing all main-sequence stars of spectral type M for which flares have been found. The first column (Main Identifier) is matched with SIMBADs "MAIN_ID" value for the star. The second column specifies the spectral type of the star according to SIMBAD (with the exception of the stars mentioned in section 3.3, for which the method described in that section has been applied). The TIC and KIC columns represent the TESS and Kepler Input Catalogue identifiers respectively. The fit type column specifies the used fit types which were found to work best for the lightcurves. The list is sorted first by spectral type, and then by main identifier.

Main Identifier	Sp. Type	TIC	KIC	Fit Type
2MASS J18565158+4448162	M	TIC 164671055	KIC 8673358	sine
2MASS J18570619+4516101	M	TIC 164677934	KIC 8935942	sine
2MASS J18572876+4035369	M	TIC 120251682	KIC 5342558	sine
2MASS J19023480+4539052	M	TIC 352013620	KIC 9205855	sine
2MASS J19061662+4502422	M	TIC 158274889	KIC 8807085	sine
2MASS J19074075+3752413	M	TIC 121022434	KIC 2557669	sine
2MASS J19230963+3739397	M	TIC 122672447	KIC 2300039	sine
2MASS J19255059+4532219	M	TIC 159761686	KIC 9153754	sine

Main Identifier	Sp. Type	TIC	KIC	Fit Type
2MASS J19421615+4928069	M	TIC 27531488	KIC 11515276	sine
UCAC4 643-073385	M	TIC 138647610	KIC 3454793	sine
1RXS J060224.9-163451	M0	TIC 95328477	-	sine
V* MY Tau	M0.5e	TIC 348638763	-	sine
WOH S 209	M0:	TIC 179038379	-	sine
V* HK Aqr	M0Ve	TIC 5656273	-	sine
V* OT Ser	M1.0V	TIC 355793860	-	sine, poly
V* V631 Tau	M1.5	TIC 348638813	-	sine
2MASS J18563342+4513481	M1.5V	TIC 164670606	KIC 8935655	sine
V* FF And	M1Ve+M1Ve	TIC 267802440	-	sine
[LM84] 3-13	M2	TIC 165124012	-	sine
V* AX Cnc	M2.0	TIC 175233993	-	sine, poly
1RXS J004211.1-425245	M2.2	TIC 80427281	-	sine
2MASS J04133314-5231586	M2.4	TIC 219229275	-	sine
G 10-29	M2.5V	TIC 396951485	-	sine
ASAS J232857-6802.4	M2.5Ve	TIC 229807000	-	sine
V* V497 Tau	M2.9	TIC 258032026	-	sine
CD-51 13128	M2Ve	TIC 140045538	-	sine
UCAC4 698-065839	M3.0	TIC 48504458	KIC 11495571	sine
G 9-11	M3.0V	TIC 21246336	-	sine
G 209-3	M3.4	TIC 28231379	KIC 10877432	sine
V* LT Tau	M3.5	TIC 258067389	-	sine
BD-15 6290	M3.5V	TIC 188580272	-	sine
2MASS J22371494-2622332	M3.5Ve	TIC 326446019	-	sine
KOI-256	M3V	TIC 48528261	KIC 11548140	sine
LAMOST J192817.82+410412.2	M3V	TIC 137410897	KIC 5791720	sine
CD-56 1032A	M3Ve	TIC 220433363	-	sine
2MASS J04534379-5836247	M3e	TIC 220432563	-	sine
1RXS J185504.7+425952	M4.0V	TIC 164644375	KIC 7341653	sine
HG 8-80	M4.0V	TIC 435916078	-	sine
V* EV Lac	M4.0Ve	TIC 154101678	-	sine
2MASS J01275875-6032243	M4.2	TIC 237910557	-	sine
G 6-7	M4.5V	TIC 456938518	-	sine
2MASS J19005766+4428279	M4Ve	TIC 164889852	KIC 8416220	sine
CD-56 1032B	M4Ve	TIC 220433364	-	sine
Kepler-1646	M4Ve	TIC 158552258	KIC 7350067	sine
2MASS J21484123-4736506	M5	TIC 147421845	-	sine
UCAC3 53-724	M5.5V	TIC 425937691	-	sine
G 205-40	M5V	TIC 164458193	KIC 9201463	sine
LP 357-206	M5e	TIC 14079970	-	sine

Main Identifier	Sp. Type	TIC	KIC	Fit Type
V* V692 Tau	M:	TIC 149923415	-	sine

Table A.3.: Table containing all main-sequence stars of spectral type K for which flares have been found. The first column (Main Identifier) is matched with SIMBADs "MAIN_ID" value for the star. The second column specifies the spectral type of the star according to SIMBAD (with the exception of the stars mentioned in section 3.3, for which the method described in that section has been applied). The TIC and KIC columns represent the TESS and Kepler Input Catalogue idetifiers respectively. The fit type column specifies the used fit types which were found to work best for the lightcurves. The list is sorted first by spectral type, and then by main identifier.

Main Identifier	Sp. Type	TIC	KIC	Fit Type
1RXS J064643.6-770027	K	TIC 177255827	-	sine
2MASS J19404949+5046469	K	TIC 27398219	KIC 12166457	sine
CPD-19 878	K	TIC 93125144	-	sine
Kepler-693	K	TIC 237159318	KIC 5164255	sine
PM J07058-5848	K	TIC 279615427	-	sine
TYC 1360-957-1	K	TIC 247117382	-	sine
HD 245924	K0IV	TIC 19934471	-	sine
CD-26 1578	K0V	TIC 44797824	-	sine
TYC 553-33-1	K0V:e	TIC 405405298	-	sine
RX J1925.0+4429	K1V	TIC 159721038	KIC 8429280	sine
HD 215341	K1Ve	TIC 145752454	-	sine
TYC 582-114-1	K1Ve	TIC 344163180	-	sine
V* LQ Hya	K1Vp	TIC 46907042	-	sine
Kepler-1558	K2	TIC 158322085	KIC 10000941	sine
HD 283750	K2.5Ve	TIC 125838647	-	sine
CD-52 381	K2V(e)	TIC 229151691	-	sine
V* V471 Tau	K2V+DA	TIC 456863710	-	sine
Kepler-411	K3V	TIC 399954349	KIC 11551692	sine
BD-13 6131	K3Ve	TIC 437696706	-	sine
V* BY Dra	K4Ve+K7.5Ve	TIC 47579336	-	sine
V* CC Eri	K7V	TIC 142206123	-	sine

Table A.4.: Table containing all main-sequence stars of spectral type G for which flares have been found. The first column (Main Identifier) is matched with SIMBADs "MAIN_ID" value for the star. The second column specifies the spectral type of the star according to SIMBAD (with the exception of the stars mentioned in section 3.3, for which the method described in that section has been applied). The TIC and KIC columns represent the TESS and Kepler Input Catalogues respectively. The fit type column specifies the used fit types which were found to work best for the lightcurves. The list is sorted first by spectral type, and then by main identifier.

Main Identifier	Sp. Type	TIC	KIC	Fit Type
2MASS J18425375+4345336	G	TIC 123198563	KIC 7936748	sine
2MASS J19061691+4654395	G	TIC 158272786	KIC 10000509	sine
2MASS J19320792+3933052	G	TIC 137972488	KIC 4469481	sine
2MASS J19553242+4737586	G	TIC 268382866	KIC 10491422	sine
2MASS J20060991+4417004	G	TIC 185335830	KIC 8332459	sine
ATO J285.5682+44.5725	G	TIC 352012409	KIC 8481574	sine
BD-08 995	G	TIC 43472154	-	sine
Kepler-725	G	TIC 164652841	KIC 8672910	sine
TYC 4595-107-1	G	TIC 394030788	-	sine
V* V452 Lyr	G	-	KIC 7742289	sine
BD-01 2318	G0	TIC 78234015	-	sine
HD 295290	G0	TIC 53417036	-	sine
TYC 3146-672-1	G2V	TIC 159448893	KIC 7523785	sine
HD 214261	G5	TIC 200501090	-	sine
KOI-644	G5	TIC 122138452	KIC 5356593	sine
HD 23524	G5V	TIC 428761512	-	sine
V* AG Lep	G5V	TIC 92845906	-	sine
HD 222259A	G6V	TIC 410214986	-	sine
Kepler-605	G7	TIC 158423850	KIC 7595157	sine, poly
HD 180445	G8V(e)	TIC 97914505	-	sine
HD 220186	G9Ve	TIC 49619607	-	sine

Table A.5.: Table containing all main-sequence stars of spectral type F for which flares have been found. The first column (Main Identifier) is matched with SIMBADs "MAIN_ID" value for the star. The second column specifies the spectral type of the star according to SIMBAD (with the exception of the stars mentioned in section 3.3, for which the method described in that section has been applied). The TIC and KIC columns represent the TESS and Kepler Input Catalogue identifiers respectively. The fit type column specifies the used fit types which were found to work best for the lightcurves. The list is sorted first by spectral type, and then by main identifier.

Main Identifier	Sp. Type	TIC	KIC	Fit Type
Kepler-380	F	TIC 48132154	KIC 11121752	sine
KOI-19	F3/F5V	TIC 123201406	KIC 7255336	sine
TYC 3557-1501-1	F6IV	TIC 273043859	KIC 9724820	sine
Kepler-1084	F8V	TIC 267749737	KIC 10857519	sine

Table A.6.: Table containing all stars for which either no flares have been found, or which did not match the spectral types M, K, G or F. The first column (Main Identifier) is matched with SIMBADs "MAIN_ID" value for the star. The second column specifies the spectral type of the star according to SIMBAD (with the exception of the stars mentioned in section 3.3, for which the method described in that section has been applied). The TIC and KIC columns represent the TESS and Kepler Input Catalogue identifiers respectively. The list is sorted first by spectral type, and then by main identifier.

Main Identifier	Sp. Type	TIC	KIC	Fit Type
HD 225391	A	TIC 139156518	KIC 5632093	sine
HD 226712	A	TIC 171882897	KIC 5905878	sine
TYC 3125-2237-1	A	TIC 121274152	KIC 4641547	sine
HD 187141	A0	TIC 360021868	KIC 6381306	sine
HD 188360	A0	TIC 28359846	KIC 10815604	sine
HD 177982	A2	TIC 120821069	KIC 4995049	sine
HD 225493	A4V	TIC 184163024	KIC 5201872	sine
TYC 3551-561-1	A5IV	TIC 26418553	KIC 11296464	sine
HD 225333	A5V	TIC 139037071	KIC 3458671	sine
AG+46 1529	A7III	TIC 273380253	KIC 9604762	sine
TYC 3560-1923-1	A9IV–V	TIC 271167267	KIC 10281360	sine
TYC 3565-514-1	A9V	TIC 27458214	KIC 11197934	sine
KOI-3818	B9.5Vn	TIC 159102838	KIC 6515722	sine
2MASS J18491671+4410445	F	TIC 123449867	KIC 8212826	sine
KOI-4698	F	TIC 159643077	KIC 10663738	sine
Kepler-1271	F	TIC 120825510	KIC 1996180	sine

Main Identifier	Sp. Type	TIC	KIC	Fit Type
Kepler-1443	F	TIC 164525743	KIC 10057494	sine
Kepler-494	F	TIC 169176556	KIC 6305192	sine
TYC 3134-301-1	F	TIC 137483286	KIC 3852772	sine
TYC 3557-727-1	F3/F5V	TIC 273684688	KIC 9788113	sine
TYC 3140-1658-1	F5	TIC 138967825	KIC 5802601	sine
KOI-44	F7IV	TIC 239276046	KIC 8845026	sine
2MASS J18495232+4309276	G	TIC 123489639	KIC 7503439	
2MASS J18525868+4530560	G	TIC 164458315	KIC 9137611	sine
2MASS J18582492+4446498	G	TIC 164779298	KIC 8609289	sine
2MASS J19012927+4104159	G	TIC 120496415	KIC 5773205	sine
2MASS J19043346+4427484	G	TIC 158171605	KIC 8417863	sine
2MASS J19065549+3937268	G	TIC 121012476	KIC 4546541	sine
2MASS J19080680+4450500	G	TIC 158391683	KIC 8678334	sine
2MASS J19100183+4257041	G	TIC 158552191	KIC 7350021	sine
2MASS J19182441+4439465	G	TIC 159097797	KIC 8554173	sine
2MASS J19184939+4418233	G	TIC 159107064	KIC 8359762	sine
2MASS J19185028+4633324	G	TIC 159171504	KIC 9765670	sine
2MASS J19250540+3734332	G	TIC 137097085	KIC 2159377	sine
2MASS J19280249+3911165	G	TIC 137402956	KIC 4058829	sine, poly
2MASS J19283146+3837123	G	TIC 137484235	KIC 3547283	sine
2MASS J19313155+4628249	G	TIC 63452929	KIC 9712781	sine
2MASS J19350077+4608423	G	TIC 270698467	KIC 9531002	sine
2MASS J19354814+4118464	G	TIC 138431713	KIC 6049426	sine
2MASS J19354900+4623499	G	TIC 270789534	KIC 9654338	sine
2MASS J19364457+4403341	G	TIC 270859571	KIC 8172597	sine
2MASS J19370439+4626209	G	TIC 270957778	KIC 9716208	sine
2MASS J19390861+4046149	G	TIC 138725759	KIC 5544024	sine
2MASS J19395042+4622296	G	TIC 271354512	KIC 9657062	sine
2MASS J19415575+4522369	G	TIC 271664690	KIC 9032578	sine
2MASS J19450785+5108395	G	TIC 27778260	KIC 12367153	sine
2MASS J19484658+5002007	G	TIC 28084005	KIC 11825619	sine
2MASS J19491761+4638356	G	TIC 273131067	KIC 9845711	sine
2MASS J19535154+4211197	G	TIC 274119294	KIC 6719122	sine
2MASS J19551628+4145582	G	TIC 171093514	KIC 6390935	sine
2MASS J19562459+4408276	G	TIC 268606798	KIC 8257716	sine
2MASS J19572618+4520510	G	TIC 268712881	KIC 9048032	sine
2MASS J19583564+4352320	G	TIC 269121724	KIC 8055957	sine
KOI-1747	G	TIC 159717069	KIC 7032421	sine
KOI-2324	G	TIC 159105557	KIC 7746958	poly
KOI-5796	G	TIC 63070665	KIC 10470779	sine

Main Identifier	Sp. Type	TIC	KIC	Fit Type
KOI-5810	G	TIC 123494489	KIC 10581308	sine
KOI-5825	G	TIC 27183790	KIC 10737437	sine
KOI-5952	G	TIC 27845077	KIC 12071775	sine
KOI-741	G	TIC 272840512	KIC 10418797	sine
Kepler-1060	G	TIC 120691237	KIC 4544907	
Kepler-1198	G	TIC 158843826	KIC 8681734	sine
Kepler-1839	G	TIC 27082730	KIC 11818607	sine
Kepler-513	G	TIC 48503953	KIC 11802615	sine
Kepler-739	G	TIC 159225155	KIC 9766437	
UCAC4 640-067417	G	TIC 122517231	KIC 2709412	sine
UCAC4 686-075120	G	TIC 269030397	KIC 10098932	sine
TYC 3560-458-1	G0	TIC 26815845	KIC 10922836	sine
TYC 3557-1509-1	G0.5V	TIC 273379797	KIC 9726613	sine
TYC 3139-951-1	G0V	TIC 138215507	KIC 4660797	sine
Kepler-1424	G1.5Vb	TIC 122706631	KIC 5096590	sine
KOI-6202	G1V	TIC 164669854	KIC 9389245	sine
Kepler-400	G2V	TIC 122707140	KIC 5272233	sine
TYC 3131-2137-1	G2V	TIC 164460243	KIC 7871914	sine
TYC 3545-2661-1	G2V	TIC 399827121	KIC 10850420	sine
HD 183473	G5	TIC 63120335	KIC 7201012	sine, poly
TYC 3550-241-1	G5	TIC 299088815	KIC 12008308	sine
TYC 3562-2088-1	G5V	TIC 273872314	KIC 10093680	sine
TYC 3128-2312-1	G8V	TIC 120686876	KIC 5944209	sine
2MASS J18524052+4156057	K	-	KIC 6500181	sine
2MASS J18534407+4208274	K	-	KIC 6668646	sine
2MASS J18535462+4135227	K	-	KIC 6183672	sine
2MASS J19004200+3903124	K	TIC 399794444	KIC 3935803	sine
2MASS J19082791+4337114	K	TIC 158389986	KIC 7879384	sine
2MASS J19324909+4229041	K	TIC 275495685	KIC 6953069	sine
ATO J296.1841+42.6311	K	TIC 272184059	KIC 7133807	sine
KOI-7449	K	TIC 279918401	KIC 11495989	sine
KOI-8047	K	TIC 290034561	KIC 11294822	sine
Kepler-1259	K	TIC 273592350	KIC 10028535	sine
Kepler-1782	K	TIC 123202646	KIC 8142942	sine
Kepler-1856	K	TIC 27687265	KIC 12469800	sine
Kepler-1966	K	TIC 137627194	KIC 5962262	sine
Kepler-246	K	TIC 272484980	KIC 7134976	sine
2MASS J19200703+4335050	K0V	TIC 159220196	KIC 7816999	sine
BD+41 3306	K0V	TIC 394172596	KIC 6278762	sine, poly
V* V4371 Sgr	K1V	TIC 151839506	-	poly

Main Identifier	Sp. Type	TIC	KIC	Fit Type
2MASS J19400800+4923036	K5	TIC 27390487	KIC 11461764	sine
2MASS J18460555+4332131	M	TIC 123317330	KIC 7800087	
2MASS J18472701+4348011	M	TIC 123410529	KIC 8007234	sine
2MASS J18491356+4619042	M	TIC 123447780	KIC 9631548	sine
2MASS J18511354+4227227	M	TIC 164411695	KIC 6925256	sine
2MASS J18511902+4837594	M	TIC 48216443	KIC 11069034	sine
2MASS J18512069+4846013	M	TIC 48216303	KIC 11122350	sine
2MASS J18524238+4828368	M	TIC 48304549	KIC 10960823	sine
2MASS J18525314+4818044	M	TIC 48304703	KIC 10905192	sine
2MASS J18525455+4634012	M	TIC 164457389	KIC 9754582	sine
2MASS J18531060+4050093	M	TIC 237158804	KIC 5597695	sine
2MASS J18535987+4741070	M	TIC 164525174	KIC 10452840	sine
2MASS J18541728+4305206	M	TIC 164529739	KIC 7422811	sine
2MASS J18545269+4107528	M	TIC 350987684	KIC 5855808	sine
2MASS J18561787+4457391	M	TIC 164670879	KIC 8737443	sine
2MASS J18574689+4115593	M	TIC 120254207	KIC 5941226	sine
2MASS J18592859+4351465	M	TIC 164786997	KIC 8012943	sine
2MASS J19000393+4109460	M	TIC 120419969	KIC 5858361	sine
2MASS J19001025+4045358	M	TIC 120422710	KIC 5515142	sine
2MASS J19005916+4400190	M	TIC 164889286	KIC 8150479	sine
2MASS J19011064+4206175	M	TIC 164886887	KIC 6672948	sine
2MASS J19011256+4152067	M	TIC 399822429	KIC 6425989	sine
2MASS J19020142+4110533	M	TIC 120576193	KIC 5859365	sine
2MASS J19024516+4429007	M	TIC 352012319	KIC 8417053	
2MASS J19030585+4046008	M	TIC 120579026	KIC 5516671	sine
2MASS J19033576+3941263	M	TIC 120684614	KIC 4544623	sine
2MASS J19034709+4317208	M	TIC 158166384	KIC 7592133	sine
2MASS J19035284+4338273	M	TIC 158165866	KIC 7877209	sine
2MASS J19041026+4530403	M	TIC 158172860	KIC 9142714	sine
2MASS J19053703+4235308	M	TIC 158218091	KIC 7018323	sine
2MASS J19061507+5029221	M	TIC 399825094	KIC 12004872	sine
2MASS J19063685+4928043	M	TIC 399825963	KIC 11498106	sine
2MASS J19064350+5020087	M	TIC 399825217	KIC 11955208	sine
2MASS J19064648+4931162	M	TIC 399825921	KIC 11550428	sine
2MASS J19081745+3902346	M	TIC 121085753	KIC 3940372	sine
2MASS J19083962+4221137	M	TIC 158388172	KIC 6849112	sine
2MASS J19085407+4320395	M	TIC 158423632	KIC 7670700	sine
2MASS J19103260+4322147	M	TIC 158551504	KIC 7671594	sine
2MASS J19104382+4039368	M	TIC 121329525	KIC 5435958	sine
2MASS J19110814+4024571	M	TIC 121333779	KIC 5262561	sine

Main Identifier	Sp. Type	TIC	KIC	Fit Type
2MASS J19114749+4048205	M	TIC 121461193	KIC 5608002	sine
2MASS J19130891+5127421	M	TIC 298961665	KIC 12505054	sine
2MASS J19135561+4319299	M	TIC 158725435	KIC 7673428	sine
2MASS J19141052+4559479	M	TIC 158787568	KIC 9396972	sine
2MASS J19143720+4243450	M	TIC 158795349	KIC 7190459	
2MASS J19152845+5001374	M	TIC 299088298	KIC 11808734	sine
2MASS J19160242+4726491	M	TIC 158983853	KIC 10332732	sine
2MASS J19170322+4953087	M	TIC 299159305	KIC 11708034	sine
2MASS J19200001+3844383	M	TIC 122225323	KIC 3640527	sine
2MASS J19200978+4954168	M	TIC 267747418	KIC 11760021	sine
2MASS J19205088+5018194	M	TIC 406950619	KIC 11961075	sine
2MASS J19210354+4523201	M	TIC 159303166	KIC 9017693	sine
2MASS J19213187+4459115	M	TIC 159387244	KIC 8749769	sine
2MASS J19232149+5107053	M	TIC 417655942	KIC 12356051	sine
2MASS J19233077+5035350	M	TIC 417656504	KIC 12060710	sine
2MASS J19233788+4518061	M	TIC 159520226	KIC 9019435	sine
2MASS J19240851+3747169	M	TIC 122781970	KIC 2441562	sine
2MASS J19242752+5106364	M	TIC 350738203	KIC 12356489	sine
2MASS J19291103+4821243	M	TIC 424864617	KIC 10921009	sine
2MASS J19304396+4112528	M	TIC 137759349	KIC 5962956	sine
2MASS J19304840+4142454	M	TIC 137758161	KIC 6366739	sine
2MASS J19335656+4010546	M	-	KIC 5016904	sine, poly
2MASS J19343395+4137235	M	TIC 138222062	KIC 6290811	sine
2MASS J19353467+3943573	M	TIC 138436033	KIC 4662431	sine
2MASS J19353874+4708324	M	TIC 270790828	KIC 10146539	
2MASS J19365745+4628121	M	TIC 270957843	KIC 9716117	sine
2MASS J19374745+4341098	M	TIC 271047224	KIC 7898781	sine
2MASS J19423900+5108356	M	TIC 27639064	KIC 12365719	sine
2MASS J19433653+4758149	M	TIC 27645448	KIC 10676126	sine
2MASS J19443380+4843497	M	TIC 27770198	KIC 11147271	sine
2MASS J19444493+4720327	M	TIC 272279258	KIC 10285642	sine
2MASS J19450930+4754591	M	TIC 27771932	KIC 10677397	sine
2MASS J19451164+4345265	M	TIC 272270363	KIC 7973675	sine
2MASS J19454134+3906345	M	TIC 184471264	KIC 4077867	sine
2MASS J19471875+4123248	M	TIC 239228371	KIC 6060845	sine
2MASS J19471987+4747258	M	TIC 272841049	KIC 10548508	sine
2MASS J19480997+4310160	M	TIC 272943707	KIC 7547969	sine
2MASS J19503771+4705359	M	TIC 273378083	KIC 10091786	sine
2MASS J19503804+4041450	M	TIC 169816129	KIC 5471468	sine
2MASS J19505785+4630250	M	TIC 273379615	KIC 9786877	sine

Main Identifier	Sp. Type	TIC	KIC	Fit Type
2MASS J19510637+4505045	M	TIC 273383619	KIC 8836388	sine
2MASS J19525571+4743328	M	TIC 273874034	KIC 10553513	sine
2MASS J19542833+4420425	M	TIC 268158580	KIC 8387621	sine
2MASS J19543981+4814406	M	TIC 264508845	KIC 10880514	sine
2MASS J19550625+4009192	M	TIC 171101426	KIC 5041192	sine
2MASS J19553603+4805356	M	TIC 416528859	KIC 10753072	sine
2MASS J19561258+4335485	M	TIC 268485803	KIC 7847566	sine
2MASS J19584764+4711122	M	TIC 269029909	KIC 10165815	sine
2MASS J20000387+4531405	M	TIC 239234887	KIC 9179906	sine
ATO J285.1153+45.7850	M	TIC 164882037	KIC 9267818	sine
KOI-1654	M	TIC 48355200	KIC 11546211	sine
UCAC4 639-062929	M	TIC 120963868	KIC 2284919	sine
UCAC4 651-066418	M	TIC 120354289	KIC 4904647	sine
UCAC4 661-082974	M	TIC 268288304	KIC 6720765	sine
UCAC4 664-071715	M	TIC 158430593	KIC 7104739	sine
UCAC4 668-073165	M	TIC 158432884	KIC 7741987	sine
UCAC4 683-066189	M	TIC 351897570	KIC 9692206	sine
UCAC4 707-062317	M	TIC 299097784	KIC 12403318	sine
Kepler-210	M0V	TIC 63283780	KIC 7447200	poly
MCC 428	M0V	TIC 434136638	-	
HG 7-26	M1	TIC 345454031	-	
G 6-33	M1.5V	TIC 434160946	-	sine
HD 197481	M1VeBa1	TIC 441420236	-	poly
2MASS J19412234+5104273	M2.1	TIC 27454242	KIC 12314646	sine
PM J19399+3950	M2.5	TIC 138893136	KIC 4758595	sine
UCAC4 647-065171	M2.5	TIC 121215155	KIC 4142890	sine
LP 474-124	M2.5V	TIC 348663808	-	
2MASS J19130537+5020559	M2.5Ve	TIC 298962893	KIC 11957647	sine
2MASS J19324802+4200580	M2.7	TIC 275496670	KIC 6610837	sine
2MASS J19445931+4812415	M2.8	TIC 27772498	KIC 10872868	sine
2MASS J19183060+4153031	M3	TIC 122067236	KIC 6436291	sine
[PS78] 219	M3+	TIC 11652986	-	
UCAC4 673-078334	M3.0Ve	TIC 272272592	KIC 8507979	sine
LP 426-35	M3.5V	TIC 197247983	-	
LP 737-14	M3.5V	TIC 335628483	-	
BD+16 2708	M3V	TIC 258105174	-	
2MASS J18535530+4310389	M3Ve	TIC 164529625	KIC 7505644	sine
2MASS J18592696+4548446	M3Ve	TIC 164784762	KIC 9328653	sine
2MASS J19015564+4134218	M3Ve	TIC 120576760	KIC 6187812	sine
CD-43 9546	M3Ve	TIC 334524122	-	poly

Main Identifier	Sp. Type	TIC	KIC	Fit Type
2MASS J22534969-1721358	M4	TIC 188586529	-	
LP 873-37	M4	TIC 99566892	-	
2MASS J19150930+5101139	M4.5V	TIC 299089441	KIC 12302994	
2MASS J19573917+4554182	M4.5V	TIC 268711231	KIC 9426508	sine
UCAC4 683-069625	M4.5V	TIC 159171299	KIC 9705079	sine
2MASS J18432784+4727325	M4Ve	TIC 123205792	KIC 10318386	sine
2MASS J18474286+4218039	M4Ve	TIC 123408865	KIC 6837702	sine
2MASS J18535193+4327449	M4Ve	TIC 164529313	KIC 7734382	sine
2MASS J19045588+3738361	M4Ve	TIC 120825083	KIC 2283749	sine
LP 760-3	M6.5V	-	-	
2MASS J19202351+5037161	M6Ve	TIC 267746625	KIC 12108566	sine
L 762-51	dM3.5	TIC 286942673	-	
GALEX J184242.4+440405	sdB	TIC 123198279	KIC 8142623	sine
GALEX J191612.1+474915	sdB+F/G	TIC 158984345	KIC 10593239	sine
SDSS J192715.88+380808.2	sdB+dM	-	KIC 2991403	sine

B Additional folded lightcurves

B.1 TYC 4595-107-1

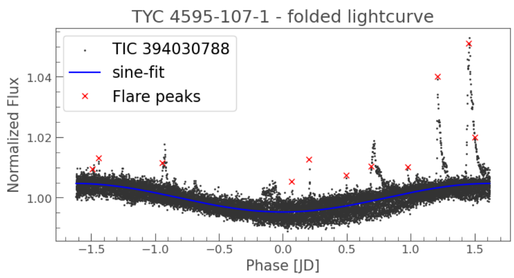

(a) TESS Sector 14

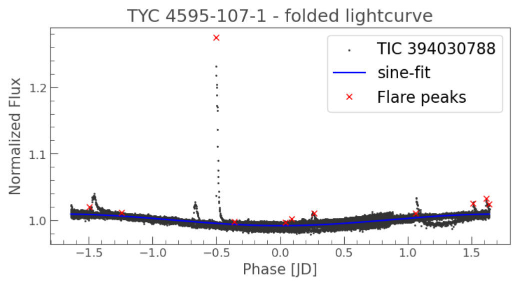

(b) TESS Sector 18

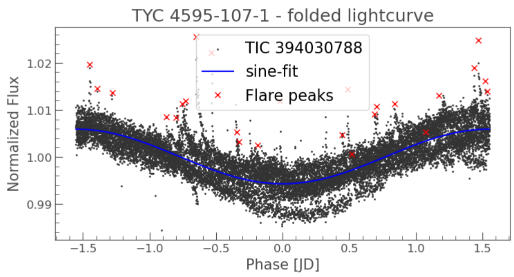

(c) TESS Sector 19

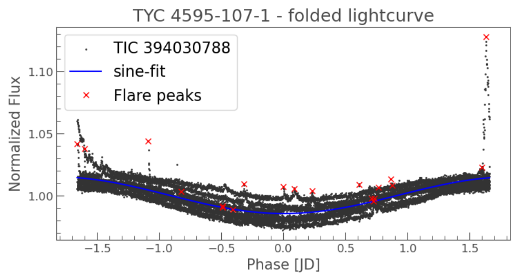

(d) TESS Sector 24

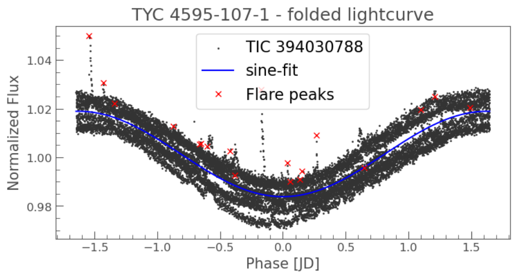

(e) TESS Sector 25

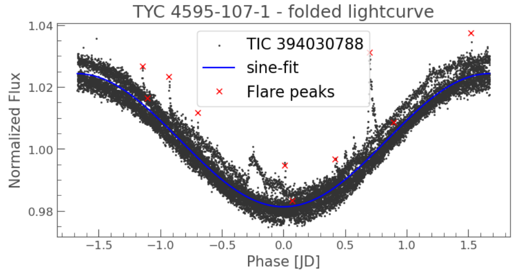

(f) TESS Sector 26

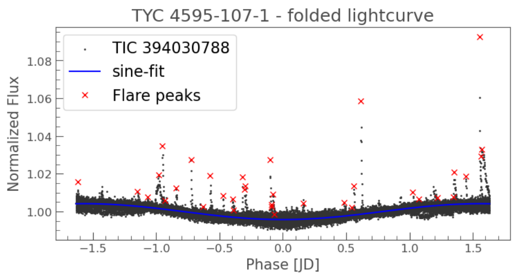

(g) TESS Sector 40

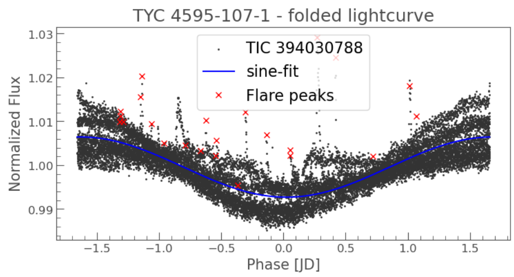

(h) TESS Sector 41

Fig. B.1.: Folded lightcurves for TYC 4595-107-1.

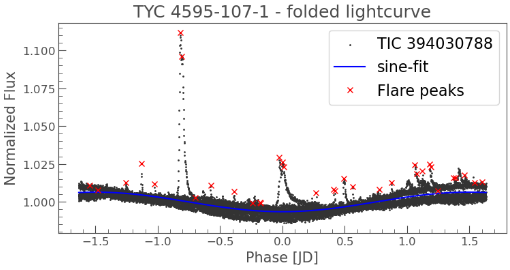

(a) TESS Sector 47

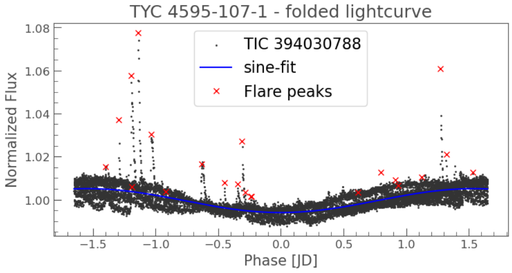

(b) TESS Sector 51

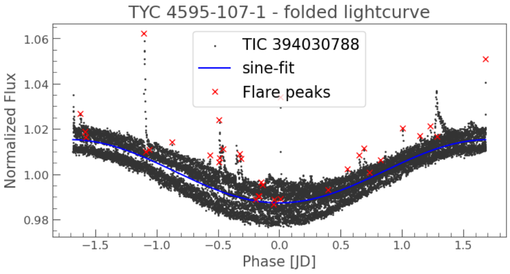

(c) TESS Sector 52

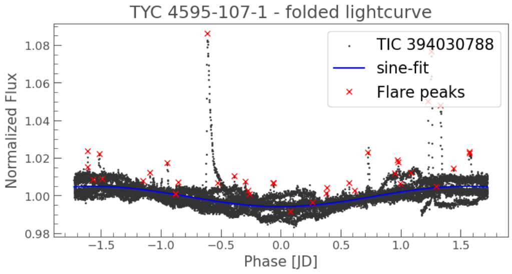

(d) TESS Sector 53

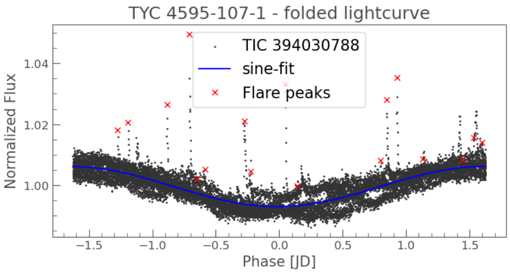

(e) TESS Sector 54

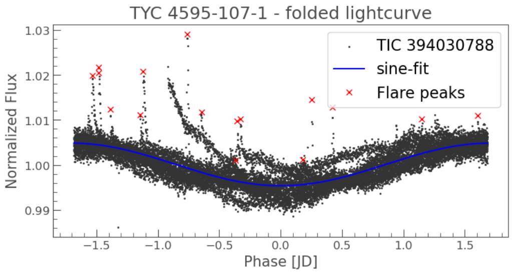

(f) TESS Sector 58

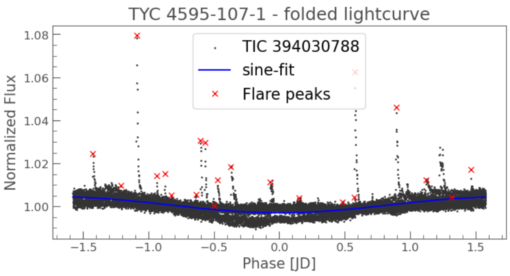

(g) TESS Sector 59

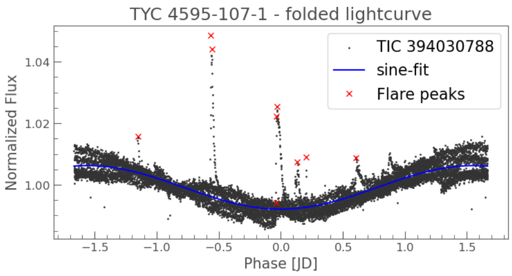

(h) TESS Sector 60

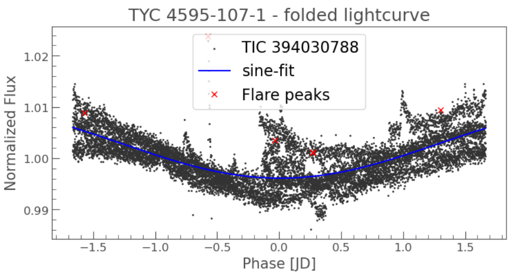

(i) TESS Sector 73

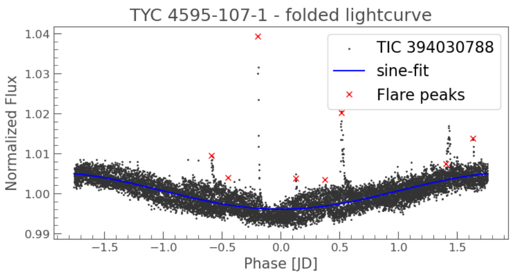

(j) TESS Sector 74

Fig. B.2.: Folded lightcurves for TYC 4595-107-1.

B.2 V471 Tau

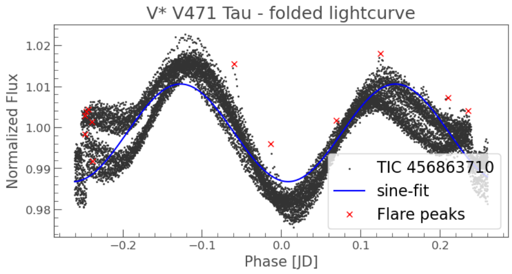

(a) TESS Sector 42

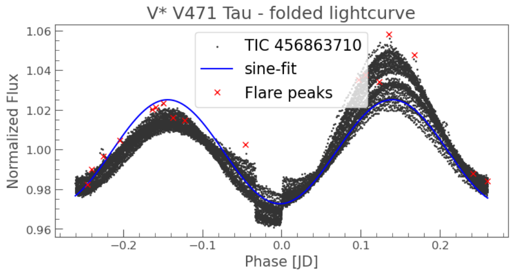

(b) TESS Sector 43

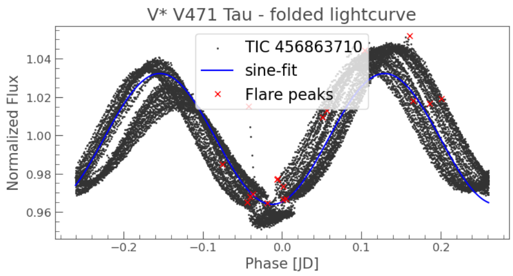

(c) TESS Sector 44

Fig. B.3.: Folded lightcurves for V* V471 Tau by rotational period.

B.3 KOI-256

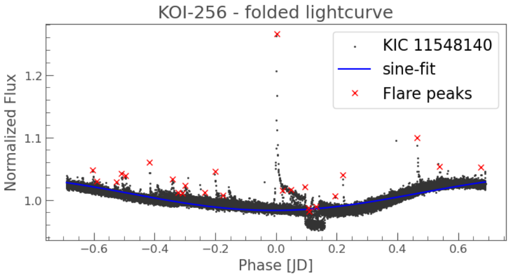

(a) Kepler target table ID 35

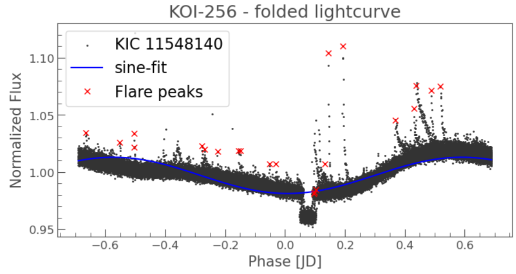

(b) Kepler target table ID 36

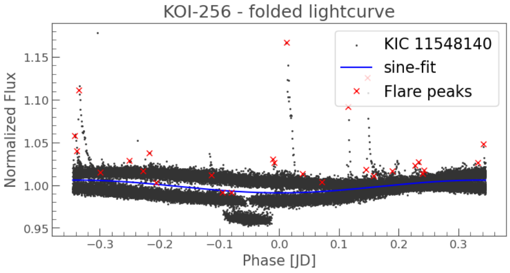

(c) Kepler target table ID 37

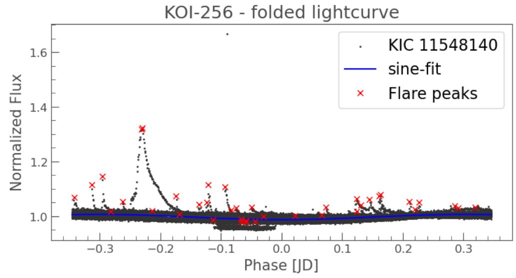

(d) Kepler target table ID 38

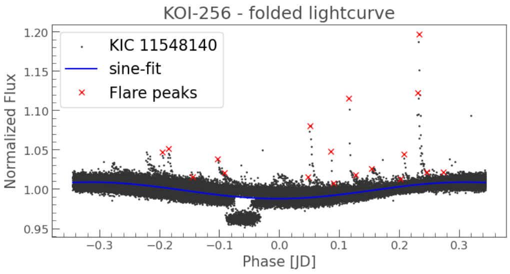

(e) Kepler target table ID 39

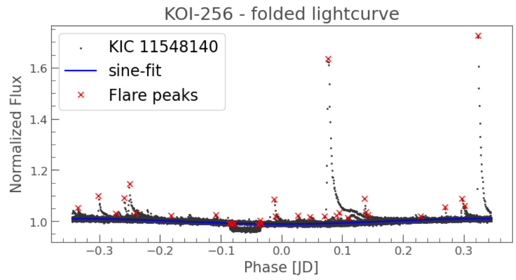

(f) Kepler target table ID 40

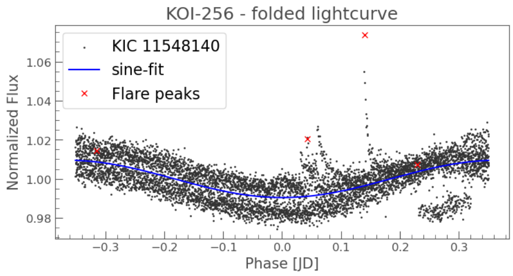

(g) Kepler target table ID 69

Fig. B.4.: Folded Kepler lightcurves for KOI-256.

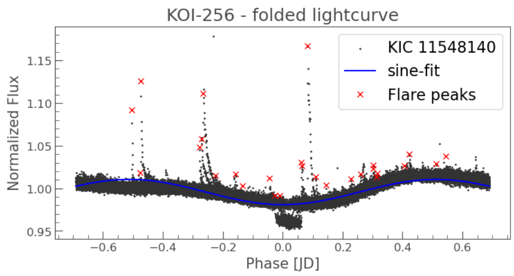

(a) Kepler target table ID 37

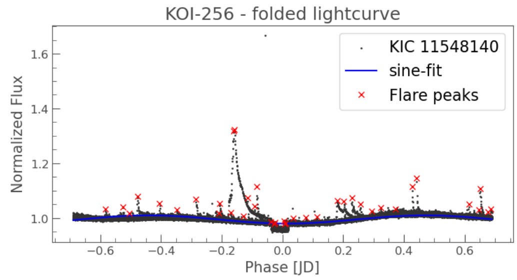

(b) Kepler target table ID 38

Fig. B.5.: Folded Kepler lightcurves for KOI-256 by rotational period.

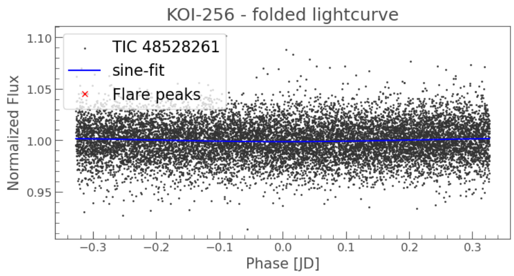

(a) TESS sector 53

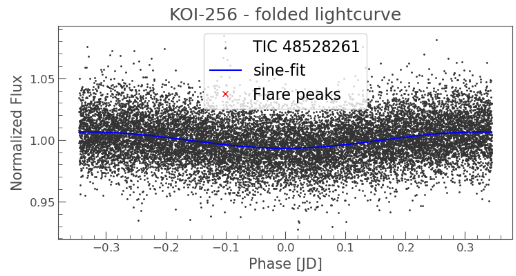

(b) TESS sector 75

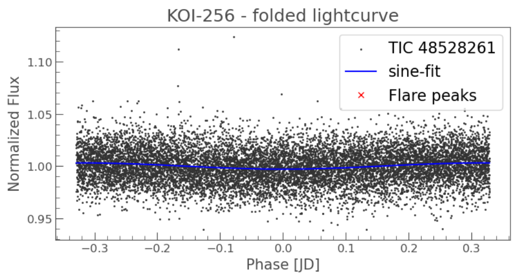

(c) TESS sector 80

Fig. B.6.: Folded TESS lightcurves for KOI-256.

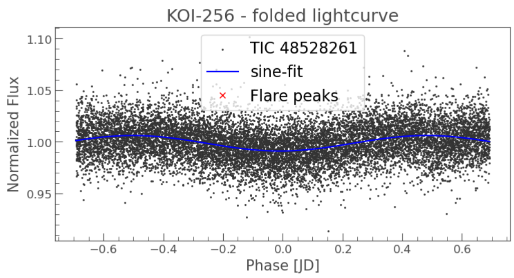

(a) TESS sector 53

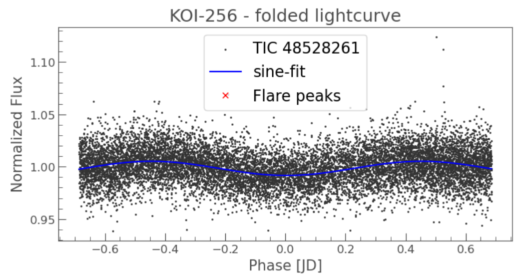

(b) TESS sector 80

Fig. B.7.: Folded TESS lightcurves for KOI-256 by rotational period.

C Miscellaneous lightcurves

Appendix for miscellaneous lightcurves that can not be attributed to any of the topics, but are still noteworthy.

C.1 2MASS J19033576+3941263

2MASS J19033576+3941263 also known as KOI-6423.

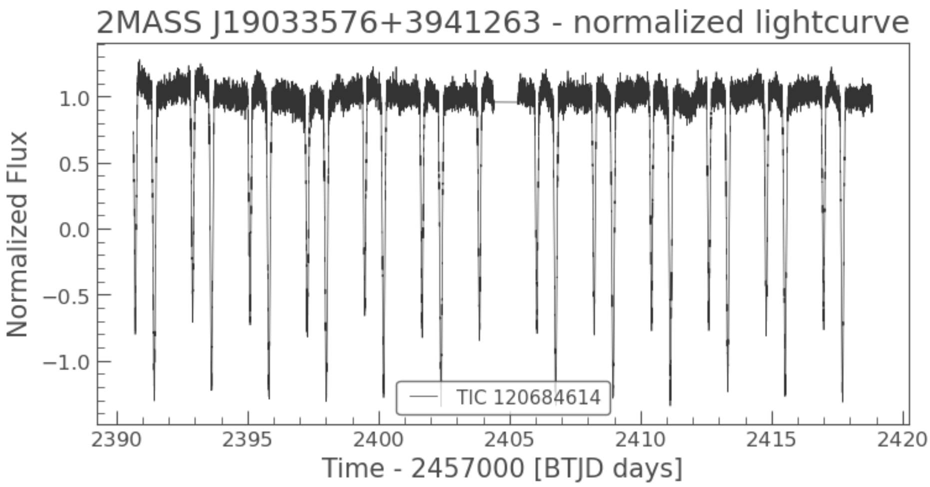

(a) TESS Sector 40

Fig. C.1.: Lightcurves for 2MASS J19033576+3941263, also known as KOI-6423.

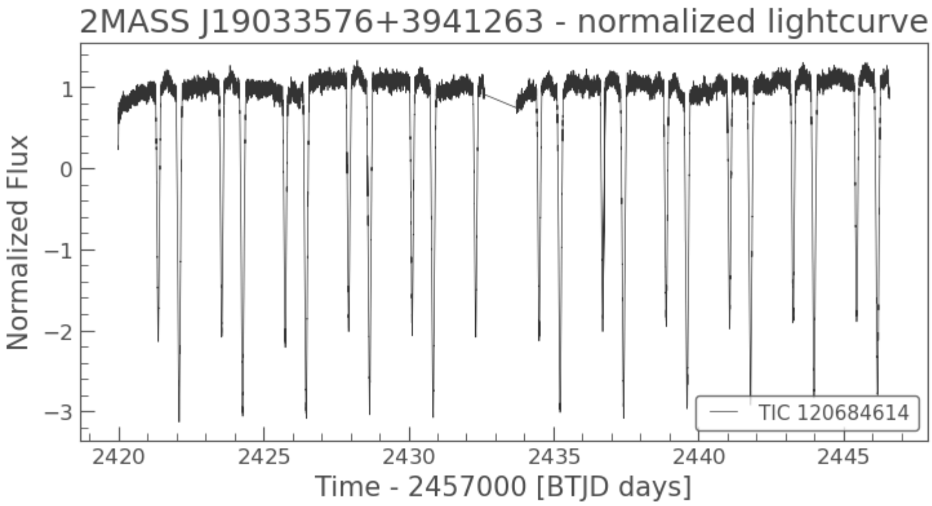

(a) TESS Sector 41

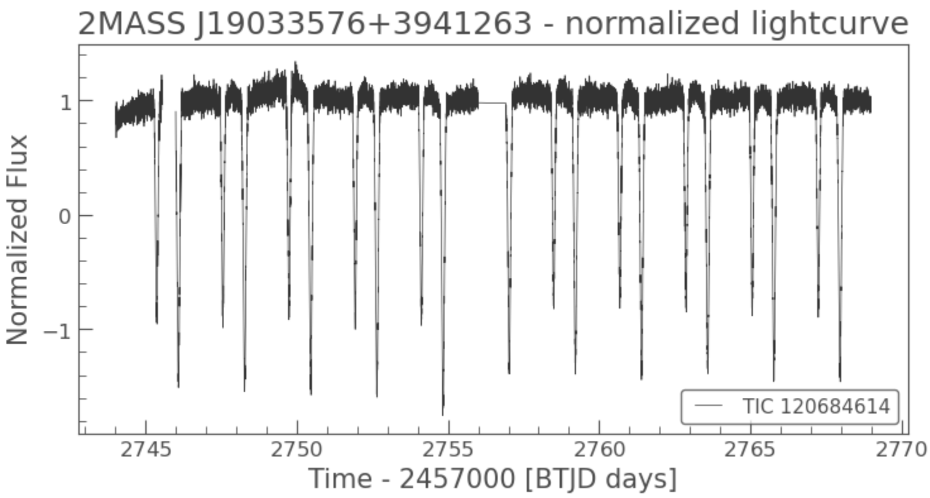

(b) TESS Sector 53

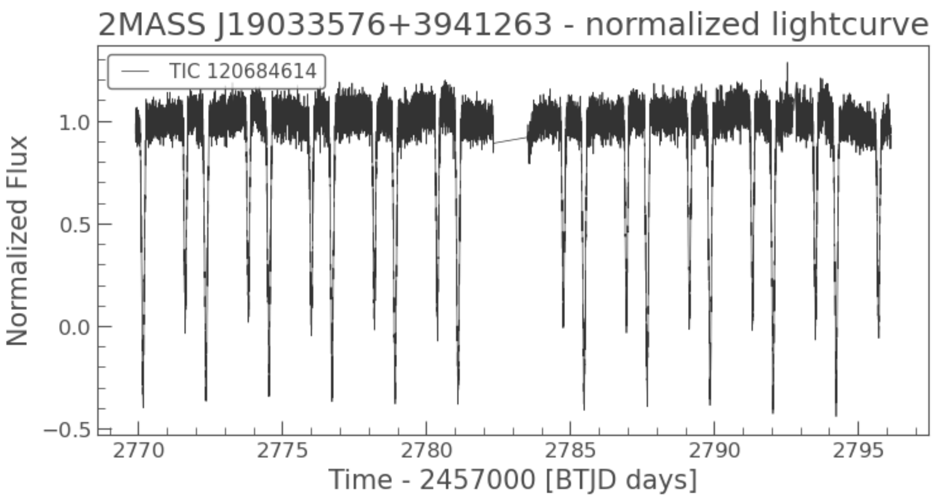

(c) TESS Sector 54

Fig. C.2.: Lightcurves for 2MASS J19033576+3941263, also known as KOI-6423.

C.2 V* V452 Lyr

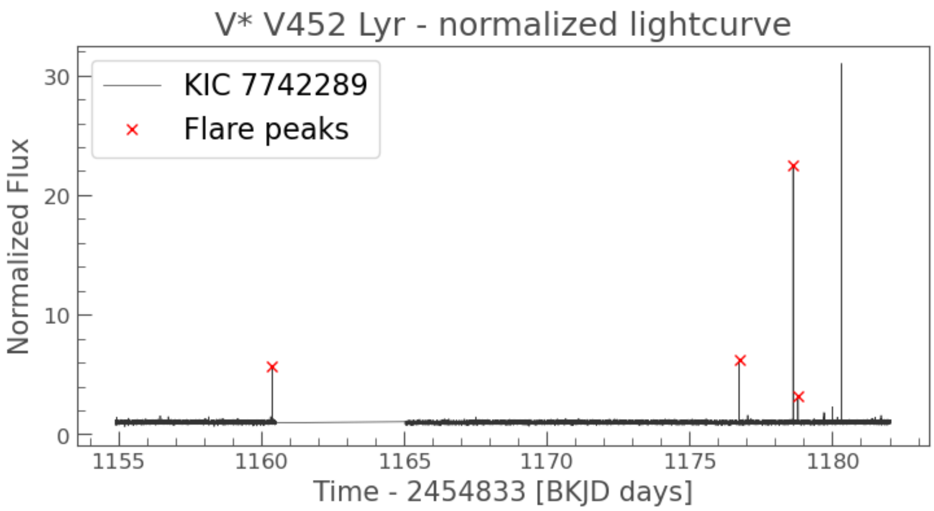

(a) Kepler target table ID 55, normalized lightcurve

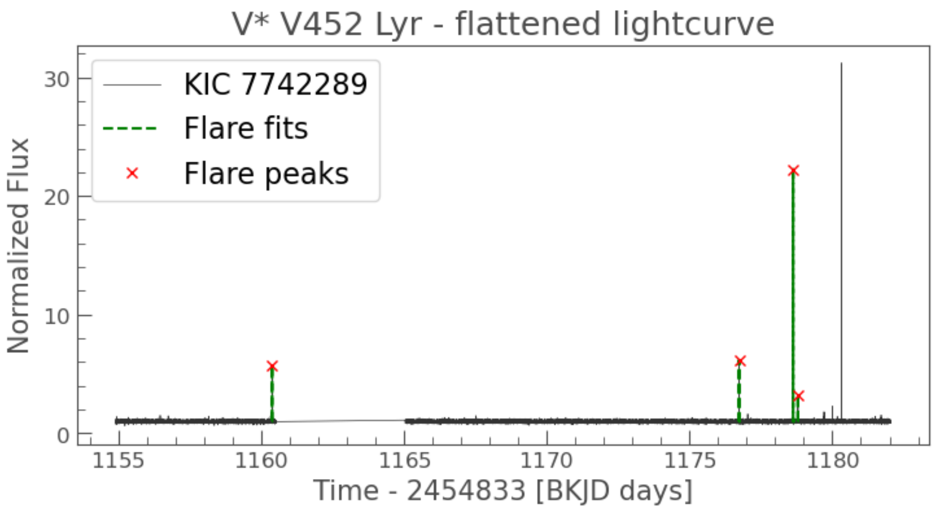

(b) Kepler target table ID 55, flattened lightcurve

Fig. C.3.: Lightcurves for V* V452 Lyr.

Colophon

This thesis was typeset with $\LaTeX\ 2_\varepsilon$. It uses the *Clean Thesis* style developed by Ricardo Langner, available at http://cleanthesis.der-ric.de/. The design of the *Clean Thesis* style is inspired by user guide documents from Apple Inc.

The template is provided in this adapted version by Desmond Grossmann, BSc, Stefan Janisch, BSc, Lea Schimak and Paul Beck, PhD to implement the editorial guidelines of *Astronomy & Astrophysics* and the cooperate-identity guidelines of the University of Graz for the Institute for Physics. Version: March, 2024.

Declaration

I declare that I have authored this thesis independently, that I have not used other than the declared sources/resources, and that I have explicitly indicated all material which has been quoted either literally or by content from the sources used. The text document uploaded to UNIGRAZonline or TUGRAZonline is identical to the present master's thesis.

Graz, June 10, 2025

Markus Ornik, BSc